МИСИС
УНИВЕРСИТЕТ

ISSN 1997-308X
eISSN 2412-8767

ИЗВЕСТИЯ ВУЗОВ
ПОРОШКОВАЯ МЕТАЛЛУРГИЯ И ФУНКЦИОНАЛЬНЫЕ ПОКРЫТИЯ

2025
Том 19 № 2
Vol. 19 No. 2

POWDER METALLURGY AND FUNCTIONAL COATINGS

powder.misis.ru

ISSN 1997-308X
eISSN 2412-8767

POWDER METALLURGY AND FUNCTIONAL COATINGS

Scientific and Technical Journal
Founded in 2007
Six issues per year

2025
Том 19 № 2
Vol. 19 No. 2

ИЗВЕСТИЯ ВУЗОВ ПОРОШКОВАЯ МЕТАЛЛУРГИЯ И ФУНКЦИОНАЛЬНЫЕ ПОКРЫТИЯ

Научно-технический журнал
Основан в 2007 г.
Выходит 6 раз в год

POWDER METALLURGY AND FUNCTIONAL COATINGS

SCIENTIFIC AND TECHNICAL JOURNAL
FOUNDED IN 2007
SIX ISSUES PER YEAR

http://powder.misis.ru

ISSN 1997-308X
eISSN 2412-8767

Founder:

**National University of Science
and Technology "MISIS"**
Address: 1 Bld, 4 Leninskiy Prosp., Moscow 119049, Russian Federation
http://www.misis.ru

Editor-in-Chief

Evgeny A. Levashov
Prof., Dr. Sci. (Eng.), Acad. of the RANS, NUST MISIS, Moscow, Russian Federation

Journal is included into the List of peer-reviewed scientific publications recommended by the Highest Attestation Commission of the Ministry of Education and Science of the Russian Federation for publishing the results of doctoral and candidate dissertations.
Abstracting/Indexing: Scopus, Russian Science Citation Index (RSCI), Ulrich's Periodicals Directory, VINITI Database (Abstract Journal).

Editorial Board

M. I. Alymov – Dr. Sci. (Eng.), Corresponding Member of the RAS, Merzhanov Institute of Structural Macrokinetics and Materials Sciences of the RAS, Chernogolovka, Russia
A. P. Amosov – Prof., Dr. Sci. (Phys.-Math.), Samara State Technical University, Samara, Russia
I. V. Blinkov – Prof., Dr. Sci. (Eng.), NUST MISIS, Moscow, Russia
M. V. Chukin – Prof., Dr. Sci. (Eng.), Magnitogorsk State Technical University, Magnitogorsk, Russia
H. Danninger – Prof., Dr. Sci., Vienna University of Technology, Vienna, Austria
B. Derin – Assoc. Prof., Dr. Sci. (Phil.), Istanbul Technical University, Maslak, Istanbul, Turkey
V. Yu. Dorofeyev – Prof., Dr. Sci. (Eng.), South-Russian State Polytechnical University (NPI), Novocherkassk, Russia
Yu. Estrin – Prof., Dr. Sci. (Nat.), Monash University, Clayton, Australia
A. Ph. Ilyushchanka – Prof., Dr. Sci. (Eng.), Acad. of the NAS of Belarus, State Research and Production Powder Metallurgy Association, Minsk, Belarus
Yu. R. Kolobov – Prof., Dr. Sci. (Phys.-Math.), Federal Research Center of Problems of Chemical Pfysics and Medicinal Chemistry of the RAS, Chernogolovka, Russia
V. S. Komlev – Prof., Dr. Sci. (Eng.), Corresponding Member of the RAS, Institute of Metallurgy of the RAS, Moscow, Russia
I. Konyashin – Prof., Dr. Sci. (Econ.), Element Six GmbH, Burghaun, Germany
Yu. M. Korolyov – Prof., Dr. Sci. (Eng.), Scientific and Technical Association "Powder Metallurgy", Moscow, Russia
D. Yu. Kovalev – Dr. Sci. (Phys.-Math.), Merzhanov Institute of Structural Macrokinetics and Materials Sciences of the RAS, Chernogolovka, Russia
S. A. Kulinich – Assoc. Prof., PhD (Chem.), Tokai University, Hiratsuka, Kanagawa, Japan
S. V. Kuzmin – Prof., Dr. Sci. (Eng.), Corresponding Member of the RAS, Volgograd State Technical University, Volgograd, Russia
V. P. Kuznetsov – Prof., Dr. Sci. (Eng.), Ural Federal University, Ekaterinburg, Russia
Yu. V. Levinsky – Prof., Dr. Sci. (Eng.) Merzhanov Institute of Structural Macrokinetics and Materials Sciences of the RAS, Chernogolovka, Russia
A. E. Ligachyov – Prof., Dr. Sci. (Phys.-Math.), Prokhorov General Physics Institute of the RAS, Moscow, Russia
V. Yu. Lopatin – Cand. Sci., NUST MISIS, Moscow, Russia
A. A. Lozovan – Prof., Dr. Sci (Eng.), Moscow Aviation Institute (NRU), Moscow, Russia
V. I. Lysak – Prof., Dr. Sci. (Eng.), Acad. of the RAS, Volgograd State Technical University, Volgograd, Russia
A. V. Makarov – Dr. Sci. (Eng.), Corresponding Member of the RAS, M.N. Mikheev Institute of Metal Physics of the Ural Branch of the RAS, Ural Federal University, Ekaterinburg, Russia
L. L. Mishnaevsky – Dr. Habil. (Eng.), Technical University of Denmark, Roskilde, Denmark
A. S. Mukasyan – Prof., Dr. Sci. (Phys.-Math.), University of Notre Dame, Notre Dame, USA
S. A. Oglezneva – Prof., Dr. Sci. (Eng.), Perm National Research Polytechnical University, Perm, Russia
R. Orrù – Prof., Dr. Sci. (Eng.), University of Cagliari, Cagliari, Italy
I. B. Panteleev – Prof., Dr. Sci. (Eng.), St. Petersburg State Technological Institute (Technical University), St. Petersburg, Russia
F. Peizhong – Prof., Dr. Sci., China University of Mining and Technology, Xuzhou, P.R. China
C. Pengwan – Prof., Dr. Sci., Beijing Institute of Technology, Beijing, P.R. China
M. I. Petrzhik – Dr. Sci. (Eng.), NUST MISIS, Moscow, Russia
Yu. S. Pogozhev – Assoc. Prof., Cand. Sci. (Eng.), NUST MISIS, Moscow, Russia
V. V. Polyakov – Prof., Dr. Sci. (Phys.-Math.), Altai State University, Barnaul, Russia
A. A. Popovich – Prof., Dr. Sci. (Eng.)., Corresp. Member of the RANS, St. Petersburg State Polytechnical University (National Research University), St. Petersburg, Russia
S. E. Porozova – Dr. Sci. (Eng.), Perm National Research Polytechnical University, Perm, Russia
A. A. Rempel – Prof., Dr. Sci. (Phys.-Math.), Acad. of the RAS, Institute of Metallurgy of the Ural Branch of the RAS, Ekaterinburg, Russia
F. Rustichelli – Prof., Dr. Sci. (Phys.), University of Marches, Ancona, Italy
S. D. Shlyapin – Prof., Dr. Sci. (Eng.), Moscow Aviation Institute (NRU), Moscow, Russia
D. V. Shtansky – Prof., Dr. Sci. (Phys.-Math.), NUST MISIS, Moscow, Russia
A. N. Timofeev – Dr. Sci. (Eng.), JSC "Komposite", Korolev, Russia
P. A. Vityaz' – Prof., Dr. Sci. (Eng.), Acad. of the NAS of Belarus, Minsk, Belarus
A. A. Zaitsev – Assoc. Prof., Cand. Sci. (Eng.), NUST MISIS, Moscow, Russia
Zheng YongTing – Prof., Dr. Sci., Harbin Institute of Technology, Harbin, P.R. China
F. Zhengyi – Prof., Dr. Sci., Wuhan University of Technology, Wuhan, P.R. China

Editorial Staff

Address: NUST MISIS,
1 Bld, 4 Leninskiy Prosp., Moscow 119049, Russian Federation

Phone: +7 (495) 638-45-35. ***E-mail:*** izv.vuz@misis.ru

Certificate of registration **No. FS77-27955** (12.04.2007)
Re-registration **PI No. FS77-79230** (25.09.2020)

Leading Editor: O.V. Sosnina
Executive Editor: A.A. Kudinova
Layout Designer: V.V. Rasenets

Signed print 21.02.2025. Format 60×90 $^{1}/_{8}$
Offset paper No. 1. Digital printing. Quires 9.00
Order 21935. Free price
Printed in the printing house of the MISIS Publish House
1 Bld, 4 Leninskiy Prosp., Moscow 119049, Russian Federation
Phone/fax: +7 (499) 236-76-17

PM & FC © NUST MISIS, Moscow, 2025

Articles are available under Creative Commons Attribution Non-Commercial No Derivatives

ИЗВЕСТИЯ ВУЗОВ ПОРОШКОВАЯ МЕТАЛЛУРГИЯ И ФУНКЦИОНАЛЬНЫЕ ПОКРЫТИЯ

НАУЧНО-ТЕХНИЧЕСКИЙ ЖУРНАЛ
ОСНОВАН В 2007 Г.
ВЫХОДИТ 6 РАЗ В ГОД

http://powder.misis.ru

ISSN 1997-308X
eISSN 2412-8767

Учредитель: МИСИС
УНИВЕРСИТЕТ
НАУКИ И ТЕХНОЛОГИЙ

ФГАОУ ВО Национальный исследовательский
технологический университет «МИСИС»
Адрес: 119049, Москва, Ленинский пр-т, 4, стр. 1
https://www.misis.ru

Главный редактор

Евгений Александрович Левашов
д.т.н., академик РАЕН, профессор, НИТУ МИСИС, г. Москва

Журнал включен в Перечень рецензируемых научных изданий, рекомендованных ВАК Минобрнауки РФ для публикации результатов диссертаций на соискание ученых степеней.
Журнал включен в базы данных: Scopus, Russian Science Citation Index (RSCI), Ulrich's Periodicals Directory, РИНЦ, БД/РЖ ВИНИТИ.

Редакционная коллегия

М. И. Алымов – д.т.н., чл.-корр. РАН, проф., ИСМАН, г. Черноголовка
А. П. Амосов – д.ф.-м.н., проф., СамГТУ, г. Самара
И. В. Блинков – д.т.н., проф., НИТУ МИСИС, г. Москва
П. А. Витязь – д.т.н., акад. НАНБ, проф., НАН Беларуси, г. Минск
В. Ю. Дорофеев – д.т.н., проф., ЮРГПУ (НПИ), г. Новочеркасск
А. А. Зайцев – к.т.н., доц., НИТУ МИСИС, г. Москва
А. Ф. Ильющенко – д.т.н., акад. НАН Беларуси, проф., ГНПО ПМ НАН Беларуси, г. Минск
Д. Ю. Ковалев – д.ф.-м.н., ИСМАН, г. Черноголовка
Ю. Р. Колобов – д.ф.-м.н., проф., ФИЦ ПХФ и МХ РАН, г. Черноголовка
В. С. Комлев – д.т.н., чл.-корр. РАН, проф., ИМЕТ РАН, г. Москва
Ю. М. Королев – д.т.н., проф., НТА «Порошковая металлургия», г. Москва
В. П. Кузнецов – д.т.н., проф., УрФУ, г. Екатеринбург
С. В. Кузьмин – д.т.н., чл.-корр. РАН, проф., ВолгГТУ, г. Волгоград
Ю. В. Левинский – д.т.н., проф., ИСМАН, г. Черноголовка
А. Е. Лигачев – д.ф.-м.н., проф., ИОФ РАН, г. Москва
А. А. Лозован – д.т.н., проф., МАИ (НИУ), г. Москва
В. Ю. Лопатин – к.т.н., доц., НИТУ МИСИС, г. Москва
В. И. Лысак – д.т.н., акад. РАН, проф., ВолгГТУ, г. Волгоград
А. В. Макаров – д.т.н., чл.-корр. РАН, ИФМ УрО РАН, УрФУ, г. Екатеринбург
С. А. Оглезнева – д.т.н., проф., ПНИПУ, г. Пермь
И. Б. Пантелеев – д.т.н., проф., СПбГТИ (ТУ), г. Санкт-Петербург
М. И. Петржик – д.т.н., проф., НИТУ МИСИС, г. Москва
Ю. С. Погожев – к.т.н., доц., НИТУ МИСИС, г. Москва
В. В. Поляков – д.ф.-м.н., проф., АлтГУ, г. Барнаул
А. А. Попович – д.т.н., чл.-корр. РАЕН, проф., СПбГПУ, г. Санкт-Петербург
С. Е. Порозова – д.т.н., проф., ПНИПУ, г. Пермь
А. А. Ремпель – д.ф.-м.н., акад. РАН, проф., ИМЕТ УрО РАН, г. Екатеринбург
А. Н. Тимофеев – д.т.н., АО «Композит», г. Королев
М. В. Чукин – д.т.н., проф., МГТУ, г. Магнитогорск
С. Д. Шляпин – д.т.н., проф., МАИ (НИУ), г. Москва
Д. В. Штанский – д.ф.-м.н., проф., НИТУ МИСИС, г. Москва
H. Danninger – Dr. Sci., Prof., Vienna University of Technology, Vienna, Austria
B. Derin – Dr. Sci. (Phil.), Assoc. Prof., Istanbul Technical University, Maslak, Istanbul, Turkey
Yu. Estrin – Dr. Sci. (Nat.), Prof., Monash University, Clayton, Australia
I. Konyashin – Dr. Sci. (Econ.), Prof., Element Six GmbH, Burghaun, Germany
S. A. Kulinich – PhD (Chem.), Associate Prof., Tokai University, Hiratsuka, Kanagawa, Japan
L. L. Mishnaevsky – Dr. Habil. (Eng.), Technical University of Denmark, Roskilde, Denmark
A. S. Mukasyan – Dr. Sci. (Phys.-Math.), Prof., University of Notre Dame, Notre Dame, USA
R. Orrù – Dr. Sci. (Eng.), Prof., University of Cagliari, Cagliari, Italy
F. Peizhong – Dr. Sci., Prof., China University of Mining and Technology, Xuzhou, P.R. China
C. Pengwan – Dr. Sci., Prof., Beijing Institute of Technology, Beijing, P.R. China
F. Rustichelli – Dr. Sci. (Phys.), Prof., University of Marches, Ancona, Italy
Zheng YongTing – Dr. Sci., Prof., Harbin Institute of Technology, Harbin, P.R. China
F. Zhengyi – Dr. Sci., Prof., Wuhan University of Technology, Wuhan, P.R. China

---

Редакция журнала

Адрес: 119049, Москва,
Ленинский пр-т, 4, стр. 1. НИТУ МИСИС

Тел.: +7 (495) 638-45-35. *Эл. почта:* izv.vuz@misis.ru

Свидетельство о регистрации № **ФС77-27955** от 12.04.2007 г.
Перерегистрация 25.09.2020 г. **ПИ № ФС77-79230**

ПМ и ФП ИЗВЕСТИЯ ВУЗОВ © НИТУ МИСИС, Москва, 2025

Статьи доступны под лицензией Creative Commons Attribution Non-Commercial No Derivatives

Ведущий редактор: О.В. Соснина
Выпускающий редактор: А.А. Кудинова
Дизайн и верстка: В.В. Расенецъ

Подписано в печать 21.02.2025. Формат 60×90 $^1/_8$
Бум. офсетная № 1. Печать цифровая. Усл. печ. л. 9,00
Заказ 21935. Цена свободная
Отпечатано в типографии Издательского Дома МИСИС
119049, г. Москва, Ленинский пр-т, стр. 1
Тел./факс: +7 (499) 236-76-17

Contents

Production Processes and Properties of Powders

Refractory, Ceramic, and Composite Materials

Nanostructured Materials and Functional Coatings

Содержание

Процессы получения и свойства порошков

Тугоплавкие, керамические и композиционные материалы

Наноструктурированные материалы и функциональные покрытия

Production Processes and Properties of Powders
Процессы получения и свойства порошков

UDC 621.762.34

https://doi.org/10.17073/1997-308X-2025-2-5-14

Research article
Научная статья

Comparison of properties of hard magnetic isotropic powder-processed Fe–Cr–Co alloys doped with titanium and titanium hydride

A. S. Ustyukhin[1], V. A. Zelensky[1], I. M. Milyaev[1],
D. Yu. Kovalev[2], V. S. Shustov[1], M. I. Alymov[1, 2]

[1] **A.A. Baikov Institute of Metallurgy and Materials Science of the Russian Academy of Sciences**
49 Leninskiy Prosp., Moscow 119334, Russia
[2] **Merzhanov Institute of Structural Macrokinetics and Materials Science of the Russian Academy of Sciences**
8 Academician Osipyan Str., Chernogolovka, Moscow Region 142432, Russia

fcbneo@yandex.ru

Abstract. This study presents a comparative investigation of the density, phase composition, magnetic, and mechanical properties of isotropic powder metallurgy alloys Fe–28Cr–15Co and Fe–32Cr–22Co doped with 2 wt. % titanium introduced either as conventional titanium powder (PTS-1 grade) or as titanium hydride powder. The sample fabrication process included powder blend preparation, compaction, vacuum sintering, quenching, and heat treatment aimed at developing magnetic properties. The use of titanium hydride powder resulted in an increase in residual porosity from 2 to 4 %. A significant difference in the phase composition of the alloys after sintering was observed: the structure of the Fe–28Cr–15Co–2Ti alloy consisted of a BCC α-phase solid solution and tetragonal σ-phase inclusions, while Fe–32Cr–22Co–2Ti exhibited a σ-phase solid solution matrix with FCC γ-phase inclusions. After heat treatment, all alloys developed a BCC α-phase solid solution structure. In the samples containing titanium hydride, minor traces of an impurity phase – most likely a hydride of a titanium–chromium intermetallic compound – were also detected. Samples prepared using PTS-1 titanium powder exhibited higher residual induction values (B_r up to 0.84 and 0.82 T for Fe–28Cr–15Co–2Ti and Fe–32Cr–22Co–2Ti, respectively) compared to those containing titanium hydride (up to 0.80 and 0.79 T, respectively), which is attributed to differences in residual porosity. On the other hand, samples with titanium hydride powder showed higher coercivity values (H_c up to 41.1 and 57.2 kA/m for Fe–28Cr–15Co–2Ti and Fe–32Cr–22Co–2Ti, respectively) compared to those with titanium powder (up to 38.4 and 49.2 kA/m, respectively). The maximum energy product ($(BH)_{max}$) reached 11.0–11.5 kJ/m^3 for Fe–28Cr–15Co–2Ti and 14.0–14.5 kJ/m^3 for Fe–32Cr–22Co–2Ti, with virtually no dependence on the titanium source. The compression stress–strain curves for alloys with different titanium sources were nearly identical. Alloys of the Fe–32Cr–22Co–2Ti composition exhibited higher yield strength values ($\sigma_{0.2}$ = 1200–1400 MPa) compared to Fe–28Cr–15Co–2Ti alloys ($\sigma_{0.2}$ = 1000 MPa). All materials studied in this work demonstrated ductility.

Keywords: powder metallurgy, heat treatment, Fe–Cr–Co alloys, doping, porosity, magnetic properties, mechanical properties

Acknowledgements: This work was financially supported by the Russian Science Foundation, Project No. 24-29-00323.

For citation: Ustyukhin A.S., Zelensky V.A., Milyaev I.M., Kovalev D.Yu., Shustov V.S., Alymov M.I. Comparison of properties of hard magnetic isotropic powder-processed Fe–Cr–Co alloys doped with titanium and titanium hydride. *Powder Metallurgy and Functional Coatings*. 2025;19(2):5–14. https://doi.org/10.17073/1997-308X-2025-2-5-14

Сравнение характеристик магнитотвердых порошковых изотропных Fe–Cr–Co-сплавов, легированных титаном и гидридом титана

А. С. Устюхин[1] ✉, В. А. Зеленский[1], И. М. Миляев[1],
Д. Ю. Ковалев[2], В .С. Шустов[1], М. И. Алымов[1, 2]

[1] **Институт металлургии и материаловедения им. А.А. Байкова Российской академии наук**
Россия, 119334, г. Москва, Ленинский пр-т, 49
[2] **Институт структурной макрокинетики и проблем материаловедения**
им. А.Г. Мержанова Российской академии наук
Россия, 142432, Московская обл., г. Черноголовка, ул. Акад. Осипьяна, 8

✉ fcbneo@yandex.ru

Аннотация. В работе проведено сравнительное исследование плотности, фазового состава, магнитных и механических свойств изотропных порошковых сплавов Fe–28Cr–15Co и Fe–32Cr–22Co, легированных 2 мас. % титана в виде обычного порошка титана ПТС-1 и порошка гидрида титана. Процесс получения образцов состоял из приготовления исходной смеси порошков, прессования, спекания в вакууме, закалки и термической обработки для формирования магнитных свойств. Использование порошка гидрида титана привело к повышению остаточной пористости образцов с 2 до 4 %. Было отмечено существенное отличие фазового состава сплавов после спекания: структура образца Fe–28Cr–15Co–2Ti состояла из твердого раствора ОЦК α-фазы и включений тетрагональной σ-фазы, а Fe–32Cr–22Co–2Ti – из твердого раствора σ-фазы и включений ГЦК γ-фазы. После термической обработки структура всех сплавов представляла собой твердый раствор ОЦК α-фазы. В образцах с гидридом титана были также обнаружены малые следы примесной фазы, которая, вероятнее всего, является гидридом интерметаллического соединения титана и хрома. Образцы, в которых использовался порошок титана ПТС-1, имели более высокие значения остаточной индукции (B_r до 0,84 и 0,82 Тл у сплавов Fe–28Cr–15Co–2Ti и Fe–32Cr–22Co–2Ti соответственно) по сравнению с образцами, содержащими гидрид титана (до 0,8 и 0,79 Тл соответственно), что связано с разницей в остаточной пористости. С другой стороны, образцы с порошком гидрида титана имели более высокие показатели коэрцитивной силы (H_c до 41,1 и 57,2 кА/м у сплавов Fe–28Cr–15Co–2Ti и Fe–32Cr–22Co–2Ti соответственно) по сравнению с образцам, содержащими с порошок титана (до 38,4 и 49,2 кА/м соответственно). Наиболее высокие значения максимального энергетического произведения $(BH)_{max}$ составили 11,0–11,5 кДж/м^3 у сплавов Fe–28Cr–15Co–2Ti и 14,0–14,5 кДж/м^3 у Fe–32Cr–22Co–2Ti и практически не зависели от типа введенного титана. Кривые деформирования при сжатии сплавов с разными источниками титана были практически идентичны. Образцы состава Fe–32Cr–22Co–2Ti имели более высокие значения предела текучести ($\sigma_{0,2}$ = 1200÷1400 МПа) по сравнению со сплавами Fe–28Cr–15Co–2Ti ($\sigma_{0,2}$ = 1000 МПа). Все исследованные в работе материалы оказались пластичными.

Ключевые слова: порошковая металлургия, термическая обработка, Fe–Cr–Co-сплавы, легирование, пористость, магнитные свойства, механические свойства

Благодарности: Работа выполнена при финансовой поддержке РНФ, проект № 24-29-00323.

Для цитирования: Устюхин А.С., Зеленский В.А., Миляев И.М., Ковалев Д.Ю., Шустов В.С., Алымов М.И. Сравнение характеристик магнитотвердых порошковых изотропных Fe–Cr–Co-сплавов, легированных титаном и гидридом титана. *Известия вузов. Порошковая металлургия и функциональные покрытия*. 2025;19(2):5–14.
https://doi.org/10.17073/1997-308X-2025-2-5-14

Introduction

Hard magnetic alloys are among the most important materials in modern manufacturing, and the demand for them continues to grow. However, the majority of such alloys have high production costs due to the expensive components they contain, such as rare-earth metals and cobalt. Fe–Cr–Co-based hard magnetic materials contain less cobalt and therefore represent a more economical alternative. These materials exhibit a sufficient level of magnetic properties, although they are inferior in this regard to many other magnetic systems [1–3]. The main advantages of Fe–Cr–Co alloys include the highest ductility among all hard magnetic materials, high strength and corrosion resistance, thermal stability, and a wide operating temperature range [4–8]. Recent studies on Fe–Cr–Co alloys have increasingly employed various approaches, primarily based on powder metallurgy and additive manufacturing technologies [9–18]. There is also ongoing research into the characteristics of magnetic films based on these alloys, which are used in non-contact sensors for various devices [19; 20].

In Fe–Cr–Co hard magnetic alloys, spinodal decomposition occurs at temperatures around 650 °C, during which the body-centered cubic (BCC) α-phase separates into two BCC phases, α_1 and α_2, differing in chemical composition. During heat treatment – specifically, slow cooling from ~650 °C – ferromagnetic α_1-phase particles become uniformly distributed in the weakly magnetic α_2-phase matrix, leading to the development of magnetic properties in the alloy [21–23]. The parameters of the heat treatment process require careful control, as prolonged annealing or slow cooling can result in the formation of an equilibrium nonmagnetic σ-phase with a tetragonal crystal structure [24].

The properties of Fe–Cr–Co alloys can be modified by introducing various alloying elements, such as Mo, Si, W, Ti, and others [25–28]. When using powder metallurgy methods, a number of additional factors must be considered for alloying additives, including their solubility in the solid solution of the base elements (Fe, Cr, and Co), their reactivity with oxygen from the air trapped in the pores of the green compacts, and the characteristics of the initial powders. As shown in our experiments, the properties of the resulting material depend on the form in which the doping elements are introduced into the initial powder mixture [29].

The present study focuses on a comparative investigation of the properties of isotropic powder metallurgy Fe–Cr–Co alloys doped with titanium introduced either as conventional titanium powder or as titanium hydride powder. Dehydrogenation of the latter begins at approximately 450 °C and is expected to occur during the heating stage and throughout the sintering process. The study was conducted on alloys with the following compositions (wt. %): Fe–28Cr–15Co and Fe–32Cr–22Co, representing medium and high cobalt contents, respectively. Each alloy was doped with 2 wt. % of the above-mentioned titanium powders. The density, phase composition, as well as the magnetic and mechanical properties of the resulting compositions were investigated.

Materials and methods

To prepare the initial powder blends for the Fe–Cr–Co alloys, elemental powders of iron (carbonyl iron, grade VS), chromium (grade PX-1M), and cobalt (grade PK-1) with particle sizes of $d < 25$ µm were used. Titanium was introduced into the system in two forms: titanium powder (PTS-1 grade) with $d < 45$ µm, and titanium hydride powder obtained by hydrogenating titanium sponge (grade TG-100, GOST 17746–96), followed by milling to a powder with $d < 45$ µm. Depending on the alloy composition (Fe–28Cr–15Co and Fe–32Cr–22Co) and the titanium source, the materials are hereafter designated as Kh28K15T_H, Kh28K15T_P, Kh32K22T_H, and Kh32K22T_P, where the subscripts "H" and "P" indicate titanium hydride and titanium powder (PTS-1), respectively. The powders were mixed in a Turbula shaker mixer C2.0 (Russia) for 300 min. For every 100 g of powder blend, 200 g of 3 mm diameter steel balls were added to the mixing container. Cylindrical green compacts weighing 20 g and measuring 13.6 mm in diameter were formed using a Knuth HP15 hydraulic press (Germany) under a compaction pressure of 600 MPa. The compacts were then sintered in a ShSV-1.2.5/25I1 electric vacuum furnace (Russia) at a pressure below 10^{-2} Pa and a temperature of 1350 °C, with an isothermal hold time of 2.5 h. After sintering, the density of the samples was determined using the hydrostatic weighing method in distilled water.

Subsequently, the alloys were heated to 1300 °C and quenched in water. After quenching, heat treatment was performed in a tube furnace to achieve a high-coercivity state. For each sample, four heat treatment modes were tested by varying the initial temperature (t_1). The heat treatment process consisted of the following three stages:

1) isothermal holding for 40 min at $t_1 = 630 \div 655$ °C;

2) cooling by 60 °C from t_1 at a rate of $v_1 = 20$ °C/h;

3) cooling to 500 °C at a rate of $v_2 = 8$ °C/h.

No external magnetic field was applied during the heat treatment.

Microscopic investigations were conducted using a TESCAN VEGA3 scanning electron microscope (Czech Republic). Elemental composition was analyzed by energy-dispersive spectroscopy (EDS) with an X-Act microanalyzer (Oxford Instruments, UK). The phase composition of the samples was examined by *X*-ray diffraction (XRD) using a Difrey-401 diffractometer (Russia) with CrK_α radiation, in the 2θ range of 35 to 125°. Magnetic hysteresis properties were measured using a Permagraph L hysteresisgraph (Magnet-Physik, Germany). Compression tests were performed using an Instron 3382 testing machine (Instron, USA) at a loading rate of 1 mm/min. For testing, cylindrical samples were machined to a diameter of 7 mm and a height of 15 mm.

Results and discussion

Table 1 presents the density values (ρ) of the titanium-doped powder Fe–Cr–Co alloys after sintering, as measured by the hydrostatic weighing method. The theoretical density (ρ_t) was calculated based on the principle of additivity: the density of each alloy component was multiplied by its respective weight fraction, and the results were summed. Based on these

Table 1. **Density measurements of the investigated alloys with different titanium sources after sintering**

Таблица 1. **Результаты измерения плотности исследуемых сплавов с разными источниками титана после спекания**

Alloy	ρ, g/cm^3	ρ_t, g/cm^3	ρ_{rel}, %
Kh28K15T_H	7.45–7.48	7.77	95.9–96.3
Kh28K15T_P	7.59–7.68	7.77	97.7–98.8
Kh32K22T_H	7.53–7.59	7.81	96.4–97.1
Kh32K22T_P	7.66–7.74	7.81	98.1–99.1

data, the relative density (ρ_{rel}) and residual porosity of the sintered samples were determined.

The results revealed noticeable differences in the density of the samples depending on whether titanium powder or titanium hydride powder was used for doping. According to the measured ρ values, the use of titanium hydride powder as the titanium source leads to an increase in porosity – up to 3.0–3.5 % for Kh32K22T_H samples and up to 4 % for Kh28K15T_H.

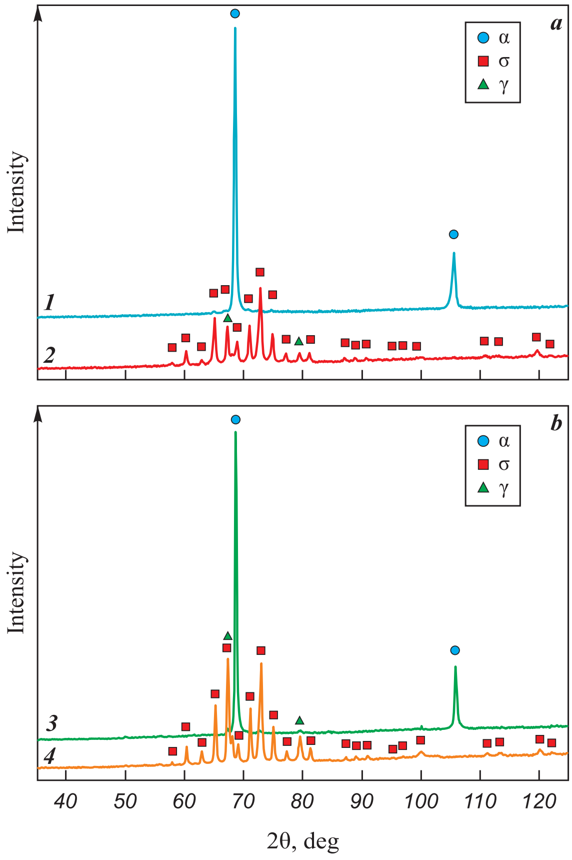

Fig. 1. *X*-ray diffraction patterns of Fe–Cr–Co alloys doped with titanium powder (***a***) and titanium hydride (***b***)
1 – Kh28K15T_H, ***2*** – Kh32K22T_H, ***3*** – Kh28K15T_P, ***4*** – Kh32K22T_P

Рис. 1. Дифрактограммы Fe–Cr–Co-сплавов, легированных порошком титана (***a***) и гидридом титана (***b***)
1 – Х28К15Т_Г, ***2*** – Х32К22Т_Г, ***3*** – Х28К15Т_П, ***4*** – Х32К22Т_П

According to our previous studies on powder Fe–Cr–Co alloys under the same sintering conditions, the relative density ρrel typically reaches approximately 98 % [11]. When titanium powder is used, the alloys exhibit a relative density of approximately 98–99%.

Fig. 1 shows the results of phase composition analysis of the alloys doped with PTS-1 titanium powder and titanium hydride immediately after sintering. Fig. 2 presents, as an example, microstructure images of the Kh28K15T_P and Kh32K22T_P alloys, along with the results of elemental concentration mea-

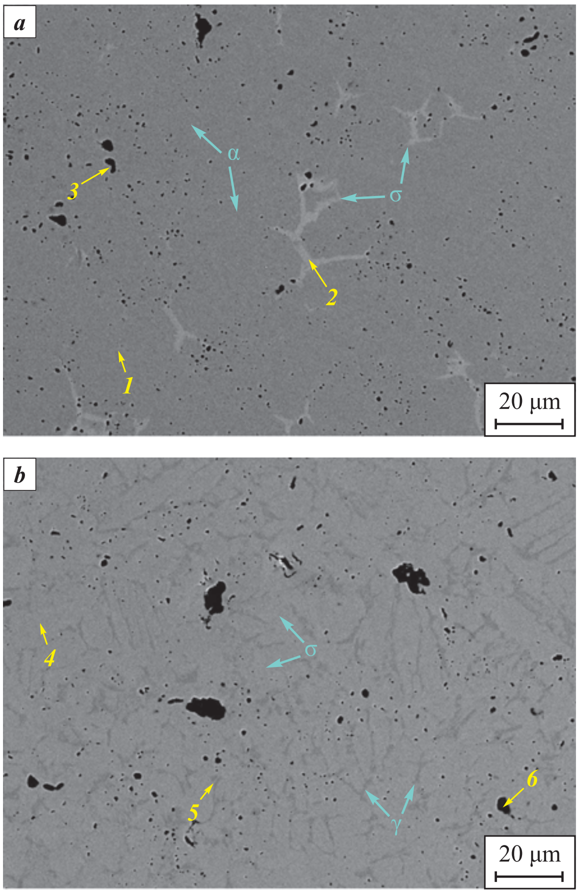

Spectrum	Elemental composition, wt. %				
	Fe	Cr	Co	Ti	O
1	54.9	28.7	15.3	1.0	–
2	53.3	29.8	15.4	1.5	–
3	6.3	4.2	1.7	56.4	31.4
4	41.4	34.1	22.2	2.2	–
5	50.2	25.7	23.4	0.7	–
6	0.7	0.9	0.3	62.2	35.9

c

Fig. 2. SEM images of microsections of alloys Kh28K15T_P (***a***) and Kh32K22T_P (***b***) after sintering, and EDS analysis results at points ***1***–***6*** (***c***)

Рис. 2. РЭМ-фотографии микрошлифов сплавов Х28К15Т_П (***a***) и Х32К22Т_П (***b***) после спекания и результаты ЭДС-анализа в точках ***1***–***6*** (***c***) surements obtained by EDS for different structural constituents.

According to the obtained diffraction patterns (Fig. 1), the phase composition of the Fe–28Cr–15Co and Fe–32Cr–22Co alloys differs significantly immediately after sintering. The structure of the Kh28K15T_H and Kh28K15T_P samples consists of a BCC α-phase solid solution and inclusions of the tetragonal σ-phase. In the microstructure image of the Kh28K15T_P alloy (Fig. 2, *a*), the σ-phase inclusions appear as white bands within the gray α-phase matrix, mainly located along grain boundaries. This is consistent with numerous studies indicating that σ-phase inclusions typically form at grain boundaries. The elemental composition of the phases is relatively similar, although the σ-phase inclusions exhibit a slightly elevated chromium concentration.

The structures of the Kh32K22T_H and Kh32K22T_P alloys consist of a σ-phase solid solution and FCC γ-phase inclusions (Fig. 1). No traces of the α-phase are observed in these samples, which can be attributed to the polymorphic nature of the α → σ transformation during cooling of Fe–Cr–Co alloys with elevated Cr and Co contents. It should be noted that the diffraction peaks in the patterns of Kh32K22T_H and Kh32K22T_P may also indicate the presence of two distinct σ-phases based on Fe–Cr and Co–Cr systems, which are compositionally similar, as well as two γ-phases. The peaks of these phases may partially or fully overlap, which complicates their identification.

In the microstructure image of the Kh32K22T_P alloy (Fig. 2, *b*), in contrast to Kh28K15T_P, the σ-phase–based matrix appears as the brightest structural component, while all inclusions are darker. According to the EDS data (Fig. 2, *c*), the inclusions show increased Fe content and reduced Cr content, which confirms the presence of the γ-phase in the sample. All oxide inclusions observed in pore regions in both alloys are titanium oxides.

X-ray diffraction patterns of the Fe–28Cr–15Co and Fe–32Cr–22Co alloys containing different titanium sources after heat treatment are shown in Fig. 3, and their microstructure images are presented in Fig. 4. The structure of all samples represents a BCC α-phase solid solution (Fig. 3). The spinodal decomposition into α_1 and α_2 phases that occurs during thermal treatment was not detected in the diffraction patterns due to peak broadening. In the patterns of Kh28K15T_H and Kh32K22T_H, diffraction peaks of a secondary phase are also present, which may correspond to iron or cobalt oxides. However, according to earlier EDS analysis and elemental mapping [30], all oxide inclusions in the structure are titanium oxides. In addition, among the main components of Fe–Cr–Co alloys, chromium is known to oxidize first.

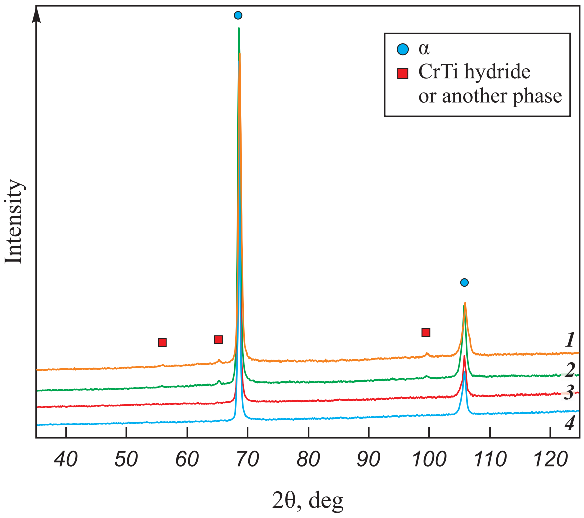

Fig. 3. *X*-ray diffraction patterns of Fe–Cr–Co alloys doped with titanium after heat treatment

1 – Kh32K22T_H, ***2*** – Kh28K15T_H, ***3*** – Kh32K22T_P, ***4*** – Kh28K15T_P

Рис. 3. Дифрактограммы сплавов системы Fe–Cr–Co с добавками титана после термической обработки

1 – Х32К22Т_Г, ***2*** – Х28К15Т_Г, ***3*** – Х32К22Т_П, ***4*** – Х28К15Т_П

Additional analysis indicated that the diffraction peaks of the secondary phase may also correspond to a hydride of a Ti–Cr-based intermetallic compound, which may partly account for the formation of the porous structure observed in the samples containing it (Fig. 4, *a*, *b*). However, the initial amount of titanium hydride in the system is small. Hydrides of Ti–Cr-based compounds are also characterized by low stability, so it cannot be conclusively identified which specific compound is responsible for the secondary phase peaks observed in the obtained alloys. Notably, these peaks may already be present in the diffraction patterns after sintering (see Fig. 1, *b*); however, at positions such as 2θ = 66° and 100°, they are overlapped by the σ-phase peaks, which further complicates their identification.

Microstructural analysis of the samples revealed noticeable differences in the porous structure depending on the titanium source. As seen in Fig. 4, *a*, *b*, the samples containing titanium hydride exhibit numerous elongated dark inclusions forming a branched porous network, indicative of incomplete sintering. This type of structure is considered intermediate and may have resulted from incomplete dehydrogenation of titanium during the sintering heating process. Rapid healing of open pores may have trapped hydrogen within the material, thereby impeding the removal of residual porosity and promoting the formation of elongated inclusions under internal pressure.

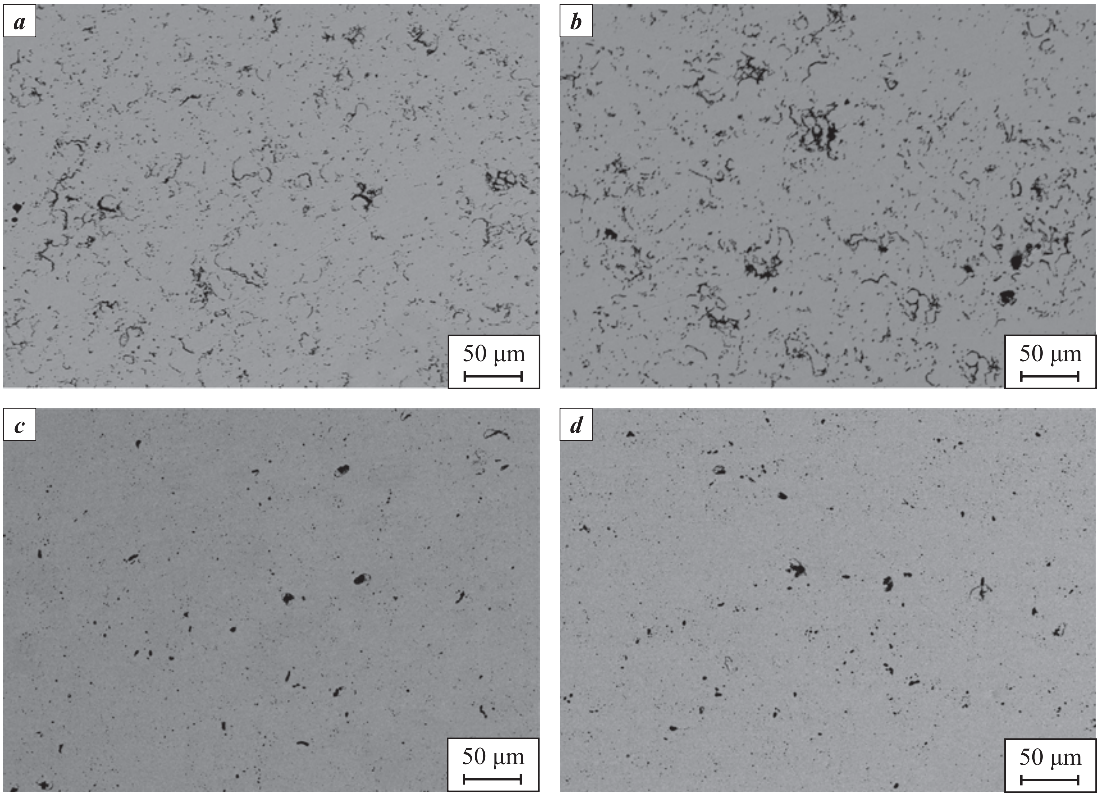

Fig. 4. SEM images of microsections of alloys Kh28K15T_H (***a***), Kh32K22T_H (***b***), Kh28K15T_P (***c***), and Kh32K22T_P (***d***) after heat treatment

Рис. 4. РЭМ-фотографии микрошлифов сплавов Х28К15Т_Г (***a***), Х32К22Т_Г (***b***), Х28К15Т_П (***c***) и Х32К22Т_П (***d***) после термической обработки

In the alloys with PTS-1 titanium powder, the pore structure is characterized by dark inclusions 5–10 μm in size, fairly uniformly distributed throughout the matrix, along with significantly smaller pores approximately 1–2 μm in size (Fig. 4, *c*, *d*). The alloys with titanium hydride (Fig. 4, *a*, *b*) exhibit a visibly higher number and volume of inclusions compared to those with titanium powder (Fig. 4, *c*, *d*), which correlates with the lower relative density values measured for these samples. In addition, the smaller inclusions in Fig. 4, *c*, *d* tend to cluster, suggesting incomplete pore closure during sintering.

The magnetic property analysis revealed significant differences in B_r, H_c, and $(BH)_{\max}$ values depending on the titanium source. The heat treatment dependence of the magnetic properties is shown in Fig. 5. The use of titanium hydride led to increased maximum coercivity (H_c up to 41.1 and 57.2 kA/m for Kh28K15T_H and Kh32K22T_H, respectively) and reduced residual induction (B_r up to 0.8 and 0.79 T), compared to Kh28K15T_P and Kh32K22T_P alloys (up to 0.84 and 0.82 T, respectively). The lower B_r values are mainly attributed to increased porosity in the samples with titanium hydride.

The temperature dependence of residual induction (Fig. 5, *a*, *b*) is nearly identical for all alloys: as t_1 increases, Br values decrease monotonically, similar to the behavior observed in many other isotropic Fe–Cr–Co alloys. The observed increase in coercivity is likely associated with a higher density of defects and internal stresses in the structure due to incomplete titanium dehydrogenation. The temperature dependence of H_c for all alloys exhibits a maximum at $t_1 \sim 645{\div}650$ °C (Fig. 5, *c*, *d*). For both H_c and B_r, even a 5 °C change in t_1 can have a pronounced effect on their values, highlighting the sensitivity of spinodal decomposition and the final magnetic properties of the alloys to the processing conditions. The $(BH)_{\max}$ curves (Fig. 5, *e*, *f*) for alloys with different titanium sources are relatively similar, as the improvement in one magnetic parameter is offset by the decline in another. The highest values of $(BH)_{\max}$ reached 11.0–11.5 kJ/m^3 for both Kh28K15T_H and Kh28K15T_P, and 14.0–14.5 kJ/m^3 for Kh32K22T_H and Kh32K22T_P.

A comparison of the mechanical properties of the investigated Fe–Cr–Co alloys containing different titanium sources was carried out. The samples with the best set of magnetic properties were subjected to compression testing. The experimental stress–strain curves are shown in Fig. 6, and the results of mechanical property evaluation are presented in Table 2. The tests were conducted up to a strain of 25 % (ε).

Analysis of the stress–strain curves (Fig. 6) shows that all the titanium-doped alloys investigated in this study exhibit good ductility. With the exception of Kh32K22T_P, all other samples underwent deformation up to a strain of 25 % without fracture. An increase in chromium and cobalt content in the alloys resulted in a rise in yield strength ($\sigma_{0.2}$) from 1000 to 1200–1400 MPa (Table 2). At the same time, the stress–strain curves of the alloys with different titanium sources show only minor differences, despite noticeable variations in porosity and magnetic properties (Fig. 6).

Table 2. **Results of yield strength $\sigma_{0.2}$, compressive strength σ_c, and fracture strain ε_f measurements for the investigated alloys containing different titanium sources**

Таблица 2. **Результаты определения предела текучести ($\sigma_{0,2}$), прочности на сжатие (σ_c) и деформации при разрушении (ε_f) исследуемых сплавов, содержащих разные источники титана**

Alloy	$\sigma_{0.2}$, MPa	σ_c, MPa	ε_f (100 %)
Kh28K15T_H	990 ± 30	>1580	>25.0
Kh28K15T_P	1000 ± 30	>1650	>25.0
Kh32K22T_H	1400 ± 40	>1850	>25.0
Kh32K22T_P	1240 ± 30	1850 ± 10	23.6

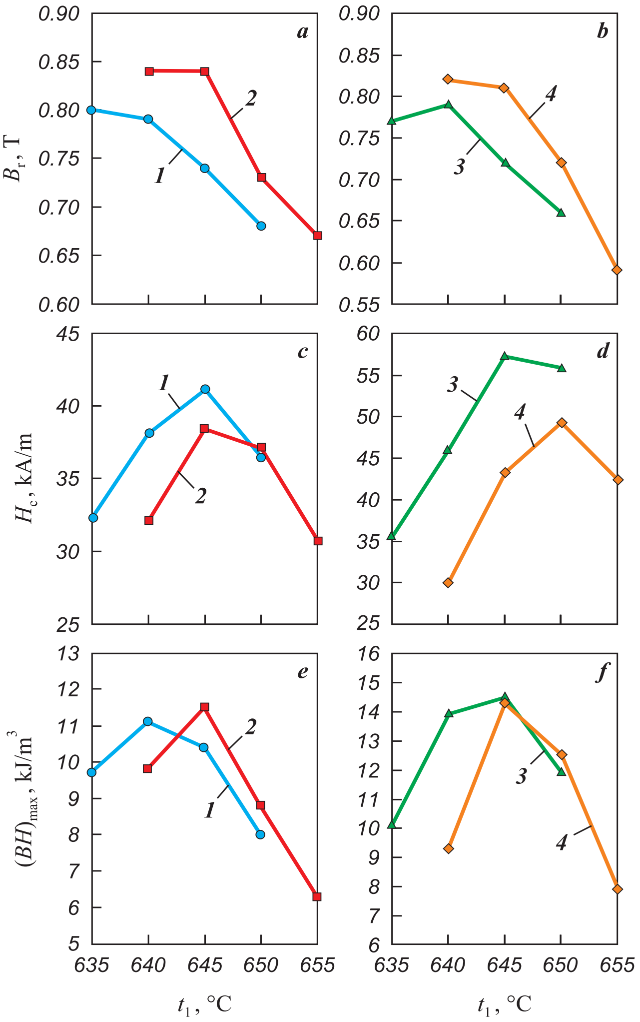

Fig. 5. Dependencies of residual induction (***a***, ***b***), coercivity (***c***, ***d***), and maximum energy product (***e***, ***f***) on the heat treatment t_1 for the investigated Fe–Cr–Co alloys containing different titanium sources

1 – Kh28K15T_H, ***2*** – Kh28K15T_P, ***3*** – Kh32K22T_H, ***4*** – Kh32K22T_P

Рис. 5. Зависимости остаточной индукции (***a***, ***b***), коэрцитивной силы (***c***, ***d***) и максимального энергетического произведения (***e***, ***f***) от температуры термообработки (t_1) исследуемых сплавов системы Fe–Cr–Co, содержащих разные источники титана

1 – Х28К15Т_Г, ***2*** – Х28К15Т_П, ***3*** – Х32К22Т_Г, ***4*** – Х32К22Т_П

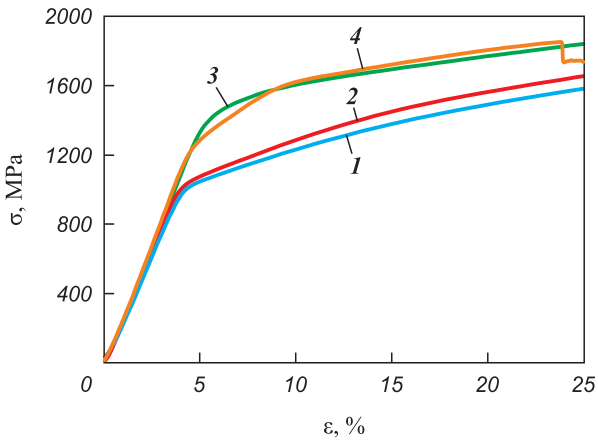

Fig. 6. Stress–strain curves of the investigated Fe–Cr–Co alloy samples containing different titanium sources

1 – Kh28K15T_H, ***2*** – Kh28K15T_P, ***3*** – Kh32K22T_H, ***4*** – Kh32K22T_P

Рис. 6. Кривые деформирования образцов исследуемых сплавов системы Fe–Cr–Co, содержащих разные источники титана

1 – Х28К15Т_Г, ***2*** – Х28К15Т_П, ***3*** – Х32К22Т_Г, ***4*** – Х32К22Т_П

Conclusions

Based on the results of this study on powder-processed hard magnetic Fe–Cr–Co alloys doped with titanium from different sources, the following conclusions can be drawn.

1. Doping with titanium hydride powder leads to an increase in residual porosity from 2 to 4 %. Phase composition analysis revealed the presence of a secondary phase, most likely a hydride of a Ti–Cr-based intermetallic compound. Microstructural analysis showed that the pore structure in the alloys containing titanium hydride is branched, which is typical of incomplete sintering. This suggests that the increased porosity is primarily due to incomplete dehydrogenation of titanium hydride during the heating stage of sintering.

2. Magnetic property measurements demonstrated that samples doped with PTS-1 titanium powder exhibited higher residual induction values (B_r up to 0.84 T) compared to those doped with titanium hydride, which is attributed to lower residual porosity. Conversely, the titanium hydride–doped samples showed higher coercivity values (H_c up to 57.2 kA/m).

3. Compression tests showed that, despite differences in density and magnetic properties, the stress–strain curves of alloys with different titanium sources were nearly identical. The Fe–32Cr–22Co–2Ti samples exhibited higher yield strength ($\sigma_{0.2}$ = 1200÷1400 MPa) compared to the Fe–28Cr–15Co–2Ti samples ($\sigma_{0.2}$ = 1000 MPa). All titanium-doped alloys investigated in this study showed good ductility, with most of them deforming up to 25 % strain without fracturing.

References / Список литературы

1. Kaneko H., Homma M., Minowa T. Effect of V and V+Ti additions on the structure and properties of Fe–Cr–Co ductile magnet alloys. *IEEE Transactions on Magnetics*. 1976;12(6):977–979. https://doi.org/10.1109/TMAG.1976.1059239

2. Tao S., Ahmad Z., Zhang P., Zheng X., Wang F., Xu X. Enhancement of magnetic and microstructural properties in Fe–Cr–Co–Mo–V–Zr–Y permanent magnetic alloy. *Journal of Magnetism and Magnetic Materials*. 2019;484: 88–94. https://doi.org/10.1016/j.jmmm.2019.04.004

3. Perminov A.S., Maslennikov S.O., Lileev A.S., Shuvaeva E.A., Stolyarov V.L., Zhukov D.G. Concentration distribution of elements and variation in phase composition during solid-solution decomposition in Fe–Cr–Co alloy. *Steel in Translation*. 2010; 40(3):216–218. https://doi.org/10.3103/S0967091210030058

Перминов А.С., Масленников С.О., Лилеев А.С., Шуваева Е.А., Столяров В.Л., Жуков Д.Г. Моделирование пространственного распределения концентраций элементов и кинетики изменения количества фаз при распаде твердого раствора в сплаве Fe–Cr–Co. *Известия вузов. Черная металлургия*. 2010;53(3):32–34.

4. Belozerov E.V., Mushnikov N.V., Ivanova G.V., Shchegoleva N.N., Serikov V.V., Kleinerman N.M., Vershinin A.V., Uimin M.A. High-strength magnetically hard Fe–Cr–Co-based alloys with reduced content of chromium and cobalt. *The Physics of Metals and Metallography*. 2012;113(4):319–325. https://doi.org/10.1134/S0031918X12040023

Белозеров Е.В., Мушников Н.В., Иванова Г.В., Щеголева Н.Н., Сериков В.В., Клейнерман Н.М., Вершинин А.В., Уймин М.А. Высокопрочные магнитотвердые сплавы на основе Fe–Cr–Co с пониженным содержанием хрома и кобальта. *Физика металлов и металловедение*. 2012;113(4):339–346.

5. Korneva A., Korznikova G., Berent K., Korznikov A., Kashaev R., Bogucka J., Sztwiertnia K. Microstructure evolution and magnetic properties of hard magnetic FeCr22Co15 alloy subjected to tension combined with torsion. *Journal of Alloys and Compounds*. 2014;615(S1):S300–S303. https://doi.org/10.1016/j.jallcom.2014.01.207

6. Han X.H., Bu S.J., Wu X., Sun J.B., Zhang Y., Cui C.X. Effects of multi-stage aging on the microstructure, domain structure and magnetic properties of Fe-24Cr-12Co-1.5Si ribbon magnets. *Journal of Alloys and Compounds*. 2017; 694:103–110. https://doi.org/10.1016/j.jallcom.2016.09.316

7. Xiang Z., Zhang L., Xin Y., An B., Niu R., Mardani M., Siegrist T., Lu J., Goddard R.E., Man T., Wang E., Han K. Ultrafine microstructure and hardness in Fe–Cr–Co alloy induced by spinodal decomposition under magnetic field. *Materials and Design*. 2021;199:109383. https://doi.org/10.1016/j.matdes.2020.109383

8. Gao Q. Gong M., Wang Y., Qu F., Huang J. Phase transformation and properties of Fe-Cr-Co alloys with low cobalt content. *Materials Transactions*. 2015;56(9):1491–1495. https://doi.org/10.2320/matertrans.M2015077

9. Efremov D.V., Gerasimova A.A. Production of Fe–Cr–Co-based magnets by selective laser sintering. *Steel in Translation*. 2021;51(10):688–692. https://doi.org/10.3103/s0967091221100028

Ефремов Д.Б., Герасимова А.А. Получение магнитов из материала системы Fe–Cr–Co методами селективного лазерного спекания. *Известия вузов. Черная металлургия*. 2021;64(10):721–727. https://doi.org/10.17073/0368-0797-2021-10-721-727

10. Marieva M.A., Shatsov A.A. Prediction of the concentration inhomogeneity of powder magnetic hard alloys based on the Fe–Cr–Co–Mo system and the effect of Sm additions on their magnetic properties. *Powder Metallurgy and Functional Coatings*. 2023;17(1):12-20. https://doi.org/10.17073/1997-308X-2023-1-12-20

Мариева М.А., Шацов А.А. Прогнозирование концентрационной неоднородности порошковых магнитотвердых сплавов на основе системы Fe–Cr–Co–Mo и влияние добавок Sm на их магнитные свойства. *Известия вузов. Порошковая металлургия и функциональные покрытия*. 2023;17(1):12–20 https://doi.org/10.17073/1997-308X-2023-1-12-20

11. Ustyukhin A.S., Ankudinov A.B., Zelensky V.A., Alymov M.I., Milyaev I.M., Vompe T.A. Synthesis, thermal treatment, and characterization of sintered hard magnetic Fe–30Cr–16Co alloy. *Journal of Alloys and Compounds*. 2022;902:163754. https://doi.org/10.1016/j.jallcom.2022.163754

12. Zhukov A.S., Kuznetsov P.A., Kamynin A.V., Gavrikov I.S., Barakhtin B.K. Multifractal analysis and magnetic properties of magnetically hard Fe–Cr–Co alloy produced by selective laser melting. *Russian Engineering Research*. 2021;41(4):325–328. https://doi.org/10.3103/S1068798X21040250

13. He Y., Zhang H., Su H., Shen P., Hou Y., Zhou D. In situ alloying of Fe–Cr–Co permanent magnet by selective laser melting of elemental iron, chromium and cobalt mixed

powders. *Metals*. 2022;12(10):1634.
https://doi.org/10.3390/met12101634

14. Mairhofer T., Arneitz S., Hofer F., Sommitsch C., Kothleitner G. Micro- and nanostructure of additively manufactured, in-situ alloyed, magnetic spinodal $Fe_{54}Cr_{31}Co_{15}$. *Journal of Materials Science*. 2023;58:7119–7135.
https://doi.org/10.1007/s10853-023-08445-z
15. Generalova K.N., Ryaposov I.V., Shatsov A.A. Effect of Mo and W additions on the magnetic hysteresis properties of a powder ridge alloy. *Metal Science and Heat Treatment*. 2020;61:657–662.
https://doi.org/10.1007/s11041-020-00474-8

    Генералова К.Н., Ряпосов И.В., Шацов А.А. Влияние добавок Mo и W на гистерезисные магнитные свойства порошкового гребневого сплава. *Металловедение и термическая обработка металлов*. 2019;(10):72–77.
    https://doi.org/10.30906/mitom.2019.10.72-77
16. Amini Rastabi R., Ghasemi A., Tavoosi M., Ramazani M. Magnetic features of Fe–Cr–Co alloys with tailoring chromium content fabricated by spark plasma sintering. *Journal of Magnetism and Magnetic Materials*. 2017;426:744–752. https://doi.org/10.1016/j.jmmm.2016.10.132
17. He Y., Hou Y., Shen P., Zhang H., Zhou D., Su H. Fabricating functionally graded Fe–Cr–Co permanent magnetic alloys via laser powder bed fusion. *Journal of Iron and Steel Research International*. 2024;31:729–737.
https://doi.org/10.1007/s42243-023-01088-z
18. Ajia S., Asa H., Toyoda Y., Sato M., Matsuura M., Tezuka N., Sugimoto S. Development of an alternative approach for electromagnetic wave absorbers using Fe–Cr–Co alloy powders. *Journal of Alloys and Compounds*. 2022;903:163920.
https://doi.org/10.1016/j.jallcom.2022.163920
19. Liu J.T., Xu X.L., Feng G.N., Yang X.Y., Zhao D., Zuo M.G., Liu C.Y., Feng C., Liu S., Li B.H., Yu G.H. Coercivity modulation of FeCoCrMoTi films by artificial magnetic phase defects engineering based on multilayer structure. *Acta Materialia*. 2023;259:119241.
https://doi.org/10.1016/j.actamat.2023.119241
20. Zhao D., Xu X.L., Cao Y., Zhai M.Y., Lu S., Kang P., Liu J.T., Yang X.Y., Zuo M.G., Liu C.Y., Hu W.Y., Ma X.J., Yu G.H. Improving magnetic properties of FeCrCo films by facilitating the internal α-γ phase transition through Pt diffusion. *Acta Materialia*. 2025;282:120469.
https://doi.org/10.1016/j.actamat.2024.120469
21. Perminov A.S., Maslennikov S.O., Lileev A.S., Shuvaeva E.A., Vvedenskii V.Y. Isothermal decomposition in Fe–Cr–Co alloy. *Steel in Translation*. 2009;39(9):755–756.
https://doi.org/10.3103/S0967091209090083

    Перминов А.С., Масленников С.О., Лилеев А.С., Шуваева Е.А., Введенский В.Ю. Моделирование изотермического распада в сплаве Fe–Cr–Co. *Известия вузов. Черная металлургия*. 2009;52(9):55–56.
22. Zhang L., Xiang Z., Li X., Wang E. Spinodal decomposition in Fe–25Cr–12Co alloys under the influence of high magnetic field and the effect of grain boundary. *Nanomaterials*. 2018;8(8):578.
https://doi.org/10.3390/nano8080578
23. Iwaizako H., Okugawa M., Saito K., Koizumi Y., Chiba A., Tachiya Y., Ohnuma M., Kuritani K. Spinodal decomposition in plastically deformed Fe–Cr–Co magnet alloy. *ISIJ International*. 2022;62(6):1268–1274.
https://doi.org/10.2355/isijinternational.ISIJINT-2021-441
24. Kozvonin V.A., Shatsov A.A., Ryaposov I.V., Generalova K.N., Spivak L.V. Phase transformations and properties of concentration-inhomogeneous magnetic materials based on the Fe–30%Cr–27%Co system. *Powder Metallurgy and Functional Coatings*. 2019;13(1):82–90. (In Russ.).
https://doi.org/10.17073/1997-308X-2019-1-82-90

    Козвонин В.А., Шацов А.А., Ряпосов И.В., Генералова К.Н., Спивак Л.В. Фазовые превращения и свойства концентрационно-неоднородных магнитных материалов на основе системы Fe–30%Cr–27%Co. *Известия вузов. Порошковая металлургия и функциональные покрытия*. 2019;13(1):82–90.
    https://doi.org/10.17073/1997-308X-2019-1-82-90
25. Ahmad Z., ul Haq A., Yan M., Iqbal Z. Evolution of phase, texture, microstructure and magnetic properties of Fe–Cr–Co–Mo–Ti permanent magnets. *Journal of Magnetism and Magnetic Materials*. 2012;324:2355–2359.
https://doi.org/10.1016/j.jmmm.2012.02.040
26. Tao S., Ahmad Z., Zhang P., Zheng X., Zhang S. Effects of Sm on structural, textural and magnetic properties of Fe–28Cr–20Co–3Mo–2V–2Ti hard magnetic alloy. *Journal of Alloys and Compounds*. 2020;816:152619.
https://doi.org/10.1016/j.jallcom.2019.152619
27. Ustyukhin A.S., Zelenskii V.A., Milyaev I.M., Shustov V.S., Yusupov V.S. Studies of properties of isotropic hard magnetic powder alloys Fe–30Cr–20Co–2Mo (Kh30K20M2) doped with niobium. *Steel in Translation*. 2022;52(10):996–1002.
https://doi.org/10.3103/S096709122210014X
28. Beltyukova M.A., Shatsov A.A. Phase transformations, microstructure formation, and magnetic properties of a hysteresis alloy based on the Fe–Cr–Co–Mo system doped with Sm, Zr, and Cu. *Powder Metallurgy and Functional Coatings*. 2024;18(4):35-44.
https://doi.org/10.17073/1997-308X-2024-4-35-44

    Бельтюкова М.А., Шацов А.А. Особенности фазовых превращений, формирования микроструктуры и магнитных свойств гистерезисного сплава на основе системы Fe–Cr–Co–Mo, легированного Sm, Zr и Cu. *Известия вузов. Порошковая металлургия и функциональные покрытия*. 2024;18(4):35–44.
    https://doi.org/10.17073/1997-308X-2024-4-35-44
29. Ustyukhin A.S., Zelensky V.A., Milyaev I.M., Alymov M.I., Ashmarin A.A., Ankudinov A.B., Sergienko K.V. Synthesis and magnetic hysteresis properties of an aluminum-doped isotropic hard-magnetic Fe–Cr–Co powder alloy. *Inorganic Materials: Applied Research*. 2024;15(2):480–488.
https://doi.org/10.1134/S2075113324020424
30. Ustyukhin A.S., Zelensky V.A., Milyaev I.M., Shustov V.S., Shibakova N.S. Influence of individual dopants on density and magnetic properties of isotropic hard magnetic Fe–28Cr–15Co alloy. *Stal'*. 2025;1:45-51. (In Russ.).

    Устюхин А.С., Зеленский В.А., Миляев И.М., Шустов В.С., Шибакова Н.С. Влияние индивидуальных легирующих добавок на плотность и магнитные свойства изотропного магнитотвердого сплава Fe–28Cr–15Co. *Сталь*. 2025;1:45-51.

Information about the Authors

Aleksei S. Ustyukhin – Cand. Sci. (Eng.), Junior Research Scientist at the Laboratory of Physical Chemistry of Surfaces and Ultrafine Powder Materials, A.A. Baikov Institute of Metallurgy and Materials Science of the Russian Academy of Sciences Russian Federation (IMET RAS)
ORCID: 0000-0003-1578-4883
E-mail: fcbneo@yandex.ru

Viktor A. Zelensky – Cand. Sci. (Phys.-Math.), Leading Researcher at the Laboratory of Physical Chemistry of Surfaces and Ultrafine Powder Materials, IMET RAS
ORCID: 0000-0002-4441-9132
E-mail: zelensky55@bk.ru

Igor M. Milyaev – Dr. Sci. (Eng.), Leading Researcher at the Laboratory of Plastic Deformation of Metallic Materials, IMET RAS
ORCID: 0000-0002-0591-2645
E-mail: imilyaev@mail.ru

Dmitry Yu. Kovalev – Dr. Sci. (Phys.-Math.), Head of the Laboratory of *X*-Ray Investigation, Merzhanov Institute of Structural Macrokinetic and Materials Science Russian Academy of Sciences (ISMAN)
ORCID: 0000-0002-8285-5656
E-mail: kovalev@ism.ac.ru

Vadim S. Shustov – Cand. Sci. (Eng.), Senior Research Scientist at the Laboratory of Physical Chemistry of Surfaces and Ultrafine Powder Materials, IMET RAS
ORCID: 0000-0001-6395-3747
E-mail: vshscience@mail.ru

Mikhail I. Alymov – Dr. Sci. (Eng.), Corresponding Member of RAS, Director of ISMAN, Head of the Laboratory of Physical Chemistry of Surfaces and Ultrafine Powder Materials, IMET RAS
ORCID: 0000-0001-6147-5753
E-mail: mialymov@mail.ru

Сведения об авторах

Алексей Сергеевич Устюхин – к.т.н., мл. науч. сотрудник лаборатории физикохимии поверхности и ультрадисперсных порошковых материалов Института металлургии и материаловедения им. А.А. Байкова Российской академии наук (ИМЕТ РАН)
ORCID: 0000-0003-1578-4883
E-mail: fcbneo@yandex.ru

Виктор Александрович Зеленский – к.ф.-м.н., вед. науч. сотрудник лаборатории физикохимии поверхности и ультрадисперсных порошковых материалов ИМЕТ РАН
ORCID: 0000-0002-4441-9132
E-mail: zelensky55@bk.ru

Игорь Матвеевич Миляев – д.т.н., вед. науч. сотрудник лаборатории пластической деформации металлических материалов ИМЕТ РАН
ORCID: 0000-0002-0591-2645
E-mail: imilyaev@mail.ru

Дмитрий Юрьевич Ковалев – д.ф-м.н., зав. лабораторией рентгеноструктурных исследований Института структурной макрокинетики и проблем материаловедения им. А.Г. Мержанова Российской академии наук (ИСМАН)
ORCID: 0000-0002-8285-5656
E-mail: kovalev@ism.ac.ru

Вадим Сергеевич Шустов – к.т.н., науч. сотрудник лаборатории физикохимии поверхности и ультрадисперсных порошковых материалов ИМЕТ РАН
ORCID: 0000-0001-6395-3747
E-mail: vshscience@mail.ru

Михаил Иванович Алымов – д.т.н., чл.кор. РАН, директор ИСМАН, зав. лабораторией физикохимии поверхности и ультрадисперсных порошковых материалов ИМЕТ РАН
ORCID: 0000-0001-6147-5753
E-mail: mialymov@mail.ru

Contribution of the Authors

A. S. Ustyukhin – defined the research objectives, performed electron microscopy analysis of the structure, participated in discussion of results, and wrote the manuscript.
V. A. Zelensky – research objectives, conducted powder mixing, pressing, sintering, and quenching of the samples, participated in the discussion of the results, and contributed to manuscript editing.
I. M. Milyaev – carried out heat treatment and magnetic property measurements.
D. Yu. Kovalev – performed *X*-ray phase analysis and participated in discussion of results.
V. S. Shustov – measured the density, prepared samples for compression testing, and participated in discussion of results.
M. I. Alymov – defined the research objectives and participated in discussion of results.

Вклад авторов

А. С. Устюхин – определение цели работы, проведение исследований структуры электронной микроскопией, участие в обсуждении результатов, написание текста статьи.
В. А. Зеленский – определение цели работы, подготовка смесей, прессование, спекание и закалка образцов, участие в обсуждении результатов и редактировании статьи.
И. М. Миляев – термическая обработка и измерение магнитных свойств образцов.
Д. Ю. Ковалев – рентгенофазовый анализ образцов и обсуждение результатов.
В. С. Шустов – измерение плотности, подготовка образцов для механических испытаний на сжатие, участие в обсуждении результатов.
М. И. Алымов – определение цели работы, участие в обсуждении результатов.

Received 28.02.2025
Revised 19.03.2025
Accepted 24.03.2025

Статья поступила 28.02.2025 г.
Доработана 19.03.2025 г.
Принята к публикации 24.03.2025 г.

Production Processes and Properties of Powders
Процессы получения и свойства порошков

UDC 621.762.34

https://doi.org/10.17073/1997-308X-2025-2-15-23

Research article
Научная статья

Optimization of powder mixing parameters for the Al–Sn–Pb system for use in selective laser melting

K. O. Akimov[1], A. L. Skorentsev[1, 2], N. M. Rusin[1], V. E. Likharev[1, 2],
A. Yu. Nikonov[1, 3], A. I. Dmitriev[1, 3] ✉

[1] **Institute of Strength Physics and Materials Science**
of the Siberian Branch of the Russian Academy of Sciences
2/4 Akademichesky Prosp., Tomsk 634055, Russia
[2] **National Research Tomsk Polytechnic University**
30 Lenina Prosp., Tomsk 634050, Russia
[3] **National Research Tomsk State University**
36 Lenina Prosp., Tomsk 634050, Russia

✉ dmitr@ispms.ru

Abstract. This study presents the results of research on optimizing powder mixing parameters for the Al–15Sn–5Pb (vol. %) system for application in selective laser melting technology. The primary focus is on ensuring the uniform distribution of soft-phase particles (Sn and Pb), which is essential for obtaining products with a homogeneous structure and improved tribological properties. The initial materials used in the study were aluminum (ASD-1), tin (PO-1), and lead (PS-1) powders. Before mixing, the powders were sieved using mesh sizes ranging from 50 to 25 μm. The sieved powders had a nearly spherical shape and good flowability characteristics (less than 25 s / 50 g). The effect of mixing time on the homogeneity of the powder mixture was studied using the discrete element method and a modified Hertz–Mindlin model. The obtained mixtures were analyzed using *X*-ray phase analysis, micro-*X*-ray spectral analysis, and graphical analysis methods. Subsequent experimental validation confirmed the reliability of numerical calculations and enabled the assessment of optimal mixing parameters. It was established that the optimal mixing time for achieving a uniform distribution of the initial powder particles falls within the range of 60 to 120 min. It was also found that the complex motion pattern of a *Turbula*-type mixer reduces the impact of gravitational segregation, thereby improving the uniform distribution of soft-phase particles (Sn + Pb). The proposed approach can be used for developing new powder preparation methods for additive manufacturing technologies and for creating composite materials with enhanced performance characteristics.

Keywords: selective laser melting (SLM), aluminum alloys, antifriction alloys, discrete elements method, mixing

Acknowledgements: This study was supported by the Russian Science Foundation [Grant No. 24-79-10099], https://ias.rscf.ru/user/doc/a.w.p.2024.98.legacy/182272.

For citation: Akimov K.O., Skorentsev A.L., Rusin N.M., Likharev V.E., Nikonov A.Yu., Dmitriev A.I. Optimization of powder mixing parameters for the Al–Sn–Pb system for use in selective laser melting. *Powder Metallurgy and Functional Coatings*. 2025;19(2):15–23. https://doi.org/10.17073/1997-308X-2025-2-15-23

Оптимизация параметров смешивания порошков системы Al–Sn–Pb для использования при селективном лазерном сплавлении

К. О. Акимов[1], **А. Л. Скоренцев**[1, 2], **Н. М. Русин**[1], **В. Е. Лихарев**[1, 2],
А. Ю. Никонов[1, 3], **А. И. Дмитриев**[1, 3]

[1] **Институт физики прочности и материаловедения Сибирского отделения Российской академии наук**
Россия, 634055, г. Томск, пр-т Академический, 2/4
[2] **Национальный исследовательский Томский политехнический университет**
Россия, 634050, г. Томск, пр-т Ленина, 30
[3] **Национальный исследовательский Томский государственный университет**
Россия, 634050, г. Томск, пр-т Ленина, 36

dmitr@ispms.ru

Аннотация. В работе представлены результаты исследования по оптимизации параметров смешивания порошков системы Al–15Sn–5Pb (об. %) для применения их в технологии селективного лазерного сплавления. Основное внимание уделено обеспечению равномерного распределения частиц мягкой фазы (Sn и Pb), необходимого для получения изделий с однородной структурой и улучшенными триботехническими свойствами. В качестве исходных материалов использовались порошки алюминия (АСД-1), олова (ПО-1) и свинца (ПС-1). Перед смешиванием проводился их просев через сита с размерами ячеек от 50 до 25 мкм. Просеянные порошки имели форму, близкую к сферической, и хорошие характеристики текучести (менее 25 с / 50 г). С использованием метода дискретных элементов и модифицированной модели Герца–Миндлина изучено влияние времени смешивания на степень гомогенности порошковой смеси. Исследования полученных смесей проводились с помощью рентгенофазового, микрорентгеноспектрального и графического методов анализа. Последующая экспериментальная валидация подтвердила достоверность результатов численных расчетов и позволила оценить оптимальные параметры смешения. Установлено, что оптимальное время смешивания, позволяющее получить равномерное распределение исходных порошковых частиц, находится в интервале от 60 до 120 мин. Обнаружено, что сложный характер движения смесителя типа «Турбула» снижает влияние гравитационной сегрегации, улучшая равномерность распределения частиц мягкой фазы (Sn + Pb). Предложенный подход может быть использован для разработки новых методик подготовки порошков для аддитивных технологий и создания композиционных материалов с улучшенными эксплуатационными характеристиками.

Ключевые слова: селективное лазерное сплавление (СЛС), алюминиевые сплавы, антифрикционные сплавы, метод дискретных элементов, перемешивание

Благодарности: Работа выполнена при финансовой поддержке Российского научного фонда [грант № 24-79-10099], https://ias.rscf.ru/user/doc/a.w.p.2024.98.legacy/182272.

Для цитирования: Акимов К.О., Скоренцев А.Л., Русин Н.М., Лихарев В.Е., Никонов А.Ю., Дмитриев А.И. Оптимизация параметров смешивания порошков системы Al–Sn–Pb для использования при селективном лазерном сплавлении. *Известия вузов. Порошковая металлургия и функциональные покрытия*. 2025;19(2):15–23.
https://doi.org/10.17073/1997-308X-2025-2-15-23

Introduction

The growing demand for high-performance antifriction materials in advanced engineering applications is driving the development of new metallic powder compositions designed to produce components with enhanced tribological properties [1–3]. This trend, combined with the rapid adoption of additive manufacturing technologies, imposes stricter requirements on the preparation of multicomponent powder mixtures. The extreme nonequilibrium conditions of the selective laser melting (SLM) process, characterized by intense heating ($>10^6$ K/s) and cooling rates (10^3–10^8 K/s), necessitate a high degree of homogeneity in the initial powder mixture, as any inhomogeneities can lead to structural defects and anisotropy, ultimately degrading the properties of the final components [4; 5].

Aluminum alloys are among the most widely used materials across various industries due to their unique combination of strength and low density, enabling the production of lightweight yet durable machine components. The integration of aluminum alloys into 3D printing technologies further enhances their appeal by providing additional design flexibility in terms of shape and structure [6]. The Al–15Sn–5Pb (vol. %) system is a specialized alloy intended for antifriction applications, such as sliding bearings, where tin and lead act as solid lubricants, reducing wear during frictional contact [7–9]. However, the tendency of these inclusions to segregate during both powder mixing and solidification in the 3D printing process necessitates stringent control over the composition of the powder mixture to ensure their uniform distribution in the final product [10]. Additionally, the relatively low evaporation temperature of lead (1749 °C) compared to the typical process temperatures of aluminum alloy SLM (>2000 °C) requires precise energy input control to prevent selective evaporation [11].

Mixing powders with significant density differences poses a fundamental challenge [12]. In the Al–15Sn–5Pb system, where the density ratio of lead to aluminum is approximately 4.2:1.0, this issue becomes particularly pronounced. Traditional drum mixers, which operate mainly by gravitational forces, tend to promote segregation rather than effective mixing in such systems, as denser lead and tin particles naturally migrate downward. This results in localized inhomogeneities in the powder mixture, which is critical for its subsequent use in SLM [13]. One potential solution to this problem is the use of a *Turbula*-type mixer manufactured by Vibrotechnik (Russia), which combines rotational and translational motion in a rhythmic three-dimensional pattern. This complex motion induces intense mixing conditions that counteract gravitational effects, thereby reducing segregation driven by density differences. The powder layer periodically experiences near-weightlessness, followed by abrupt directional changes, which help prevent agglomeration.

The objective of this study was to evaluate the effectiveness of the modified Hertz–Mindlin model in predicting the quality of the resulting powder mixture composed of components with significant density variations, as well as to determine the optimal mixing parameters for the Al–15Sn–5Pb system using a *Turbula*-type mixer. The research focused on identifying the minimum mixing time required to achieve compositional homogeneity sufficient for the successful application of powder mixtures with large density differences in the SLM process.

Materials and methods

The experiments were conducted using aluminum (ASD-1), tin (PO-1), and lead (PS-1) powders. The powders were sieved through meshes with an upper cell size limit of 50 μm and a lower limit of 25 μm.

Analysis of several scanning electron microscopy (SEM) images revealed that the average particle size of all studied powders was 30 μm (Fig. 1), with a size distribution approximating a normal distribution. The aluminum powder particles had a spherical shape, whereas the tin and lead powders exhibited both spherical and dumbbell-like morphologies.

Additionally, powder flowability was analyzed using funnels with outlet diameters of 2.5 mm (tin, lead) and 5 mm (aluminum) according to GOST 20899–98 (ISO 4490–78). Measurements of the natural repose angle showed that its value for all three powders was approximately 30°. The flowability of the tin and lead powders did not exceed 20 s/50 g, while that of aluminum was 26 s/50 g, indicating their suitability for SLM technology.

Mixing simulations were performed using the discrete element method (DEM) with the Altair EDEM software package (Altair Engineering, USA). The par-

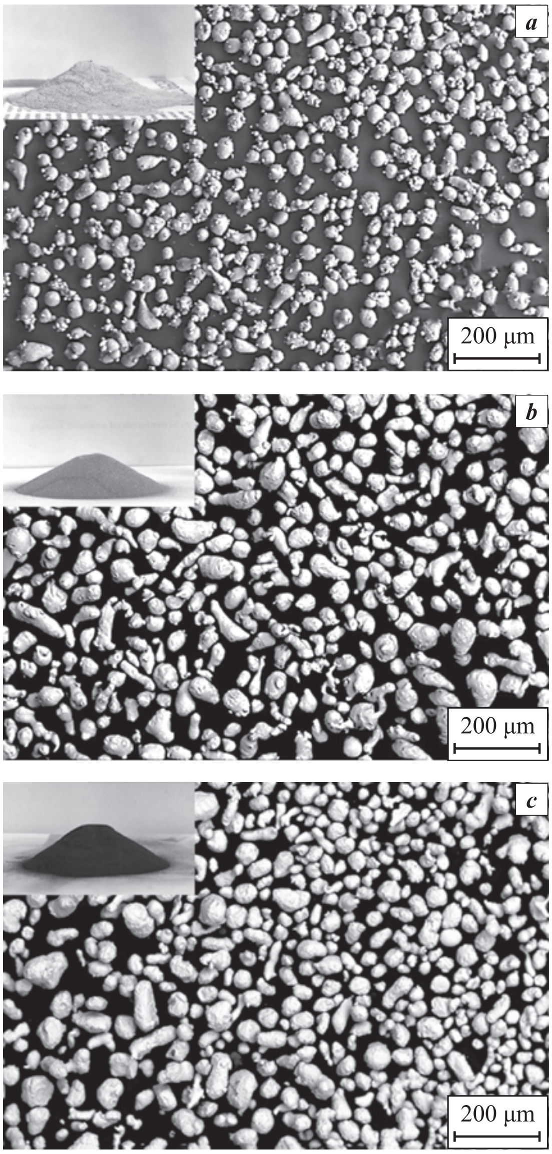

Fig. 1. SEM images of Al (***a***), Sn (***b***), and Pb (***c***) powders before mixing in a *Turbula* mixer

Рис. 1. РЭМ-изображения порошков Al (***a***), Sn (***b***) и Pb (***c***) перед смешиванием в смесителе типа «Турбула» ticle-to-particle and particle-to-wall interactions were described by the Hertz–Mindlin model, modified according to the Johnson–Kendall–Roberts (JKR) theory [14; 15]. This contact interaction model is widely used in powder mixing simulations to account for adhesion forces [16–21]. To accelerate computational time, model scaling was applied, reducing the container size and powder mass by a factor of three.

The physical parameters of the powders used in the model are presented in Tables 1 and 2. The friction and restitution coefficients were averaged based on data from various sources [22–26]. For Sn and Pb friction pairs, the friction coefficients were taken from similar bearing steels with comparable properties.

To analyze the variation in the tin and lead powder content during mixing, the container volume was conditionally divided into 28 cells, where the fraction of each metal's particles was assessed using the formula N_{ij}/V_{ij}, where N_{ij} is the number of Sn and Pb particles, V_{ij} is the cell volume, and i and j are the cell indices along the X and Y axes, respectively (Fig. 2).

In a *Turbula*-type mixer, the powder mixture was blended at a container rotation speed of 30 rpm. The mixing duration varied within the range of $\tau = 10 \div 240$ min. From the obtained mixtures, 10 compacts were produced by pressing, with the powder for each compact being taken from different parts of the container.

An initial analysis of the composition of the initial components in the powder mixture was performed using X-ray phase analysis with a DRON-8 diffractometer (NPP Burevestnik, Russia) in CuK_α radiation ($\lambda = 1.5406$ Å) over a 2θ range of 10–110°.

For metallographic studies, cross-sections of the compacts along their diameters were examined.

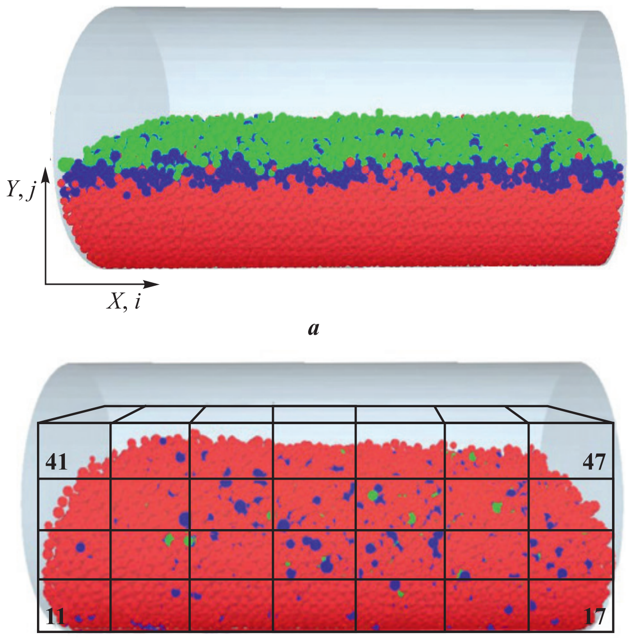

a

b

Fig. 2. Container model with powders at the beginning (***a***) and after 3 h of mixing (***b***)
The first digit in Figure ***b*** corresponds to the *i* index, and the second to *j* index
Al is highlighted in red, Sn in blue, and Pb in green

Рис. 2. Модель контейнера с порошками в начале (***a***) и после 3 ч перемешивания (***b***)
Первая цифра на рисунке ***b*** соответствует индексу *i*, вторая – *j*
Al выделен красным цветом, Sn – синим, Pb – зеленым

The microstructural analysis of the obtained compacts, as well as the elemental composition assessment, was conducted using a LEO EVO 50 scanning electron microscope (Carl Zeiss, Germany) equipped with an energy-dispersive X-ray spectroscopy (EDS)

Table 1. **Physical parameters of powders used in the simulation**

Таблица 1. **Физические параметры порошков, заложенные в моделирование**

Powder	Particle diameter, m	Particle density, kg/m^3	Poisson's ratio	Shear modulus, Pa·10^9	Particle mass, kg	Number of particles, pcs
Al	0.001 ± 0.0003	2700	0.33	26.30	0.283	22,391
Sn	0.001 ± 0.0003	7300	0.44	12.15	0.074	4,203
Pb	0.001 ± 0.0003	11 300	0.43	4.90	0.143	1,418

Table 2. **Friction and restitution coefficients of the simulated powders**

Таблица 2. **Коэффициенты трения и реституции моделируемых порошков**

Parameter	Friction pair								
	Al–Al	Sn–Sn	Pb–Pb	Al–Sn	Al–Pb	Sn–Pb	Al–steel	Sn–steel	Pb–steel
Static friction coefficient	1.1	0.74	0.9	0.5	0.5	1.4	0.50	0.40	0.30
Rolling friction coefficient	0.3	0.20	0.2	0.2	0.2	0.5	0.05	0.05	0.05
Restitution coefficient	0.6	0.50	0.4	0.5	0.5	0.5	0.60	0.60	0.60

module. The graphical analysis of SEM images of the compact cross-sections was performed using ImageJ software (National Institutes of Health, USA).

Results and discussion

Simulation

The simulation results for the number of tin and lead particles in different areas of the container over 3 h of mixing, approximated by logarithmic dependencies, are presented in Fig. 3. It was found that at a mixing duration (τ) of up to 30 min, the majority of both lead and tin particles remain predominantly in the upper layers of the powder mixture, despite the complex motion pattern of the container during the process. This may be attributed to the formation of temporary agglomerates of Sn and Pb particles, as these powders exhibit a high tendency toward adhesion due to their lower hardness and high plasticity compared to aluminum, leading to the formation of more stable contacts. As τ increases to 60 min, the dependencies of Sn and Pb particle content in different cells converge within the 4–6 % range and nearly equalize at 180 min.

Based on these results, it can be assumed that to obtain a near-homogeneous Al–15Sn–5Pb mixture, the minimum mixing time in the *Turbula* mixer should be 60 min at a container rotation speed of 30 rpm.

Experiment

A typical diffractogram of a compact made from the Al–15Sn–5Pb mixture and the dependence of the soft-phase (Sn + Pb) content on the mixing time, calculated using the corundum number method, are presented in Fig. 4. It can be observed that at short mixing times, the soft-phase content is lower (15 vol. %), with significant variations (6 %) in its values (Fig. 4, *b*). These data partially confirm the simulation results, indicating the presence of soft-phase particle agglomerates. The expected tin and lead content levels in the mixture are reached after 60 min of mixing, confirming the reliability of the applied numerical model. In the 120–180 min time range, the dependence acquires a linear character, and the variation in soft-phase element content does not exceed 2 %.

The results of SEM studies, presented in Fig. 5, indicate that at short mixing times (τ = 10–60 min), an uneven distribution of soft-phase particles is observed, with large agglomerates of various shapes reaching 300 μm in size. The use of such powder mixtures in SLM would likely result in large defects due to local inhomogeneities in the initial powder distribution. At τ = 120–240 min, tin and lead become more evenly distributed across the polished section surface, and the size of soft-phase agglomerates decreases. Completely eliminating these agglomerates is not feasible due to the inherent tendency of these powders to adhere. However, at this stage, the powder mixtures can be considered suitable for SLM technology.

The EDS analysis results of the compact element composition are presented in Table 3. According to the data, even at short mixing times, the mixture contains Sn and Pb levels close to the target composition. However, due to inhomogeneous distribution within the powder volume, a significant deviation from the mean is observed in different sections of the com-

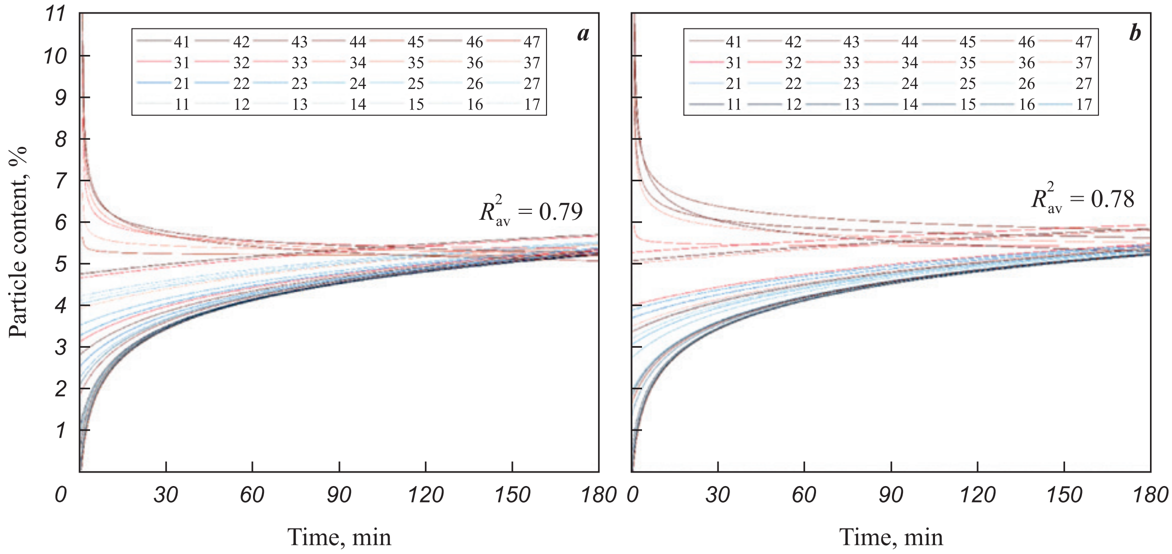

Fig. 3. Dependences of the content of Sn (***a***) and Pb (***b***) particles in the cells (11÷47) of the container on the mixing time

Рис. 3. Зависимости содержания частиц Sn (***a***) и Pb (***b***) в ячейках (11–47) контейнера от времени перемешивания

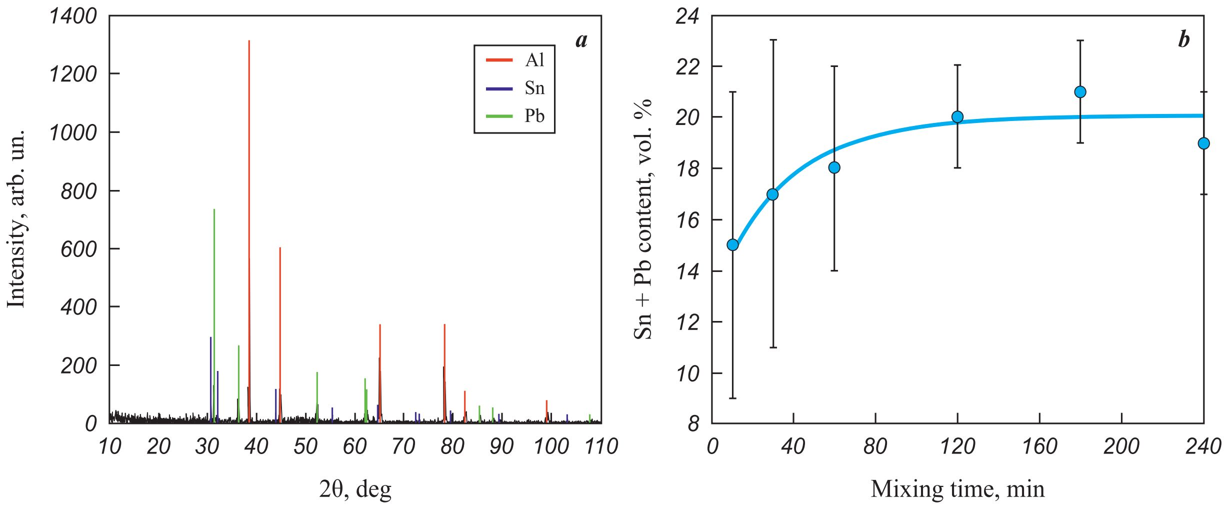

Fig. 4. Typical diffractogram of the Al–15Sn–5Pb mixture (***a***)
and dependence of the soft-phase (Sn + Pb) content on the mixing time (***b***)

Рис. 4. Типичная дифрактограмма смеси состава Al–15Sn–5Pb (***a***)
и зависимость содержания мягкой фазы Sn + Pb от времени перемешивания (***b***)

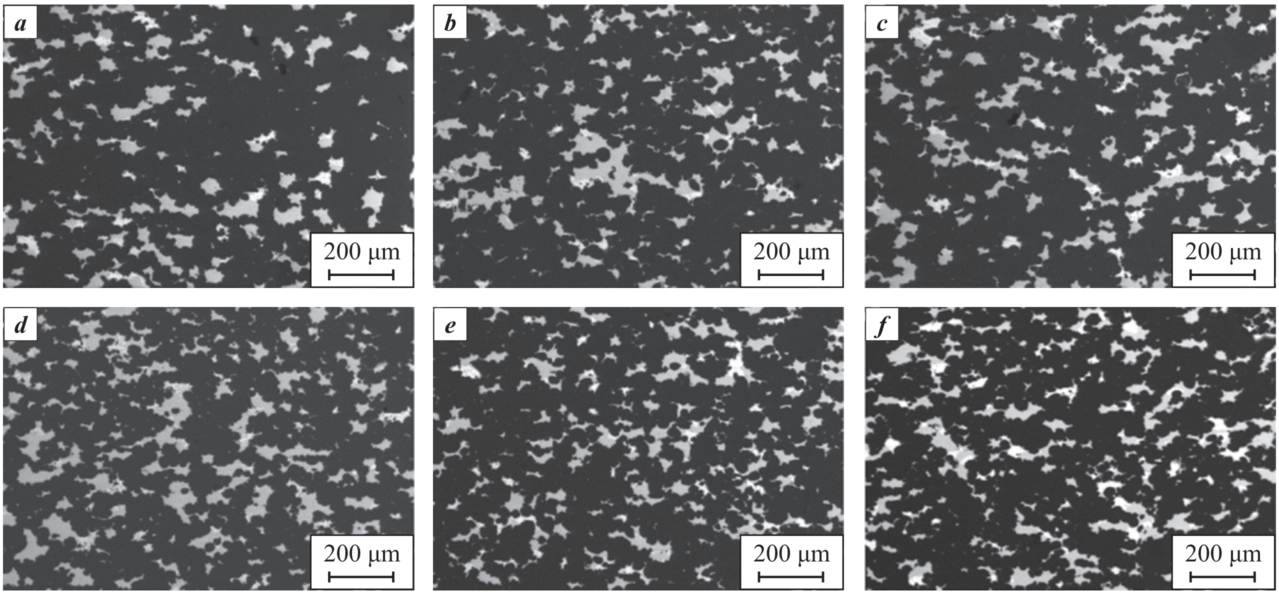

Fig. 5. Typical SEM images of cross-sections of powder compacts
obtained from mixtures after 10 (***a***), 30 (***b***), 60 (***c***), 120 (***d***), 180 (***e***), and 240 min (***f***) of mixing

Dark phase – Al, bright phases – Sn and Pb

Рис. 5. Типичные РЭМ-снимки поперечных сечений исследуемых компактов из порошковых смесей,
полученных после перемешивания в течение 10 (***a***), 30 (***b***), 60 (***c***), 120 (***d***), 180 (***e***) и 240 мин (***f***)

Темная фаза – Al, светлые – Sn и Pb

pacts. After 60 min of mixing, these deviations are reduced by approximately a factor of two, indicating the breakdown of large agglomerates. Mixing for 120 min or longer further decreases the deviation from the average element content within different compact sections to ≈ 2 %, suggesting that the elements have reached a sufficiently homogeneous distribution throughout the volume.

In addition to EDS analysis, graphical analysis of SEM images was conducted using ImageJ software to assess the quantity and size of soft-phase (Sn + Pb) agglomerates (Fig. 6). The fraction of lead and tin was determined based on the area occupied by these particles. For each τ value, 10 images per compact were analyzed.

The analysis revealed that the tin and lead content follows an approximately linear trend. However,

Table 3. **Elemental content in powder compacts depending on mixing time**

Таблица 3. **Содержание элементов в компактах из порошковых смесей в зависимости от времени перемешивания**

τ, min	Content, vol. %		
	Al	Sn	Pb
10	81 ± 8	15 ± 8	4 ± 3
30	80 ± 5	15 ± 6	5 ± 3
60	80 ± 4	15 ± 4	5 ± 2
120	80 ± 2	16 ± 2	4 ± 1
180	80 ± 2	16 ± 2	4 ± 1
240	80 ± 2	16 ± 2	4 ± 1

at short mixing times, as observed in the EDS results, there is a high relative deviation in particle distribution within the volume (±6 %), which decreases to 1 % as τ increases. Despite the relative deviation reduction occurring as early as τ = 60 min, it is also important to consider the size of Sn and Pb agglomerates. The trend in agglomerate area reduction follows a linear downward pattern. With an increase in mixing duration, the agglomerate area decreases by approximately 35 %, from 1400 to 900 μm^2 at τ = 10 and 240 min, respectively. At the same time, the deviation value also decreases from 16 to 10 %, but remains relatively high. This is likely due to the formation of agglomerates within the internal volume of the powder mixture, which, lacking direct contact with the container walls, were more resistant to breakdown during mixing.

These findings indicate not only an improvement in mixture homogeneity within a relatively short period (τ = 60–120 min) but also the effectiveness of the modified Hertz–Mindlin model for simulating the mixing process in powder systems with significant density differences between their components.

Conclusions

Based on the obtained results, the following conclusions can be drawn.

1. The complex motion pattern of the *Turbula* mixer ensures effective mixing of the Al–15Sn–5Pb powder system, reducing the impact of gravitational segregation and improving the uniformity of soft-phase (Sn + Pb) particle distribution. This allows for its further application in selective laser melting (SLM) technology.

2. The discrete element method with the modified Hertz–Mindlin model demonstrated high reliability in predicting the homogeneity evolution of powder mixtures, which was confirmed by experimental data.

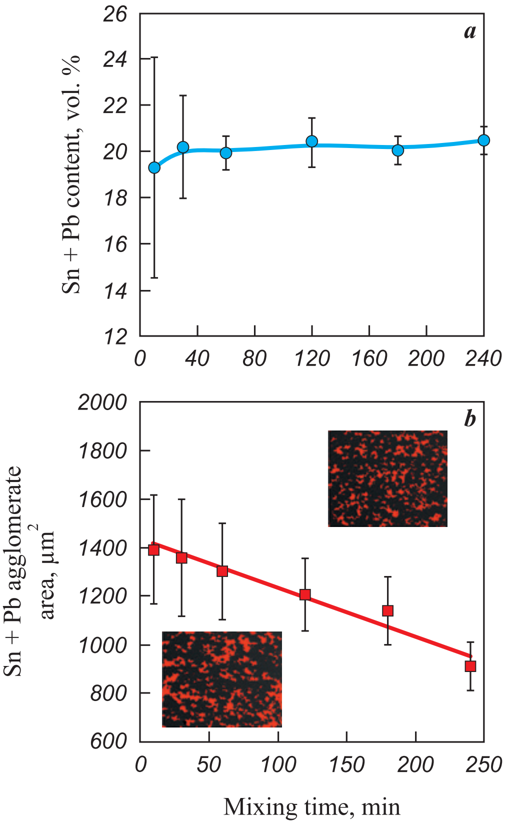

Fig. 6. Dependences of the content (***a***) and agglomerate size (***b***) of the soft phase (Sn + Pb) on the mixing time in the *Turbula* mixer

Рис. 6. Зависимости содержания (***а***) и размеров агломератов (***b***) мягкой фазы (Sn + Pb) от времени перемешивания в смесителе «Турбула»

3. It was established that reducing the size of soft-phase (Sn + Pb) agglomerates and minimizing component distribution deviations occur at a mixing time of 60 to 120 min, making this interval recommended for practical applications.

4. The obtained results can be utilized to improve powder preparation quality for additive manufacturing technologies and to develop new powder materials with enhanced performance characteristics.

References / Список литературы

1. Ralls A., Merbin J., Noud J., Lopez J., LeSourd Kasey, Napier I., Hallas N., Menezes P. Tribological, corrosion, and mechanical properties of selective laser melted steel. *Metals*. 2022;12(10):1732. https://doi.org/10.3390/met12101732
2. Yang G., Zhang J., Xie H., Li F., Huang Z., Yuan G., Zhang J., Jia Q., Zhang H., Yeprem H.A., Zhang S. Preparation of B_4C_p/Al composites via selective laser melting and their tribological properties. *Materials*. 2022;15:8340. https://doi.org/10.3390/ma15238340
3. Rusin N.M., Akimov K.O., Skorentsev A.L., Dmitriev A.I. Influence of laser power during laser powder bed fusion on the structure and properties of Al–40Sn alloy prepared

from a mixture of elemental powders. *Journal of Alloys and Compounds*. 2025;1013:178647.
https://doi.org/10.1016/j.jallcom.2025.178648

4. Mukherjee T., DebRoy T. A digital twin for rapid qualification of 3D printed metallic components. *Applied Materials Today*. 2019;14:59–65.
https://doi.org/10.1016/j.apmt.2018.11.003
5. Han Tianyi, Chen Jiaying, Wei Zongfan, Qu Nan, Liu Y., Yand D., Zhao S., Lai Z., Jiang M., Zhu J. Effect of cooling rate on microstructure and mechanical properties of $AlCrFe_2Ni_2$ medium entropy alloy fabricated by laser powder bed fusion. *Journal of Materials Research and Technology*. 2023;25:4063–4073.
https://doi.org/10.1016/j.jmrt.2023.06.241
6. Wang Z., Ummethala R., Singh N., Tang S., Suryanarayana C., Eckert J., Prashanth K.G. Selective laser melting of aluminum and its alloys. *Materials*. 2020;13:4564.
https://doi.org/10.3390/ma13204564
7. Rusin N.M., Skorentsev A.L., Akimov K.O. Mechanical properties of sintered Al–Sn–Fe alloys. *Physical Mesomechanics*. 2024;27(1):69–78.
https://doi.org/10.1134/S1029959924010077
8. Confalonieri C., Gariboldi E. Al–Sn miscibility gap alloy produced by power bed laser melting for application as phase change material. *Journal of Alloys and Compounds*. 2021;881:160569.
https://doi.org/10.1016/j.jallcom.2021.160596
9. Rusin N.M., Skorentsev A.L., Akimov K.O. Al–40Sn alloy produced by selective laser melting of elemental powder mixtures. *Physics of Metals and Metallography*. 2023;124(9):908–915.
https://doi.org/10.1134/S0031918X23601476
10. Guo Z., Jie J., Liu S., Yue S., Zhang Y., Li T. Solidification characteristics and segregation behavior of Cu–15Ni–8Sn alloy. *Metallurgical and Materials Transactions A*. 2020;51:1229–1241.
https://doi.org/10.1007/s11661-019-05609-y
11. Shi G., Zhang R., Cao Y., Yang G. A review of the vaporization behavior of some metal elements in the LPBF process. *Micromachines*. 2024;15:846.
https://doi.org/10.3390/mi15070846
12. Hogg R. Mixing and segregation in powders: Evaluation, mechanisms and processes. *KONA Powder and Particle Journal*. 2009;27:3–17.
https://doi.org/10.14356/kona.2009005
13. Vock S., Klöden B., Kirchner A., Weißgärber T., Kieback B. Powders for powder bed fusion: A review. *Progress in Additive Manufacturing*. 2019;4:383–397.
https://doi.org/10.1007/s40964-019-00078-6
14. Hertz H. On the contact of elastic solids. *Journal für die Reine und Angewandte Mathematik*. 1882;92:156–171.
15. Johnson K.L., Kendall K., Roberts A. Surface energy and the contact of elastic solids. *Proceedings of the Royal Society A*. 1971;324:301–313.
16. Li J., Peng F., Li H., Ru Z., Fu J., Zhu W. Material evaluation and dynamic powder deposition modeling of PEEK/CF composite for laser powder bed fusion process. *Polymers*. 2023;15:2863.
https://doi.org/10.3390/polym15132863
17. Yan W., Qian Y., Ge W., Lin S., Liu W.K., Lin F., Wagner G.J. Meso-scale modeling of multiple-layer fabrication process in selective electron beam melting. *Materials and Design*. 2018;14:210–219.
https://doi.org/10.1016/j.matdes.2017.12.031
18. Yeom S.B., Ha E.-S., Kim M.-S., Jeong S.H., Hwang S.-J., Choi D.H. Application of the discrete element method for manufacturing process simulation in the pharmaceutical industry. *Pharmaceutics*. 2019;11:414.
https://doi.org/10.3390/pharmaceutics11080414
19. Horabik J., Molenda M. Parameters and contact models for DEM simulations of agricultural granular materials: A review. *Biosystems Engineering*. 2016;147:206–225.
https://doi.org/10.1016/j.biosystemseng.2016.02.017
20. Pantaleev S., Yordanova S., Janda A., Marigo M., Jin Y.O. An experimentally validated DEM study of powder mixing in a paddle blade mixer. *Powder Technology*. 2017;311:287–302.
https://doi.org/10.1016/j.powtec.2016.12.053
21. Marigo M., Cairns D.L., Davies M., Ingram A., Stitt E.H. Developing mechanistic understanding of granular behaviour in complex moving geometry using the discrete element method. Part B. Investigation of flow and mixing in the Turbula® mixer. *Powder Technology*. 2011;212(1):1724.
https://doi.org/10.1016/j.powtec.2011.04.009
22. Totten G.E. ASM Handbook. Vol. 18. Friction, lubrication, and wear technology. Ohio: ASM International, 2017. 1091 p.
23. Bajpai A., Saxena P., Kunze K. Tribo-mechanical characterization of carbon fiber-reinforced cyanate ester resins modified with fillers. *Polymers*. 2020;12:1725.
https://doi.org/10.3390/polym12081725
24. Bowden F.P., Tabor D. The friction and lubrication of solids. Oxford: University Press, 2001. 424 p.
25. Anurev V.I. Handbook of the mechanical engineer-designer. Vol. 1. Moscow: Mashinostroenie, 2001. 920 p. (In Russ.).

    Анурьев В.И. Справочник конструктора-машиностроителя. Т. 1. М.: Машиностроение, 2001. 920 с.
26. Blanter M.S., Golovin I. S., Neuhäuser H., Sinning H.-R. Internal friction in metallic materials: A Handbook. Berlin: Springer, 2007. 520 p.

Information about the Authors

Kirill O. Akimov – Cand. Sci. (Eng.), Research Associate of the Laboratory of Powder Materials Consolidation Physics, Institute of Strength Physics and Materials Science of the Siberian Branch of Russian Academy of Sciences (ISPMS SB RAS)
ORCID: 0000-0002-3204-250X
E-mail: akimov_ko@ispms.ru

Сведения об авторах

Кирилл Олегович Акимов – к.т.н., науч. сотрудник лаборатории физики консолидации порошковых материалов, Институт физики прочности и материаловедения Сибирского отделения Российской академии наук (ИФПМ СО РАН)
ORCID: 0000-0002-3204-250X
E-mail: akimov_ko@ispms.ru

Alexander L. Skorentsev – Cand. Sci. (Eng.), Research Associate of the Laboratory of Powder Materials Consolidation Physics, ISPMS SB RAS; Engineer of the Department of Experimental Physics, School of Nuclear Engineering, National Research Tomsk Polytechnic University (TPU)
ORCID: 0000-0003-2506-9437
E-mail: skoralexan@ispms.ru

Nikolay M. Rusin – Cand. Sci. (Eng.), Senior Research Scientist of the Laboratory of Powder Materials Consolidation Physics, ISPMS SB RAS
ORCID: 0000-0002-7537-7895
E-mail: rusinnm@ispms.ru

Vadim E. Likharev – Engineer of the Laboratory of Powder Materials Consolidation Physics, ISPMS SB RAS; Student of the engineering school of new production materials, TPU
ORCID: 0009-0002-4713-3663
E-mail: vel6@tpu.ru

Anton Yu. Nikonov – Cand. Sci. (Phys.Math.), Research Associate of the Laboratory of Computer-Aided Design of Materials, ISPMS SB RAS; Associate Professor of the Department of Physics of Metals, Faculty of Physics, National Research Tomsk State University (TSU)
ORCID: 0000-0002-0980-0317
E-mail: anickonoff@ispms.ru

Andrey I. Dmitriev – Dr. Sci. (Phys.Math.), Principal Researcher of the Laboratory of Powder Materials Consolidation Physics, ISPMS SB RAS; Professor of the Department of Physics of Metals, Faculty of Physics, TSU
ORCID: 0000-0002-2823-578X
E-mail: dmitr@ispms.ru

Александр Леонидович Скоренцев – к.т.н., науч. сотрудник лаборатории физики консолидации порошковых материалов, ИФПМ СО РАН; инженер отделения экспериментальной физики инженерной школы ядерных технологий, Национальный исследовательский Томский политехнический университет (ТПУ)
ORCID: 0000-0003-2506-9437
E-mail: skoralexan@ispms.ru

Николай Мартемьянович Русин – к.т.н., ст. науч. сотрудник лаборатории физики консолидации порошковых материалов, ИФПМ СО РАН
ORCID: 0000-0002-7537-7895
E-mail: rusinnm@ispms.ru

Вадим Евгеньевич Лихарев – инженер лаборатории физики консолидации порошковых материалов, ИФПМ СО РАН; студент инженерной школы новых производственных материалов, ТПУ
ORCID: 0009-0002-4713-3663
E-mail: vel6@tpu.ru

Антон Юрьевич Никонов – к.ф.-м.н., науч. сотрудник лаборатории компьютерного конструирования материалов, ИФПМ СО РАН; доцент кафедры физики металлов физического факультета, Национальный исследовательский Томский государственный университет (ТГУ)
ORCID: 0000-0002-0980-0317
E-mail: anickonoff@ispms.ru

Андрей Иванович Дмитриев – д.ф.-м.н., гл. науч. сотрудник лаборатории физики консолидации порошковых материалов, ИФПМ СО РАН; профессор кафедры физики металлов физического факультета, ТГУ
ORCID: 0000-0002-2823-578X
E-mail: dmitr@ispms.ru

Contribution of the Authors

K. O. Akimov – formulation of the research problem, analysis of results using SEM, modeling, manuscript preparation.
A. L. Skorentsev – preparation of samples for SEM, discussion of results.
N. M. Rusin – *X*-ray phase analysis, discussion of results.

V. E. Likharev – preparation of the powder mixtures.
A. Yu. Nikonov – formulation of the simulation problem, discussion of the results.
A. I. Dmitriev – overall supervision of the study, analysis of simulation results, discussion of results, manuscript editing.

Вклад авторов

К. О. Акимов – постановка задачи, анализ результатов с использованием РЭМ, моделирование, написание статьи.
А. Л. Скоренцев – подготовка образцов для РЭМ, обсуждение результатов.
Н. М. Русин – рентгенофазовый анализ, обсуждение результатов.
В. Е. Лихарев – подготовка порошковых смесей.
А. Ю. Никонов – постановка задачи моделирования, обсуждение результатов.
А. И. Дмитриев – общее руководство работой, анализ результатов моделирования, обсуждение результатов, редактирование рукописи.

Received 23.01.2025
Revised 12.03.2025
Accepted 13.03.2025

Статья поступила 23.01.2025 г.
Доработана 12.03.2025 г.
Принята к публикации 13.03.2025 г.

Refractory, Ceramic, and Composite Materials
Тугоплавкие, керамические и композиционные материалы

UDC 621.762

https://doi.org/10.17073/1997-308X-2025-2-24-38

Research article
Научная статья

Structural, mechanical, and tribological properties of TiC–C–Al hybrid composites fabricated by self-propagating high-temperature synthesis combined with spontaneous infiltration

E. R. Umerov[1], A. P. Amosov[1], E. I. Latukhin[1], A. D. Kachura[1],
I. A. Rastegaev[2], M. A. Afanasiev[2]

[1] **Samara State Technical University**
244 Molodogvardeyskaya Str., Samara 443100, Russia
[2] **Togliatti State University**
14 Belorusskaya Str., Tolyatti, Samara region 445020, Russia

egundor@yandex.ru

Abstract. The addition of graphite particles to aluminum improves its tribological properties due to the self-lubricating effect, while reinforcement of such aluminum matrix composites (Al–C) with the ceramic phase of titanium carbide (TiC), known for its high hardness and strength, results in Al–TiC–C hybrid composites with enhanced physical and mechanical properties and improved wear resistance. This study explores a novel energy-efficient approach to fabricating Al–TiC–C composites by combining self-propagating high-temperature synthesis (SHS) of porous TiC–C composite frameworks with subsequent spontaneous infiltration using molten aluminum. The titanium carbide was synthesized from a stoichiometric powder mixture of titanium and graphite (Ti + C). To introduce free carbon, additional graphite powders with particle sizes of 10–15 and 100–1000 μm, as well as chopped carbon fibers with a diameter of 7 μm and a length of 3 mm, were added to the stoichiometric mixture. The microstructure and composition of the resulting composites were examined using scanning electron microscopy with energy-dispersive spectroscopy and *X*-ray diffraction analysis. Density was measured by hydrostatic weighing, while Brinell hardness, compressive strength, and tribological properties were evaluated using a pin-on-disk tribometer. It was found that fine graphite particles (10–15 μm) dissolved almost completely in molten aluminum, whereas coarse graphite (100–1000 μm) and carbon fibers remained intact. The compressive strength of the carbon-containing aluminum matrix composites ranged from 203 to 233 MPa. Under dry sliding conditions, abrasive wear was the predominant wear mechanism, accompanied by a high coefficient of friction (0.88–0.98); however, the wear rate of the composite containing coarse graphite was three times lower.

Keywords: composite material, aluminum, titanium carbide, graphite, self-propagating high-temperature synthesis (SHS), porous framework, infiltration, tribology

Acknowledgements: The work was supported by the Russian Science Foundation (grant No. 24-79-10187), https://rscf.ru/project/24-79-10187/

For citation: Umerov E.R., Amosov A.P., Latukhin E.I., Kachura A.D., Rastegaev I.A., Afanasiev M.A. Structural, mechanical, and tribological properties of TiC–C–Al hybrid composites fabricated by self-propagating high-temperature synthesis combined with spontaneous infiltration. *Powder Metallurgy and Functional Coatings*. 2025;19(2):24–38.
https://doi.org/10.17073/1997-308X-2025-2-24-38

Структурные, механические и трибологические особенности гибридных композитов TiC–C–Al, изготовленных методом самораспространяющегося высокотемпературного синтеза в сочетании с самопроизвольной инфильтрацией

Э. Р. Умеров[1], **А. П. Амосов**[1] ✉, **Е. И. Латухин**[1], **А. Д. Качура**[1],
И. А. Растегаев[2], **М. А. Афанасьев**[2]

[1] **Самарский государственный технический университет**
Россия, 443100, г. Самара, ул. Молодогвардейская, 244
[2] **Тольяттинский государственный университет**
Россия, 445020, Самарская обл., г. Тольятти, ул. Белорусская, 14

✉ egundor@yandex.ru

Аннотация. Добавление частиц графита к алюминию позволяет улучшить его трибологические свойства за счет проявления эффекта самосмазывания, а армирование таких алюмоматричных композитов (Al–C) керамической фазой карбида титана (TiC) с высокими твердостью и прочностью – получить гибридные композиты Al–TiC–C с повышенными физико-механическими свойствами и улучшенной износостойкостью. В настоящей работе рассмотрено применение нового энергоэффективного подхода к получению композитов Al–TiC–C путем сочетания метода самораспространяющегося высокотемпературного синтеза (СВС) пористых композиционных каркасов из карбида титана и свободного углерода (TiC–C) с последующей инфильтрацией их расплавом алюминия. Для синтеза карбида титана использовалась стехиометрическая смесь порошков титана и графита Ti + C, а для получения свободного углерода в эту стехиометрическую смесь добавлялись порошки графита с размерами частиц 10–15 и 100–1000 мкм, а также рубленое углеволокно диаметром 7 мкм и длиной 3 мм. Для изучения микроструктуры и состава новых композитов использовались методы сканирующей электронной микроскопии с энергодисперсионной спектрометрией и рентгенофазового анализа. Также определены плотность гидростатическим взвешиванием, твердость по Бринеллю, прочность при сжатии и трибологические свойства на трибометре по схеме «*pin–on–disk*». Установлено, что добавляемый графит с мелкими частицами (10–15 мкм) практически полностью растворяется в расплаве алюминия, а крупнозернистый графит (100–1000 мкм) и углеволокно в нем сохраняются. Предел прочности при сжатии углеродсодержащих алюмоматричных композитов составил 203–233 МПа. Установлено, что при сухом трении реализуется преимущественно абразивный механизм изнашивания с высоким коэффциентом трения (0,88–0,98), но в 3 раза меньшим износом образца композита, полученного с добавлением крупнозернистого графита.

Ключевые слова: композиционный материал (КМ), алюминий, карбид титана, графит, самораспространяющийся высокотемпературный синтез (СВС), пористый каркас, инфильтрация, трибология

Благодарности: Исследование выполнено за счет гранта Российского научного фонда № 24-79-10187, https://rscf.ru/project/24-79-10187/

Для цитирования: Умеров Э.Р., Амосов А.П., Латухин Е.И., Качура А.Д., Растегаев И.А., Афанасьев М.А. Структурные, механические и трибологические особенности гибридных композитов TiC–C–Al, изготовленных методом самораспространяющегося высокотемпературного синтеза в сочетании с самопроизвольной инфильтрацией. *Известия вузов. Порошковая металлургия и функциональные покрытия*. 2025;19(2):24–38. https://doi.org/10.17073/1997-308X-2025-2-24-38

Introduction

Aluminum matrix composites (AMCs) reinforced with graphite and ceramic particles are considered promising materials for tribological applications [1–3]. Graphite, classified as a solid lubricant, imparts self-lubricating properties to the strengthened matrix, resulting in reduced friction coefficients and prevention of seizure, thus making aluminum-based materials suitable for tribotechnical applications. The aluminum – graphite composite was first successfully fabricated in 1969. Over the past 50 years, several successful tests have demonstrated the use of aluminum–graphite pistons, bearings, and connecting rods in both gasoline and diesel engines. For example, aluminum–graphite cylinder liners exhibited improved performance (without scuffing) against aluminum pistons in Alpha Romeo and Ferrari Formula 1 racing cars [4]. The main challenge in fabricating graphite-containing AMCs lies in the poor wettability of carbon-based materials by molten aluminum at temperatures below 1320 K, which hinders good interfacial adhesion and uniform distribution of graphite particles throughout the matrix. Another commonly used approach to strengthen aluminum alloys is reinforcement with carbon fibers (CFs) [5].

Powder metallurgy and casting technologies are the most widespread methods for producing metal matrix composites, as they can provide acceptable levels of density, porosity, mechanical and tribological properties under industrial conditions at a reasonable cost [6; 7]. Powder metallurgy methods are based on processing materials in the solid state and may include such operations as mixing, pressing, and sintering to achieve minimal porosity in the resulting composite. Among these methods, self-propagating high-temperature synthesis (SHS) stands out as a technique that enables the synthesis of various ceramic phases from elemental powders through an exothermic chemical reaction. The heat released during the SHS reaction results in a high temperature of the synthesized ceramic product [8]. In addition, the rapid reaction is accompanied by intensive gas evolution, which leads to the formation of an open porous capillary structure with pore sizes ranging from 0.1 μm to 1–2 mm, depending on the synthesis conditions and the composition of the initial powders [9; 10].

Liquid-phase methods include stir casting, infiltration under pressure, and spontaneous (pressureless) infiltration [11; 12]. For instance, a carbon – graphite – aluminum composite was produced by infiltrating a porous (14–16 %) carbon – graphite framework with molten AK12 alloy at temperatures up to 700 °C and pressures up to 5 MPa [13]. However, improving wettability and limiting interfacial reactions required multiple process steps, including pre-coating the carbon – graphite pore surfaces with nickel sulfate, vibrovacuum treatment before infiltration, and mechanical densification of the composite to reduce residual porosity after aluminum infiltration, which significantly complicated the process. In [14], it was shown that infiltration at 0.8 MPa, 1073 K, and a 60 s holding time in an argon atmosphere enables the fabrication of an aluminum – carbon fiber composite. However, a substantial amount of the undesirable Al_4C_3 phase formed as a result of their interaction.

The main drawback of aluminum matrix composites with graphite as a filler is their relatively low strength. To improve this property, an additional strengthening component is introduced – for example, a metal oxide or carbide with high hardness and strength. One of the most promising candidates is titanium carbide (TiC), which has a hardness of 20–25 GPa and is frequently considered as a reinforcement for aluminum and its alloys. AMCs reinforced with TiC particles exhibit superior mechanical strength, which is also attributed to the stronger interfacial bonding in the Al–TiC system compared to composites reinforced with SiC particles. The work of adhesion between TiC and aluminum increases from 1317 to 1608 mJ/m^2 as the reaction temperature rises from 800 to 1000 °C [15]. Aluminum matrix composites reinforced with TiC particles also demonstrate enhanced tribological performance, comparable to that of conventional aluminum-based tribological alloys such as AO20-1 and bronzes under dry sliding conditions at contact pressures up to 0.7 MPa. Furthermore, under dry sliding against 40Kh steel, the aluminum alloy AK12M2MgN with up to 10 % TiC[1] shows a reduced coefficient of friction, regardless of the applied pressure [16].

To achieve optimal tribological performance, the development of poly-reinforced (hybrid) composites has been proposed. These contain both a hard, high-strength carbide and self-lubricating graphite (Gr). Aluminum matrix composites such as A356–10 % SiC–4 % Gr and A356–5 % Al_2O_3–3 % Gr have been developed for use in cylinder liners of cast aluminum engine blocks. Under dry friction conditions, these composites formed graphite-based tribofilms that improved the wear resistance of aluminum and reduced the coefficient of friction [17]. Hybrid composites based on aluminum and its alloys – such as 2024–5 % SiC–x % Gr ($x = 0$, 5 and 10) [18] and 7075–Gr [19] – have also been fabricated via powder metallurgy and exhibited excellent tribological performance due to the self-lubricating effect. In [20], it was shown that the combined reinforcement of 7075 aluminum alloy with TiC particles (5–15 %) and graphite (3–5 %) significantly improved the material's tribological properties, reducing both wear and the coefficient of friction under dry sliding conditions.

The authors of [21] note that 5 % of TiC nanoparticles and up to 10 % of graphite not only reduced the wear rate and coefficient of friction of aluminum but also promoted the formation of a stable lubricating layer under long sliding distances and high sliding speeds. This layer consisted of a stable graphite – TiC composition on the contact surface. Typically, ceramic – metal composites with self-lubricating properties are fabricated by powder metallurgy, which involves prolonged high-temperature sintering in a protective atmosphere. This significantly complicates the production process and increases its cost.

A more economically feasible alternative may be spontaneous infiltration, a simple and low-cost method based on the capillary action of liquid metal into a porous body. This process does not require special equipment to create pressure or maintain a gas atmosphere. However, the key prerequisite for implementing this method is achieving good wettabi-

---

[1] Here and hereinafter, wt. % is implied unless otherwise specified.

lity of the porous solid by the molten metal, which is often unachievable in industrial settings due to the different natures of ceramics and metals. In this study, the authors propose a new energy-efficient and simple approach for producing ceramic–metal composite materials by combining the exothermic SHS method with the self-heating of the synthesized porous ceramic (SHS framework) to temperatures exceeding 2000 °C. At such temperatures, good wettability of the ceramic by metals such as aluminum, copper, and tin can be achieved, allowing spontaneous infiltration of these melts into SHS frameworks [22–24]. A characteristic feature of such materials synthesized in air is their multiphase composition. For example, SHS-derived ceramic frameworks based on MAX phases such as Ti_3SiC_2 and Ti_3AlC_2 contain not only the target phase but also a significant amount of TiC, along with minor amounts of TiO_2, TiN, and Al_2O_3, which are poorly wetted by molten aluminum. However, the observed spontaneous infiltration of the melt into these frameworks suggests that the predominant factor enabling wettability is the extremely high temperature of the ceramic immediately after SHS [25; 26].

In the present study, a new approach is proposed for fabricating composites from a non-wettable component – carbon (graphite and carbon fiber) – by introducing it into the initial SHS mixture. In this case, excess carbon that does not participate in the synthesis reaction remains in the SHS system as an inert additive, which undergoes substantial heating during the exothermic synthesis of the ceramic compound. Thus, the aim of this work was to investigate the feasibility of producing TiC–C–Al hybrid composites by introducing excess carbon (graphite and carbon fiber) into the Ti + C reactive mixture to synthesize a porous TiC–C SHS framework followed by spontaneous infiltration with molten aluminum.

Materials and methods

The following materials were used in this study:

– titanium powder grade TPP-7 (TU 1715-449-05785388, particle size ≤ 300 μm);

– colloidal graphite grade S-2 (GOST 17022-81, particle size ≤ 15 μm) and graphite grade GMZ (TU 48-20-16-81, particle size 100–1000 μm);

– chopped carbon fiber grade SYT45S (Zhongfu Shenying Carbon Fiber Co., LTD, length 3 mm, diameter 7 μm).

Dried TPP-7 titanium and S-2 graphite powders, taken in a stoichiometric ratio for TiC synthesis via the reaction $Ti + C \rightarrow TiC$, were pre-mixed in a ball mill at 105 rpm for 20 min. A 100 % excess of carbon – in the form of S-2 graphite, GMZ graphite, or chopped carbon fiber (CF) – was added at the final mixing stage to prevent particle size reduction of the graphite. The amount of the excess additive corresponded to the mass of S-2 graphite in the stoichiometric Ti + C mixture. The loose powder charges were loaded into cylindrical hollow crucibles (22 mm in diameter) made of single-layer paper and placed into a recess in the sand, into which molten aluminum was then poured after ignition of the charge. was applied to the powder charge to ignite it, i.e., to initiate the SHS process in combustion mode. The general experimental setup is shown in Fig. 1.

Four types of initial powder charge were prepared with the following compositions:

1 – Ti (TPP-7 titanium) + C (S-2 graphite);

2 – Ti (TPP-7 titanium) + C (S-2 graphite) + 100 % excess C (S-2 graphite);

3 – Ti (TPP-7 titanium) + C (S-2 graphite) + 100 % excess C (GMZ graphite);

4 – Ti (TPP-7 titanium) + C (S-2 graphite) + 100 % excess C (carbon fiber).

The total powder charge mass was 40 g without excess carbon and 48 g with excess carbonaceous additives. At the moment of ignition, molten aluminum – pre-melted in an electric furnace at 900 °C – was poured into the recess in the sand, onto the side surface of the ignited powder charge. During the SHS synthesis of titanium carbide, the high-temperature (up to 2800 °C) [10] combustion zone of the porous sample absorbed the molten aluminum. The combus-

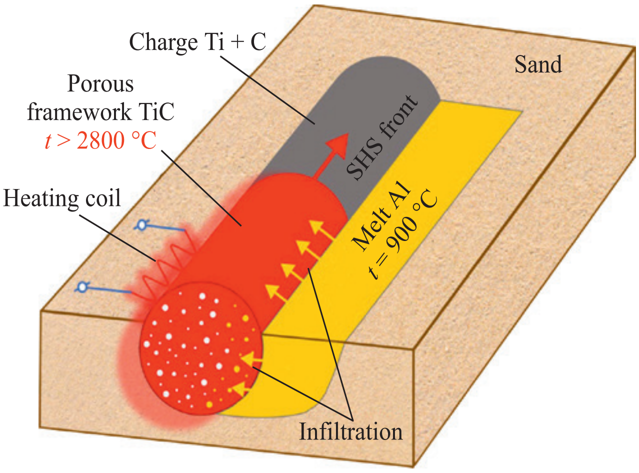

Fig. 1. Schematic representation of the SHS–infiltration process used to fabricate TiC–C–Al composites

Cross-sectional view

Рис. 1. Схема сочетания СВС и инфильтрации для получения композитов TiC–C–Al

Вид с разрезом

tion and infiltration process lasted approximately 20–25 s, after which the remaining aluminum melt was removed to facilitate subsequent mechanical processing and the fabrication of cylindrical composite samples for further testing.

Microstructure and elemental composition analyses were performed using a Tescan Vega 3 scanning electron microscope (SEM, Czech Republic) equipped with an X-act energy-dispersive spectroscopy (EDS) system. Phase composition of the synthesized products was identified by *X*-ray diffraction (XRD). XRD analysis was carried out using an automated ARL X'trA diffractometer (Thermo Scientific, Switzerland) with CuK_α radiation under continuous scanning in the 2θ range of 20–80° at a rate of 2°/min. The resulting diffraction patterns were processed using the WinXRD software package (Switzerland). Experimental density was determined by hydrostatic weighing in accordance with GOST 20018–74. Porosity was calculated as the difference between the theoretical and experimental density values of the composites. Brinell hardness was measured using a 5 mm steel ball under a load of 98 N, following GOST 9012–59. Uniaxial compression tests were conducted according to the guidelines of GOST 25.503–97 using cylindrical samples with a diameter of 20.1 ± 0.1 mm and a height of 19.4 ± 0.8 mm. The tests were performed on a WDW-300E universal testing machine (Time Group, China) at a crosshead speed of 1 mm/min. Sample dimensions before and after compression were measured using a 500-205 caliper (Mitutoyo, Japan) with a precision of 0.01 mm.

Based on the test results, stress–strain curves $\sigma^c = f(\varepsilon)$ were plotted, showing the dependence of compressive stress (σ^c) on relative strain (ε), taking into account the stiffness of the testing machine in accordance with GOST 25.503–97. The materials were then evaluated using the following parameters:

- elastic characteristics – from the slope angle of the linear portion of the curve ($\mathrm{tg}^c\alpha$) and the conventional compressive yield strength ($\sigma^c_{0.2}$);
- strength characteristics – from the compressive strength (σ_u^{c*}), where σ_u^{c*} was determined using a non-standard approach: its value was taken as the stress at the inflection point of the $\sigma^c = f(\varepsilon)$ curve observed after $\sigma^c_{0.2}$).

Tribological testing of the materials was carried out on a TRB50N tribometer (Nanovea, USA) using a rotary *pin-on-disk* configuration (ASTM G99), in which a vertically positioned cylindrical composite sample rotates about its longitudinal axis, and a friction counterbody (indenter) in the form of a stationary 6.35 mm diameter 100Cr6 steel ball is pressed against its upper face, 3 mm from the axis of rotation, under the following conditions:

– normal load on the indenter: $F = 2$ N;

– rotational speed of the sample: 200 rpm;

– wear track diameter: 6.0 mm, corresponding to a sliding speed of 62.8 mm/s;

– test duration: $\tau = 1$ h 19 min 54 s or a sliding distance of $L = 250$ m;

– lubrication regime: dry sliding.

Damage to the indenter was evaluated by measuring the wear scar diameter using the refined ASTM G99 formula. Damage to the composite sample was evaluated by 3D scanning the wear track on its end face and determining the lost metal volume (V) between the worn surface profile and a plane corresponding to the original undamaged surface. The wear scar diameter and wear volume of the sample were determined using a LEXT OLS4000 confocal laser scanning microscope (Olympus, Japan). Based on the volumetric wear data for both the samples and the indenters, the wear rate ($\dot{I}$) and wear resistance (W) were calculated using the formulas:

$$\dot{I} = \frac{V}{\tau},$$

$$W = \frac{1}{I} = \frac{L}{V},$$

where I or $\dot{I}$ is the wear rate in mm^3/m or mm^3/min, and L is the sliding distance in meters.

Throughout the tribological tests, the maximum ($\mu_{\max}$) and average (μ_{av}) values of the kinetic coefficient of friction were continuously measured in accordance with ASTM G40.

To assess changes related to the addition of excess carbon, two additional comparative parameters were used: the relative wear resistance (ε_I) and the friction coefficient stability (α), calculated as follows

$$\varepsilon_I = \frac{V_E}{V_C},$$

$$\alpha = \frac{\mu_{\mathrm{av}}}{\mu_{\max}},$$

where V_E and V_C are the average volumetric wear values of the reference material and the comparison material, respectively.

In this study, the baseline material was the Al–TiC composite fabricated without excess carbon. The ε_I parameter was calculated for both the test samples and the counterbody (indenter), since damage to the indenter is also a result of its interaction with the tested materials.

Results and discussion

Previous studies have shown that the least defective SHS-derived TiC frameworks were synthesized using relatively coarse titanium powder TPP-7 and graphite powder S-2 [13]. Therefore, these powder grades were chosen as the basis for studying the effect of excess carbon of various forms and particle sizes on the formation of TiC–C–Al hybrid composites. It is important to note that frameworks of all four types were successfully produced via SHS and infiltrated with molten aluminum.

As shown in Fig. 2, the composite samples after lathe machining exhibit a metallic luster and show virtually no large pores or cracks. Sample *B*, synthesized with an excess of fine S-2 graphite, is visually indistinguishable from sample *A* – the TiC–Al composite without excess carbon additives. In contrast, sample *C*, fabricated with the addition of coarse GMZ graphite (0.1–1.0 mm), shows uniformly distributed graphite particles of corresponding size throughout the entire volume. Sample *D*, synthesized with carbon fiber addition, contains dark inclusions formed by carbon fiber clusters embedded in the aluminum matrix.

The microstructure, phase composition, and porosity of the TiC–Al SHS composite have been described in detail in previous studies [27; 28]. In the sample without excess carbon, two main phases were identified: a metallic phase (Al) forming a continuous matrix that filled all accessible pore volume, and a ceramic phase (TiC) represented by tightly sintered equiaxed particles with a size of approximately 5–10 μm. The observed phase composition was as follows: 50–55 % Al, 40–45 % TiC, and up to 5 % secondary phases (Al_4C_3, $TiAl_3$, Al_2O_3). These minor phases were not detected by XRD due to their low content, but their presence was confirmed by SEM and EDS analysis. The Al_4C_3 phase appeared in the aluminum matrix as black acicular structures measuring up to 50–70 μm in length and 5–15 μm in width, while $TiAl_3$ was also found in the Al matrix, typically surrounding TiC particles. Since both secondary phases are products of high-temperature interaction between TiC and Al, they were observed primarily at or near the ceramic – metal interface of the composite. The residual porosity of such composites was up to 6–8 %, with an average density of 3.12 g/cm^3.

Fig. 3 shows the microstructure and the *X*-ray diffraction (XRD) pattern of the phase composition of the TiC–C(C-2)–Al composite, in which the excess carbon is introduced in the form of fine graphite particles approximately 15 μm in size. It can be seen that the ceramic and metallic components of the composite are tightly bonded. A few large pores are observed, while no systematic fine porosity is present, indicating good wettability. The ceramic region of the composite exhibits a gradient structure: the outer crust consists of densely sintered relatively large (20–40 μm) particles of non-stoichiometric TiC_x, beneath which there is a less compact zone composed of smaller TiC_x particles (5–15 μm) embedded in aluminum. In the central region of the ceramic, two phases are observed – Al and the intermetallic compound $TiAl_3$. It is worth noting that in an open pore within the Al matrix, where significant amounts of Al_4C_3 and Al_2O_3 phases were detected, local EDS analysis revealed an atomic ratio corresponding to the compound Al_2CO. It is known that this compound may act as an intermediate phase in the Al_4C_3–Al_2O_3 phase diagram [29].

It is likely that the molten aluminum, having filled a relatively large open pore (capillary), continued to penetrate into narrower capillaries between TiC particles, infiltrating the internal structure of the ceramic region with partial dissolution of TiC and subsequent formation of $TiAl_3$. The presence of a significant amount of aluminum carbide (and oxycarbide) in the large open pore is attributed to the fact that the excess graphite, remaining after the formation of the TiC SHS frame-

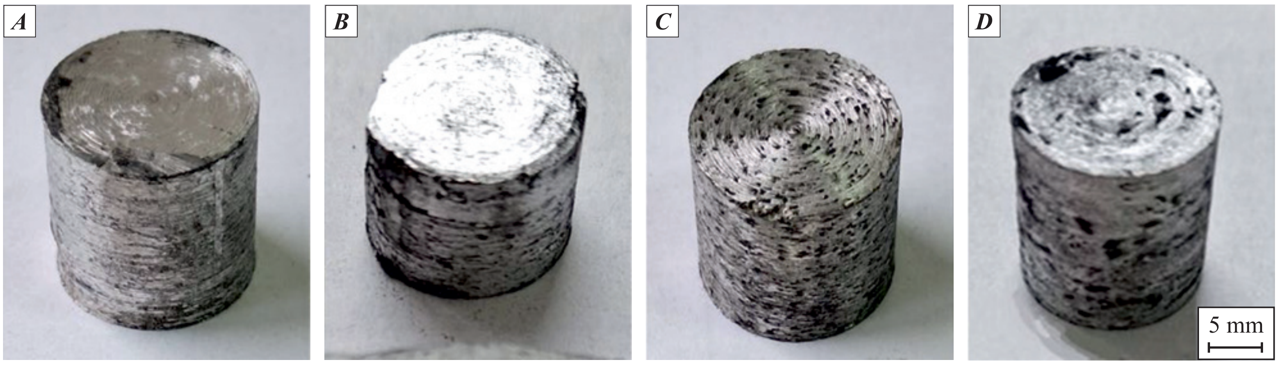

Fig. 2. External appearance of TiC–Al (***A***), TiC–C(S-2)–Al (***B***), TiC–C(GMZ)–Al (***C***), TiC–C(CF)–Al (***D***) composites

Рис. 2. Внешний вид композитов TiC–Al (***A***), TiC–C(С-2)–Al (***B***), TiC–C(ГМЗ)–Al (***C***) и TiC–C(УВ)–Al (***D***)

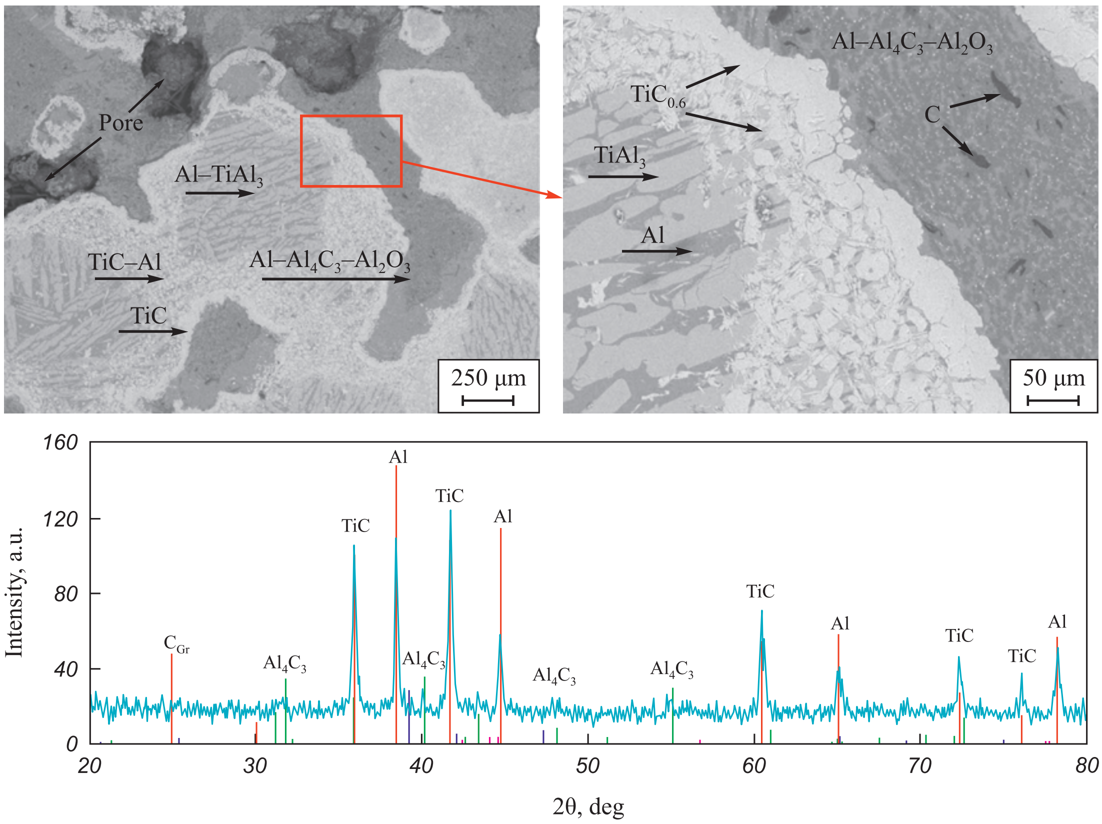

Fig. 3. Microstructure (top) and *X*-ray diffraction pattern (bottom) of the TiC–C(15 μm)–Al composite

Рис. 3. Микроструктура (сверху) и рентгеновская дифрактограмма (снизу) композита TiC–C(15 мкм)–Al

work, was concentrated in open pores and channels, which were subsequently filled with molten aluminum. In addition, isolated graphite particles measuring 15–30 μm were found within the Al matrix. The XRD pattern in Fig. 3 confirms the presence of the aforementioned phases; however, the peaks corresponding to TiAl$_3$, Al$_2$O$_3$, and graphite are within the background noise, indicating their low content in the composite.

Thus, graphite particles sized 10–15 μm almost completely dissolved in the molten aluminum, forming the secondary phase Al$_4$C$_3$. The formation of Al$_4$C$_3$ and TiAl$_3$ secondary phases in the TiC–Al system contributes to effective reactive wetting and strong adhesion between the metal and ceramic phases, which typically ensures high mechanical properties of the composite material [15]. According to the results of quantitative phase analysis, the phase composition of this composite is approximately as follows: 45–55 % Al, 35–40 % TiC, and up to 15 % secondary phases (Al$_4$C$_3$, TiAl$_3$, Al$_2$O$_3$). These values are approximate, since the XRD-based evaluation method has an error margin of up to 20 %, and the composite exhibits structural heterogeneity resulting from powder charge filling into the cylindrical crucible and the intense combustion process. The porosity of the TiC–C(S-2)–Al composite is approximately 7 %, and its average density is 3.11 g/cm^3.

The microstructure and XRD pattern of the TiC–C(GMZ)–Al composite, fabricated using GMZ graphite with a particle size of 100–1000 μm, are shown in Fig. 4. Three regions with distinct colors and structural features are clearly visible. The most extensive area, appearing gray, corresponds to the aluminum matrix, within which large black regions (graphite), clusters of fine white particles (TiC), and a few elongated acicular gray particles were observed. These were identified as Al$_2$CO or a mixture of Al$_4$C$_3$ and Al$_2$O$_3$. The main differences compared to the composite prepared with fine graphite are the presence of large free graphite particles and a lower content of interfacial reaction products (TiAl$_3$, Al$_4$C$_3$, and Al$_2$O$_3$). In addition, the observed TiC$_{0.9}$ phase contains more carbon, with a composition close to the stoichiometric TiC.

The XRD pattern in Fig. 4 confirms the phase composition observed in the microstructure and identified by EDS analysis. A noticeable increase in the intensity of the free graphite peak compared to the data in Fig. 3 clearly indicates the retention of large graphite particles in the Al matrix, in contrast to the fine graphite particles, which almost completely dissolve in molten aluminum during composite fabrication. Quantitative phase analysis shows the following approximate composition of the obtained composite: 40–45 % Al,

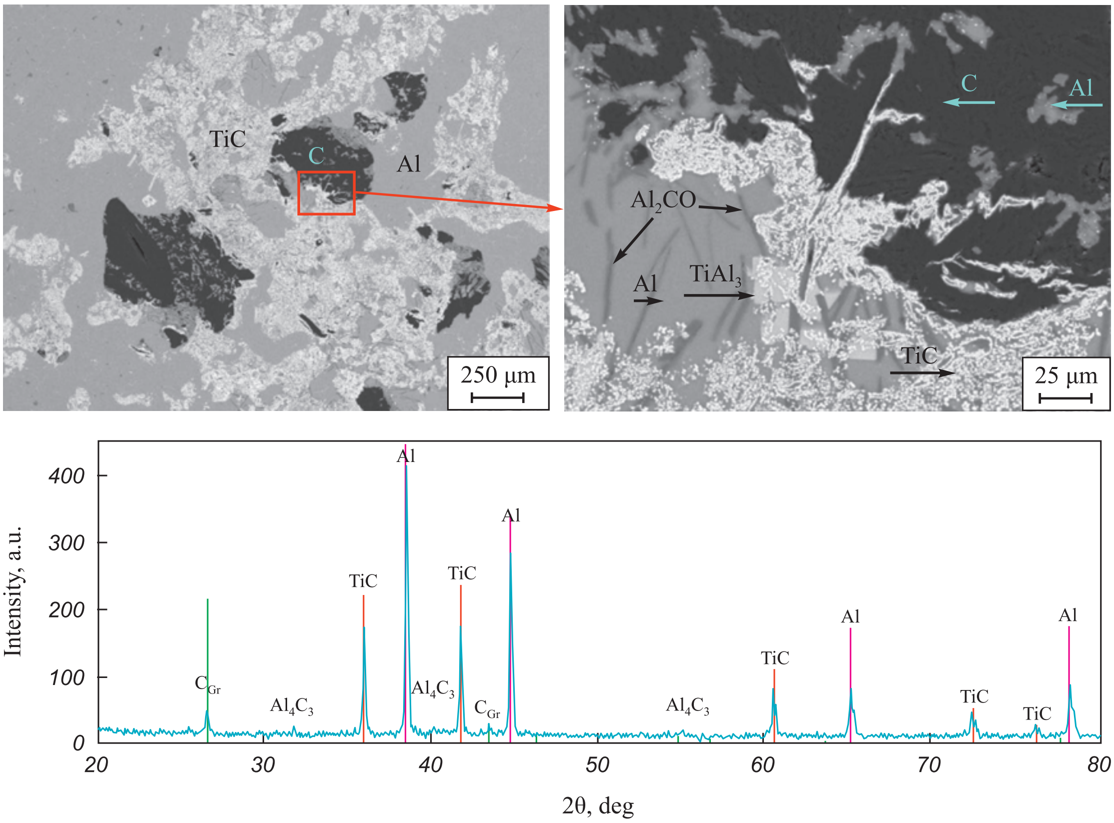

Fig. 4. Microstructure (top) and *X*-ray diffraction pattern (bottom) of the TiC–C(100–1000 µm)–Al composite

Рис. 4. Микроструктура (сверху) и рентгеновская дифрактограмма (снизу) композита TiC–C(100–1000 мкм)–Al

30–40 % TiC, 3–4 % graphite, and up to 15 % secondary phases (Al_4C_3, $TiAl_3$, Al_2O_3). The average porosity of the TiC–C(GMZ)–Al composite was 3.4 %, and its average density was 2.99 g/cm^3.

The microstructure and *X*-ray diffraction pattern of the TiC–C(CF)–Al composite, fabricated with the addition of carbon fiber, are shown in Fig. 5. The gray aluminum matrix contains regions consisting of clusters of equiaxed TiC particles and black carbon fibers. Due to their different spatial orientations, the carbon fibers appear in either longitudinal or cross-section views. In the longitudinal view, ring-like structures approximately 10 µm in diameter are observed around the fibers, consisting of fine TiC particles less than 2 µm in size. These particles are presumed to form via a different mechanism, possibly related to the interaction between Al_4C_3 and $TiAl_3$ in the aluminum melt within a specific temperature range during cooling of the composite [15]. Outside the ring-shaped TiC particle zones, virtually no titanium carbide particles are observed in the aluminum matrix. Partial dissolution of carbon fibers in molten aluminum is indicated by a reduction in their diameter from the original 7 µm to 3–5 µm and the presence of Al_4C_3 around the fibers within the TiC rings. The XRD pattern confirms the presence of the main phases – Al, TiC, and, to a lesser extent, Al_4C_3. Free graphite was not detected, as the carbon fibers preserved in the composite have an amorphous structure that is not detectable by XRD. According to the results of quantitative analysis, the approximate phase composition of the material is: 70–75 % Al, 15–20 % TiC, up to 3 % CF, and up to 15 % secondary phases (Al_4C_3, $TiAl_3$, Al_2O_3). The increased aluminum content and reduced TiC content are explained by the fact that when titanium and graphite powders are mixed with carbon fibers, the fibers tend to separate into thinner individual filaments, which greatly increases the total volume of the powder charge. As a result, after SHS, a TiC–CF framework is formed with greater porosity, allowing infiltration by a larger volume of molten aluminum compared to the TiC – graphite frameworks. Consequently, the average porosity of the final TiC–C(CF)–Al composite was only 1.9 %, the lowest among all samples, as was its average density, which was 2.74 g/cm^3. The synthesis and structural features of porous TiC–CF SHS-based composite materials represent a separate subject requiring further investigation.

Due to the relatively high content of undesirable aluminum carbide (Al_4C_3) in the TiC–C(C-2)–Al composite fabricated with an excess of fine (15 µm) graphite powder grade C-2, its mechanical and tribologi-

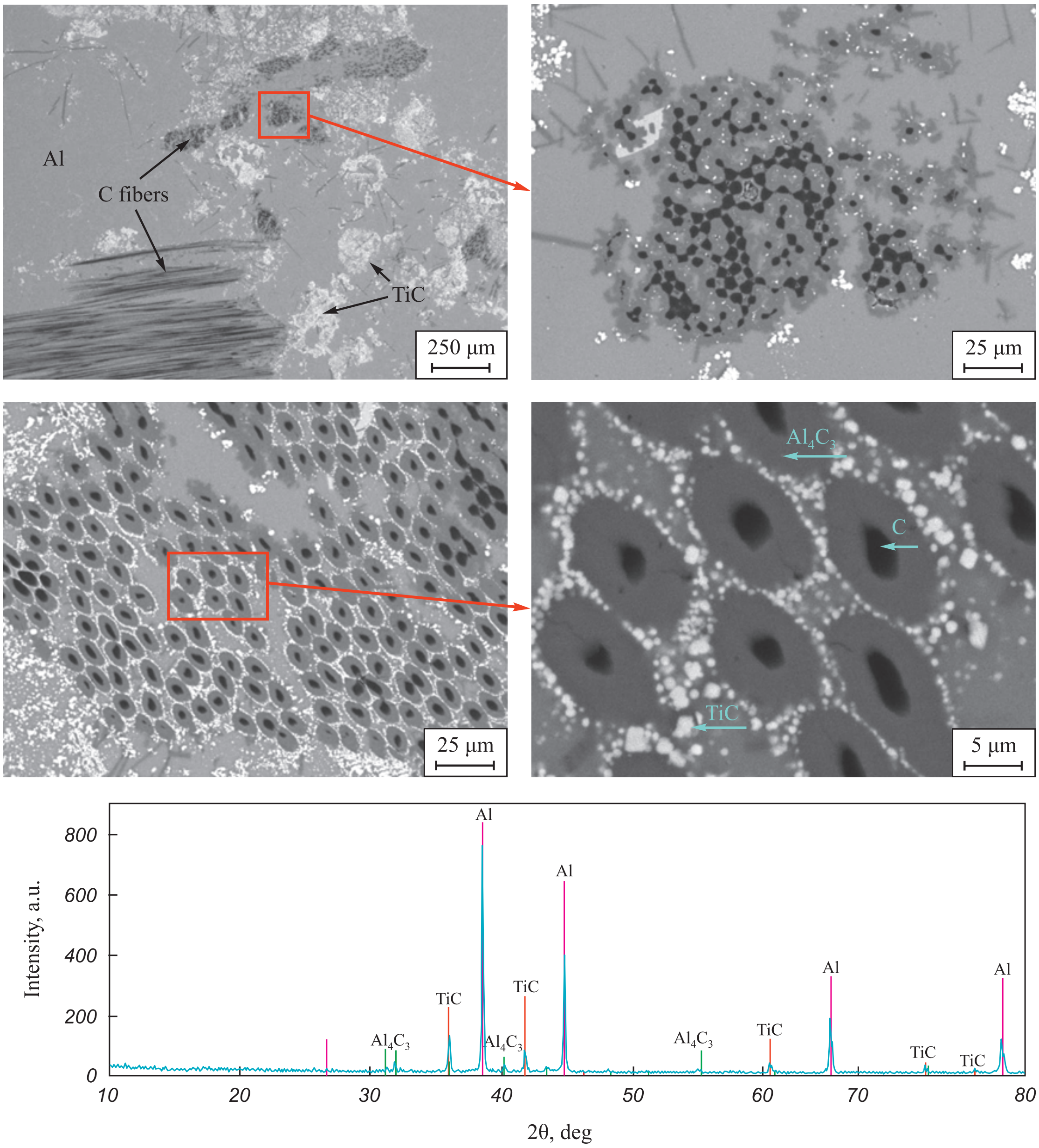

Fig. 5. Microstructure (top) and *X*-ray diffraction pattern (bottom) of the TiC–C(CF)–Al composite

Рис. 5. Микроструктура (сверху) и рентгеновская дифрактограмма (снизу) композита TiC–C(УВ)–Al

cal properties were not investigated. Al_4C_3 reacts with water to form Al_2O_3 and CH_4, making such composites phase- and structurally unstable not only in water but also in humid environments.

The results of density, hardness, and compressive property evaluation for the remaining samples of the studied TiC–Al and TiC–C–Al composite systems are presented in Table 1. As an example, Fig. 6 shows the compressive loading curves for each sample, reflecting the average result obtained from a series of tests on two samples. It can be seen that the TiC–C(100–1000 µm)–Al composite is brittle, while the other composites inherit the properties of the matrix and remain ductile.

The results obtained from the tribological tests are summarized in Table 2, while the general appearance of wear damage on the composite samples and indenters is shown in Fig. 7. The reported test results represent the arithmetic mean and standard deviation of the measured parameters, calculated from three identical tests conducted for each material.

Microscopic analysis of wear damage showed that the wear of the indenters is predominantly of abrasive origin, as evidenced by scratch marks aligned with the sliding direction (see central insets in Fig. 7, *a*–*c*). On the wear tracks of the tested composite samples, both scratches and signs of adhesive interaction between the contact surfaces are observed. Based on

Table 1. **Basic physical and mechanical properties of SHS-fabricated composites**

Таблица 1. **Основные физико-механические характеристики СВС-композитов**

Parameter	TiC–Al	TiC–C(100–1000 μm)–Al	TiC–C(CF)–Al
Density, g/cm^3	3.12 ± 0.01	2.99±0.04	2.74 ± 0.09
Porosity, %	6.6	3.4	1.9
Hardness, HB	66.1 ± 3.9	59.9 ± 3.0	49.3 ± 9.4
Slope of the linear section of the $\sigma^c = f(\varepsilon)$ curve ($\text{tg}^c\alpha$)	269.5 ± 19.1	173.5 ± 77.1	60.5 ± 41.7
Conventional compressive yield strength ($\sigma^c_{0.2}$), MPa	131.5 ± 16.3	135.5 ± 7.8	82.0 ± 9.9
Compressive strength (σ^{c*}_u), MPa	233.5 ± 13.4	203.5 ± 2.1	221.1 ± 18.4

Table 2. **Results of tribological testing of SHS-fabricated composites**

Таблица 2. **Результаты трибологических исследований СВС-композитов**

Parameter*	TiC–Al	TiC–C(100–1000 μm)–Al	TiC–C(CF)–Al
Tested materials			
S, mm	1.308 ± 0.174	1.033 ± 0.219	1.246 ± 0.109
h, μm	49.742 ± 23.490	26.240 ± 5.368	48.543 ± 16.453
V, mm^3	0.656 ± 0.300	0.221 ± 0.186	0.608 ± 0.319
$\dot{I}$, mm^3/min	$(9.889 \pm 4.527)\cdot10^{-3}$	$(3.332 \pm 2.798)\cdot10^{-3}$	$(9.156 \pm 0.005)\cdot10^{-3}$
W, mm^{-2}	$(4.686 \pm 2.879)\cdot10^5$	$(1.883 \pm 1.512)\cdot10^6$	$(4.828 \pm 2.067)\cdot10^5$
ε_I	1.0	3.0	1.1
Counterbody (spherical steel indenter)			
d, mm	1.516 ± 0.198	1.367 ± 0.051	1.386 ± 0.120
V, mm^3	0.045 ± 0.021	0.028 ± 0.004	0.030 ± 0.011
$\dot{I}$, mm^3/min	$(0.675 \pm 0.320)\cdot10^{-3}$	$(0.417 \pm 0.064)\cdot10^{-3}$	$(0.452 \pm 0.166)\cdot10^{-3}$
W, mm^{-2}	$(6.774 \pm 3.871)\cdot10^6$	$(9.176 \pm 1.318)\cdot10^6$	$(8.997 \pm 2.746)\cdot10^6$
ε_I	1.0	1.6	1.5
General characteristics of the friction pair			
μ_{max}	1.692 ± 0.214	1.639 ± 0.222	1.781 ± 0.111
μ_{av}	0.881 ± 0.041	0.982 ± 0.076	0.919 ± 0.177
α	0.5	0.6	0.5

*S and h – average wear track width and depth; V – volumetric wear; $\dot{I}$ – wear rate; W – wear resistance; ε_I – relative wear resistance; μ_{av} and μ_{max} – average and maximum kinetic coefficient of friction; α – friction coefficient stability.

the above observations, it can be concluded that in the friction pair 100Cr6/TiC–C–Al (with carbon additive content $C \geq 0$), adhesion is promoted by the soft aluminum matrix, which occupies the larger volume fraction in the composite and has the lowest melting point. The hard refractory particles TiC, Al_2O_3, Al_2CO, $TiAl_3$, and Al_4C_3 suppress adhesion but act as sources of abrasive damage to the contact surfaces. Logically, the abrasive effect is caused by both the particles embedded in the composite structure and those released into the wear debris in free form.

Another component of the wear debris consists of particles originating from the steel ball indenter. On the one hand, these particles serve as abrasives; on the other, like the Al matrix, they contribute to adhesion between the sample and the indenter. Nevertheless, under the tested conditions, the predominant wear mechanism should be considered abrasive wear. This conclusion is supported by the observation that during sliding, wear debris becomes embedded in the soft matrix, gradually altering the surface composition of the composites by increasing the proportion of hard

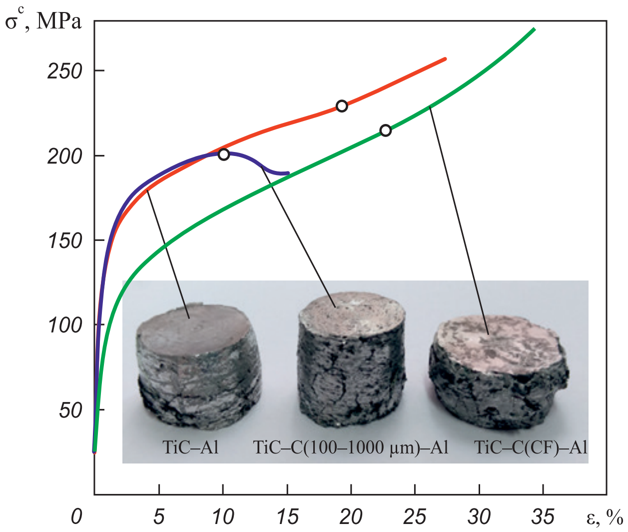

Fig. 6. General appearance of the composite samples after compression testing and the corresponding stress–strain curves

Asterisks indicate the values of σ_u^{c*}

Рис. 6. Общий вид образцов композитов после испытаний на сжатие и соответствующие кривые нагружения

Точками отмечены значения σ_u^{c*}

particles. This explains the purely abrasive wear observed on the indenter. According to the hypothesis proposed in [30], at C = 0 the instantaneous wear rate should reach a constant value, while at C > 0 it should gradually decrease. Verification of this hypothesis would require the use of precision methods to monitor wear kinetics and related effects during testing, which is the subject of future dedicated tribological studies. Within the scope of the present work, the following conclusions can be drawn.

The presence of graphite in the TiC–C–Al composite increased the average coefficient of friction but reduced its maximum value as well as all wear-related parameters (see Table 2), especially in the case of coarse graphite (100–1000 μm) addition, where the lowest wear was recorded for both the composite and the indenter, along with the highest friction stability (α). According to the relative wear resistance parameter (ε_I), the addition of carbon resulted in a clear reduction in wear of both the TiC–C(100–1000 μm)–Al and TiC–C(CF)–Al composites compared to the baseline TiC–Al composite. A sharp increase in indenter wear resistance was also observed for TiC–C(100–1000 μm)–Al, while the improvement was less pronounced for TiC–C(CF)–Al.

Profilometric analysis revealed that in the 100Cr6/TiC–Al pair, mutual abrasive wear of both the ball and the sample occurs, resulting in a wear track cross-section close to a circular shape along the entire depth of wear (see Fig. 7, *d* and Table 2). In the 100Cr6/TiC–C(100–1000 μm)–Al pair, the predominant wear occurs on the ball, as the sample shows

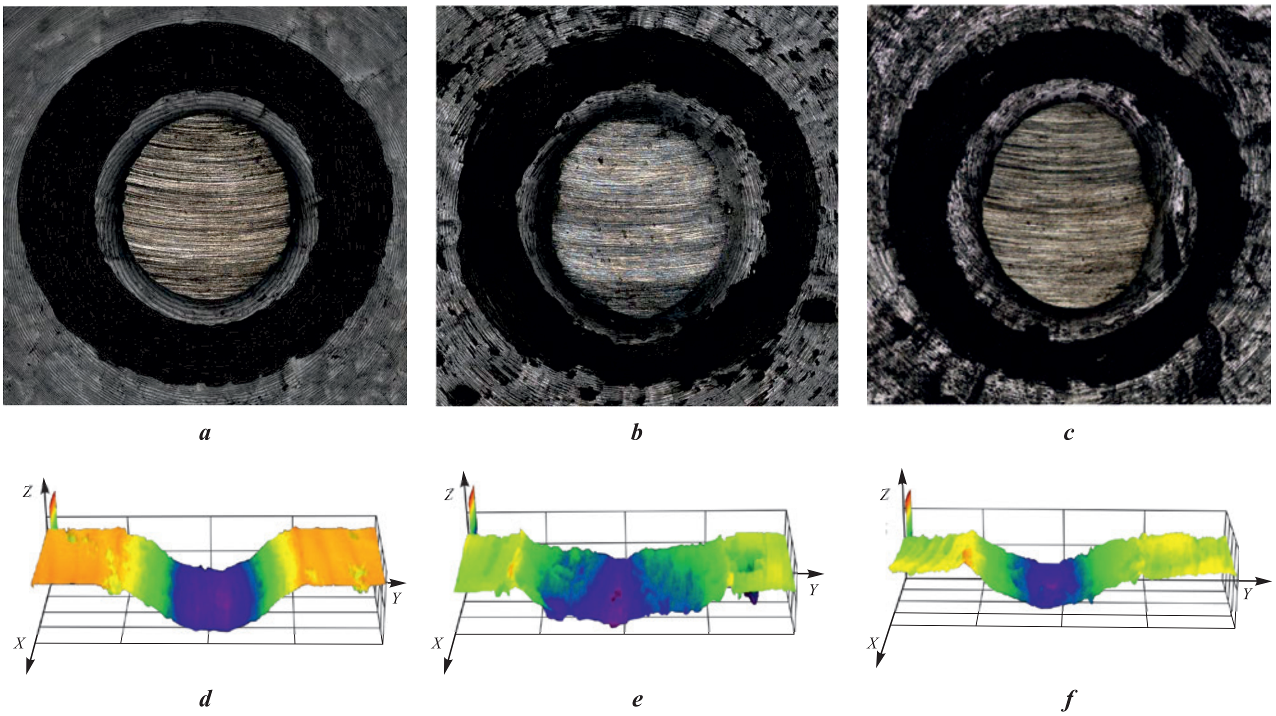

Fig. 7. General view of wear damage on composite samples and indenters (***a–c***), and 3D cross-sectional profiles of wear tracks (***d–f***)

a, ***d*** – TiC–Al; ***b***, ***e*** – TiC–C(100–1000 μm)–Al; ***c***, ***f*** – TiC–C(CF)–Al

Рис. 7. Общий вид повреждений образцов и инденторов (***a–c***), а также 3D-профиль сечения дорожек трения (***d–f***)

a, ***d*** – TiC–Al; ***b***, ***e*** – TiC–C(100–1000 мкм)–Al; ***c***, ***f*** – TiC–C(УВ)–Al more uniform wear over the contact area with only slight penetration (Fig. 7, *e*, Table 2). The wear mode in the 100Cr6/TiC–C(CF)–Al pair is intermediate – it penetrates deeper but forms a cross-sectional profile resembling a triangle (Fig. 7, *f*, Table 2). This supports the idea that carbon fiber begins to function as a lubricant at a certain point in the test, once the contact pressure decreases due to wear and sufficient amounts of CF-containing debris accumulate on the friction surface to provide lubrication.

As also shown in Table 2, the studied materials consistently fall into wear resistance class 5 ($W \sim 10^5 \div 10^6$ mm^{-2}), while the steel counterbody corresponds to class 6 ($W \sim 10^6 \div 10^7$ mm^{-2}). The addition of coarse graphite (100–1000 μm) increases the class rating to 6 and 7, respectively. Considering that sliding bearings typically use materials of wear resistance classes 5–8 [31], the studied composites are promising for such applications, even under dry friction conditions. It is known that the service life of a tribological assembly can be significantly extended in the presence of a liquid lubricant. In this regard, the porosity of SHS-fabricated TiC–C–Al composites may play a beneficial role by enabling oil impregnation and operation in a lubricated environment. However, such operating conditions and wear modes require further experimental studies and will be the subject of future research.

The standard deviations of the wear evaluation parameters (see Table 2) indicate a wide scatter in the tribological test results, which, as noted earlier, can be attributed to the inhomogeneous distribution of TiC and C particles in the Al matrix and the inherent porosity of the composite materials. This leads to high friction coefficients and uneven wear track widths and depths (see Table 2 and Fig. 7). Nonetheless, it is worth noting that the addition of coarse graphite (100–1000 μm), even under these structurally inhomogeneous conditions, improves the frictional stability.

Conclusions

1. The feasibility of fabricating hybrid composites of the TiC–C–Al system was examined by combining SHS for the synthesis of a porous TiC–C ceramic–carbon framework with subsequent spontaneous infiltration using molten aluminum. Three types of composites were produced with 100 % excess carbon – relative to the carbon mass in the stoichiometric Ti + C mixture – added to the initial powder charge in the form of fine and coarse graphite powders and chopped carbon fiber: TiC–C(15 μm)–Al, TiC–C(100–1000 μm)–Al, and TiC–C(CF)–Al. For comparison, a TiC–Al composite without excess carbon was also fabricated.

2. The reactive nature of TiC and C wetting by molten aluminum was confirmed by the increased content of secondary interfacial reaction products such as Al_4C_3, $TiAl_3$, Al_2O_3, and possibly Al_2CO. Their total content reached up to 15% in all three composites synthesized with excess carbon, while in the sample without such additives it did not exceed 5 %.

3. The use of excess fine graphite (15 μm, grade C-2) in the charge leads to its almost complete dissolution in molten Al and its absence in the final composite. The use of coarse graphite (100–1000 μm) significantly reduces interfacial interaction and largely preserves it in the form of free graphite in the resulting composite (up to 3–4 %). Carbon fiber demonstrates intermediate stability in molten Al compared to fine and coarse graphite powders, with up to 3 % of free carbon retained in the composite in the form of amorphous carbon fibers.

4. The ratio of TiC–C ceramic to Al metal content in the hybrid composites and their residual porosity significantly depend on the type of excess carbon additive (graphite or carbon fiber). The TiC phase concentration is highest in the TiC–Al composite without excess carbon (50–55 %), as is the porosity, which can reach up to 8 %. When excess carbon is introduced, the TiC content and porosity decrease to 35–40 % and 7 %, respectively, in the case of fine graphite (C-2); to 30–40 % and 3.4 % with coarse graphite (GMZ); and to 15–20 % and 1.9 % when carbon fiber is used. In the latter case, the Al phase content reaches its maximum value of 70–75 %.

5. The compressive strength of the Al-matrix composites TiC–Al, TiC–C(100–1000 μm)–Al, and TiC–C(CF)–Al was 233.5, 203.5, and 221.1 MPa, respectively, while the conventional compressive yield strength was 131.5, 135.5, and 82.0 MPa, respectively. Thus, the introduction of excess carbon and its presence in the final composite reduce the strength of the hybrid composites compared to the TiC–Al sample without carbon addition. At the same time, the TiC–C(100–1000 μm)–Al composite exhibits brittle behavior, whereas the other composites inherit the properties of the matrix and remain sufficiently ductile.

6. During friction and wear of the investigated TiC–C–Al hybrid composites in contact with a steel counterbody, abrasive wear was found to be the dominant mechanism, accompanied by a high coefficient of friction (0.88–0.98). Under these conditions, the TiC–C(100–1000 μm)–Al composite demonstrated the best tribological performance, with three times lower wear, which is attributed to the presence of self-lubricating properties retained from the beginning of the friction and wear process. It was shown that all the studied variants of hybrid composites are promising for use in sliding bearing applications. Moreover, their porosity, despite its observed negative effect on the stability of friction and wear behavior, may potentially be advantageous for lubricant impregnation in future applications.

7. Further research is planned to focus on identifying Al-based matrix alloys for tribological applications that exhibit lower chemical reactivity toward graphite during infiltration, which would enable further improvement of the tribological performance of TiC – graphite – Al(alloy) composites. It is also necessary to study in more detail the kinetics of wear accumulation, variations in the coefficient of friction, and related effects (e.g., acoustic emission) during the friction and wear of TiC–C–Al hybrid composites under dry and boundary lubrication conditions, including after lubricant impregnation and immersion in a liquid lubrication medium.

References / Список литературы

1. Rohatgi P.K., Tabandeh-Khorshid M., Omrani E., Lovell M.R., Menezes P.L. Tribology of metal matrix composites. In: *Tribology for Scientists and Engineers*. NY: Springer, 2013. P. 233–268. https://doi.org/10.1007/978-1-4614-1945-7_8
2. Ayar M.S., George P.M., Patel R.R. Advanced research progresses in aluminium metal matrix composites: An overview. In: *Proceedings of the 14th Asia-Pacific physics conference*. AIP Publishing, 2021. No. 2317(1). P. 20–26. https://doi.org/10.1063/5.0036141
3. Kar A., Sharma A., Kumar S. A critical review on recent advancements in aluminium-based metal matrix composites. *Crystals (Basel)*. 2024;14(5):412. https://doi.org/10.3390/cryst14050412
4. Ajay K.P., Rohatgi P., Weiss D. 50 Years of foundry-produced metal matrix composites and future opportunities. *International Journal of Metalcasting*. 2020;14(2):291–317. https://doi.org/10.1007/s40962-019-00375-4
5. Kostikov V. Composite materials based on aluminum alloys reinforced with carbon fibers. Moscow: Intermet Engineering, 2000. 445 p. (In Russ.).

   Костиков В. Композиционные материалы на основе алюминиевых сплавов, армированных углеродными волокнами. М.: Интермет Инжиниринг, 2000. 445 с.
6. Singh N., Belokar R.M., Walia R.S. A critical review on advanced reinforcements and base materials on hybrid metal matrix composites. *Silicon*. 2022;14(2):1–24. https://doi.org/10.1007/s12633-020-00853-z
7. Arunkumar S., Guhan R., Srivathsan A., Rithik A. Fabrication methods of aluminium metal matrix composite: A state of review. *International Research Journal on Advanced Engineering and Management (IRJAEM)*. 2024;2(03):528–537. https://doi.org/10.47392/irjaem.2024.0073
8. Rogachev A.S., Mukasyan A.S. Combustion for material synthesis. New York: CRC Press, 2014. 424 p. https://doi.org/10.1201/b17842
9. Borovinskaya I., Gromov A., Levashov E., Maksimov Y., Mukasyan A., Rogachev A. Concise encyclopedia of self-propagating high-temperature synthesis: History, theory, technology, and products. Elsevier, 2017. 432 p.
10. Kaya M., Orhan N., Tosun G. The effect of the combustion channels on the compressive strength of porous NiTi shape memory alloy fabricated by SHS as implant material. *Current Opinion in Solid State and Materials Science*. 2010;14(1):21–25. https://doi.org/10.1016/j.cossms.2009.07.002
11. Rohatgi P.K., Gupta N., Alaraj S. Thermal expansion of aluminum–fly ash cenosphere composites synthesized by pressure infiltration technique. *Journal of Composite Materials*. 2006;40(13):1163–1174. https://doi.org/10.1177/0021998305057379
12. Zhou S.M., Zhang X.B, Ding Z.P., Min C.Y., Xu G.L., Zhu W.M. Fabrication and tribological properties of carbon nanotubes reinforced Al composites prepared by pressureless infiltration technique. *Composites. Part A: Applied Science and Manufacturing*. 2007;38(2):301–306. https://doi.org/10.1016/j.compositesa.2006.04.004
13. Gulevsky V.A., Miroshkin N.Yu., Tsurikhin S.N., Gundrov O.Yu. More details about impregnation of carbon graphite with aluminum. *Izvestiya Volgogradskogo gosudarstvennogo tekhnicheskogo universiteta*. 2020;(7(242)):77–82. (In Russ.). https://doi.org/10.35211/1990-5297-2020-7-242-77-82

    Гулевский В.А., Мирошкин Н.Ю., Цурихин С.Н., Гундров О.Ю. Подробнее о пропитке углеграфита алюминием. *Известия Волгоградского государственного технического университета*. 2020;7(242):77–82. https://doi.org/10.35211/1990-5297-2020-7-242-77-82
14. Lee M., Choi Y., Sugio K., Matsugi K., Sasaki G. Effect of aluminum carbide on thermal conductivity of the unidirectional CF/Al composites fabricated by low pressure infiltration process. *Composites Science and Technology*. 2014;97:1–5. https://doi.org/10.1016/j.compscitech.2014.03.022
15. Contreras Cuevas A., Bedolla Becerril E., Martínez M.S, Lemus Ruiz J. Fabrication processes for metal matrix composites. In: *Metal Matrix Composites: Wetting and Infiltration*. Cham: Springer Nature Switzerland AG, 2018. P. 83–114. https://doi.org/10.1007/978-3-319-91854-9_3
16. Mikheev R.S. Promising coatings with enhanced tribotechnical properties made of composite materials based on non-ferrous metals: Abstract of the dissertation of Dr. Sci.(Eng.). Moscow: Institute of Metallurgy and Materials Science named after A. A. Baykov, 2018. (In Russ.).

    Михеев Р.С. Перспективные покрытия с повышенными триботехническими свойствами из композиционных материалов на основе цветных металлов: Автореф. дис.… д.т.н. М.: Институт металлургии и материаловедения им. А.А. Байкова, 2018.
17. Riahi A.R., Alpas A.T. The role of tribo-layers on the sliding wear behavior of graphitic aluminum matrix composites. *Wear*. 2001;1(1-12):1396–1407. https://doi.org/10.1016/S0043-1648(01)00796-7
18. Ravindran P., Manisekar K., Narayanasamy R., Narayanasamy P. Tribological behaviour of powder metallurgy-

processed aluminium hybrid composites with the addition of graphite solid lubricant. *Ceramics International*. 2013;39(2):1169–82.
https://doi.org/10.1016/j.ceramint.2012.07.041

19. Baradeswaran A., Perumal A.E. Wear and mechanical characteristics of Al 7075/graphite composites. *Composites. Part B: Engineering*. 2014;56:472–476.
https://doi.org/10.1016/j.compositesb.2013.08.073

20. Scaria C.T., Pugazhenthi R., Daniel A.A., Santhosh K. Mechanical and wear studies on AA7075/nano TiC/graphite hybrid composites for tribological applications. *Advances in Materials Science and Engineering*. 2022;(1):1–8.
https://doi.org/10.1155/2022/5320363

21. Fallahdoost H., Nouri A., Azimi A. Dual functions of TiC nanoparticles on tribological performance of Al/graphite composites. *Journal of Physics and Chemistry of Solids*. 2016;93:137–144.
https://doi.org/10.1016/j.jpcs.2016.02.020

22. Umerov E.R., Latukhin E.I., Amosov A.P., Kichaev P.E. Preparation of Ti_3SiC_2–Sn(Pb) cermet by SHS of Ti_3SiC_2 porous skeleton with subsequent spontaneous infiltration with Sn–Pb melt. *International Journal of Self-Propagating High-Temperature Synthesis*. 2023;32(1):30–35.
https://doi.org/10.3103/S1061386223010089

23. Latukhin E.I., Umerov E.R., Amosov A.P. Preparation of Ti_3AlC_2–Al cermets by combined use of SHS of Ti_3AlC_2 porous skeleton and spontaneous infiltration with Al and Al-based melts. *International Journal of Self-Propagating High-Temperature Synthesis*. 2023;32(1):23–29.
https://doi.org/10.3103/S1061386223010041

24. Amosov A.P., Latukhin E.I., Umerov E.R. Applying infiltration processes and self-propagating high-temperature synthesis for manufacturing cermets: A review. *Russian Journal of Non-Ferrous Metals*. 2022;63(1):81–100.
https://doi.org/10.3103/S1067821222010047

Амосов А.П., Латухин Е.И., Умеров Э.Р. Применение процессов инфильтрации и самораспространяющегося высокотемпературного синтеза для получения керметов: Обзор. *Известия вузов. Цветная металлургия*. 2021;27(6):52–75.
https://doi.org/10.17073/0021-3438-2021-6-52-75

25. Davydov D.M., Amosov A.P., Latukhin E.I., Umerov E.R., Novikov V.A. Features of the composition and microstructure of porous skeletons of MAX-phases Ti_3AlC_2 and Ti_3SiC_2 produced by the SHS method in air and in a protective shell of sand. *Vestnik Sibirskogo gosudarstvennogo industrial'nogo universiteta*. 2023;(4):88–97. (In Russ.).
https://doi.org/10.57070/2304-4497-2023-4(46)-88-97

Давыдов Д.М., Амосов А.П., Латухин Е.И., Умеров Э.Р., Новиков В.А.. особенности состава и микроструктуры пористых каркасов MAX-фаз Ti_3AlC_2 и Ti_3SiC_2, получаемых методом СВС на воздухе и в защитной оболочке из песка. *Вестник Сибирского государственного индустриального университета*. 2023;4:88–97.
https://doi.org/10.57070/2304-4497-2023-4(46)-88-97

26. Davydov D.M., Umerov E.R., Amosov A.P., Latukhin E.I. Influence of starting reagents on the formation of Ti_3SiC_2 porous skeleton by SHS in air. International *Journal of Self-Propagating High-Temperature Synthesis*. 2024;33(1):26–32.
https://doi.org/10.3103/S1061386224010023

27. Amosov A., Amosov E., Latukhin E., Kichaev P., Umerov E. Producing TiC–Al cermet by combustion synthesis of TiC porous skeleton with spontaneous infiltration by aluminum melt. In: *Proc. 2020 7th International Congress on Energy Fluxes and Radiation Effects. IEEE*. 2020. P. 1057–1062.
https://doi.org/10.1109/EFRE47760.2020.9241903

28. Umerov E.R. Manufacturing cermets using self-propagating high-temperature synthesis of ceramic skeletons TiC, Ti_3SiC_2, Ti_3AlC_2 and subsequent spontaneous infiltration with melts of metals Al, Sn, Cu: Abstract of the Dissertation of Cand. Sci.(Eng.). Samara: SamSTU, 2023. (In Russ.).

Умеров Э.Р. Получение керметов с использованием самораспространяющегося высокотемпературного синтеза керамических каркасов TiC, Ti_3SiC_2, Ti_3AlC_2 и последующей самопроизвольной инфильтрации расплавами металлов Al, Sn, Cu: Автореф. дис.… к.т.н. Самара: СамГТУ, 2023.

29. Foster L.M., Long G., Hunter M.S. Reactions between aluminum oxide and carbon the Al_2O_3–Al_4C_3 phase diagram. *Journal of the American Ceramic Society*. 1956;39(1):1–11.
https://doi.org/10.1111/j.1151-2916.1956.tb15588.x

30. Umerov E., Amosov A., Latukhin E., Kiran K.U., Choi H., Saha S., Roy S. Fabrication of MAX-phase composites by novel combustion synthesis and spontaneous metal melt infiltration: Structure and tribological behaviors. *Advanced Engineering Materials*. 2024;26(8):2301792.
https://doi.org/10.1002/adem.202301792

31. Chichinadze A., Berliner E., Braun E., Bushe N., Buyanovsky I., Hecker F. Friction, wear and lubrication (tribology and tribotechnics). Moscow: Mashinostroenie, 2003. 575 p. (In Russ.).

Чичинадзе А., Берлинер Э., Браун Э., Буше Н., Буяновский И., Геккер Ф. Трение, износ и смазка (трибология и триботехника). М.: Машиностроение, 2003. 575 с.

Information about the Authors

Emil R. Umerov – Cand. Sci. (Eng.), Leading Research Fellow of the Department of Metals Science, Powder Metallurgy, Nanomaterials, Samara State Technical University (SamSTU)
ORCID: 0000-0002-2050-6899
E-mail: umeroff2017@yandex.ru

Сведения об авторах

Эмиль Ринатович Умеров – к.т.н., вед. науч. сотрудник кафедры «Металловедение, порошковая металлургия, наноматериалы», Самарский государственный технический университет (СамГТУ)
ORCID: 0000-0002-2050-6899
E-mail: umeroff2017@yandex.ru

Aleksandr P. Amosov – Dr. Sci. (Phys.-Math.), Head of the Department of Metals Science, Powder Metallurgy, Nanomaterials, SamSTU
ORCID: 0000-0002-1510-6567
E-mail: egundor@yandex.ru

Evgeny I. Latukhin – Cand. Sci. (Eng.), Associate Professor of the Department of Metals Science, Powder Metallurgy, Nanomaterials, SamSTU
ORCID: 0000-0002-2071-3521
E-mail: evgelat@yandex.ru

Andrey D. Kachura – Postgraduate Student of the Department of Metals Science, Powder Metallurgy, Nanomaterials, SamSTU
ORCID: 0000-0001-9246-5638
E-mail: ruw223@mail.ru

Igor A. Rastegaev – Dr. Sci. (Eng.), Leading Researcher of the Magnesium Materials Design Laboratory, Togliatti State University (TSU)
ORCID: 0000-0003-3807-8105
E-mail: RastIgAev@yandex.ru

Maxim A. Afanasiev – Leading Engineer of the Magnesium Materials Design Laboratory, (TSU)
ORCID: 0000-0003-1424-7277
E-mail: maxwel-i@yandex.ru

Александр Петрович Амосов – д.ф.-м.н., зав. кафедрой «Металловедение, порошковая металлургия, наноматериалы», СамГТУ
ORCID: 0000-0002-1510-6567
E-mail: egundor@yandex.ru

Евгений Иванович Латухин – к.т.н., доцент кафедры «Металловедение, порошковая металлургия, наноматериалы», СамГТУ
ORCID: 0000-0002-2071-3521
E-mail: evgelat@yandex.ru

Андрей Дмитриевич Качура – аспирант кафедры «Металловедение, порошковая металлургия, наноматериалы», СамГТУ
ORCID: 0000-0001-9246-5638
E-mail: ruw223@mail.ru

Игорь Анатольевич Растегаев – д.т.н., вед. науч. сотрудник лаборатории дизайна магниевых материалов, Научно-исследовательский институт прогрессивных технологий, Тольяттинский государственный университет (ТГУ)
ORCID: 0000-0003-3807-8105
E-mail: RastIgAev@yandex.ru

Максим Анатольевич Афанасьев – вед. инженер лаборатории дизайна магниевых материалов, ТГУ
ORCID: 0000-0003-1424-7277
E-mail: maxwel-i@yandex.ru

Contribution of the Authors

E. R. Umerov – defined the purpose of the work, conducted experiments, wrote the article.
A. P. Amosov – defined the purpose of the work, participated in the discussion of the results, wrote the article.
E. I. Latukhin – conducted experiments, participated in the discussion of the results, wrote the article.
A. D. Kachura – prepared the charge mixtures and initial samples, participated in the discussion of the results.
I. A. Rastegaev – conducted tribological studies of the samples, participated in the discussion of the results.
M. A. Afanasiev – conducted studies of the mechanical properties of the samples, participated in the discussion of the results.

Вклад авторов

Э. Р. Умеров – определение цели работы, проведение экспериментов, написание текста статьи.
А. П. Амосов – определение цели работы, участие в обсуждении результатов, написание текста статьи.
Е. И. Латухин – проведение экспериментов, участие в обсуждении результатов.
А. Д. Качура – подготовка шихтовых смесей и исходных образцов, участие в обсуждении результатов.
И. А. Растегаев – проведение трибологических исследований образцов, участие в обсуждении результатов.
М. А. Афанасьев – проведение исследований механических свойств образцов, участие в обсуждении результатов.

Received 27.12.2024
Revised 09.01.2025
Accepted 14.01.2025

Статья поступила 27.12.2024 г.
Доработана 09.01.2025 г.
Принята к публикации 14.01.2025 г.

Refractory, Ceramic, and Composite Materials
Тугоплавкие, керамические и композиционные материалы

UDC 621.74 + 669.018

https://doi.org/10.17073/1997-308X-2025-2-39-50

Research article
Научная статья

Development of novel antifriction composite materials through reinforcement of AM4.5Kd and AK10M2N alloys with highly dispersed titanium carbide ceramic phase

A. R. Luts

Samara State Technical University
244 Molodogvardeyskaya Str., Samara 443100, Russia

alya_luts@mail.ru

Abstract. Composite materials based on aluminum alloys reinforced with a highly dispersed titanium carbide phase demonstrate enhanced antifriction properties, allowing them to be classified as promising tribotechnical materials. One of the most accessible and efficient methods for producing such composites is Self-Propagating High-Temperature Synthesis (SHS), which relies on the exothermic reaction between titanium and carbon precursors directly in the aluminum melt. This process enables the synthesis of a carbide phase with particle sizes ranging from 100 nm to 2 µm. The present study investigates the set of performance and processing characteristics of composites obtained via SHS of titanium carbide in melts of the industrial piston alloys AM4.5Kd and AK10M2N, aiming to assess their potential application as antifriction materials for manufacturing engine pistons. A comparative analysis was conducted on both the base alloys and the composite materials produced from them, after heat treatment including quenching and artificial aging under heat treatment conditions ensuring maximum hardness. The results demonstrated that in the AM4.5Kd–10 % TiC composite, the wear rate decreased by a factor of 2.4, the friction coefficient decreased by a factor of 2.7, and scuff resistance improved by a factor of 1.7 compared to the matrix alloy. In the AK10M2N–10 % TiC composite, the wear rate decreased by a factor of 17 and the friction coefficient decreased by a factor of 4, while maintaining the same level of scuff resistance as the matrix alloy. Both materials exhibited thermal self-heating during friction, a thermal linear expansion coefficient at 300 °C, heat resistance at 250 °C, fluidity, and linear shrinkage comparable to those of the matrix alloys (with variations within 10 %). The obtained data support the recommendation of these composites for use in the production of cast engine pistons as replacements for the original alloys.

Keywords: composite material, antifriction aluminum alloy, titanium carbide, self-propagating high-temperature synthesis, tribological properties

For citation: Luts A.R. Development of novel antifriction composite materials through reinforcement of AM4.5Kd and AK10M2N alloys with highly dispersed titanium carbide ceramic phase. *Powder Metallurgy and Functional Coatings*. 2025;19(2):39–50. https://doi.org/10.17073/1997-308X-2025-2-39-50

Разработка новых антифрикционных композиционных материалов путем армирования сплавов АМ4,5Кд и АК10М2Н высокодисперсной керамической фазой карбида титана

А. Р. Луц

Самарский государственный технический университет
Россия, 443100, г. Самара, ул. Молодогвардейская, 244

alya_luts@mail.ru

Аннотация. Композиционные материалы на основе алюминиевых сплавов, армированные высокодисперсной фазой карбида титана, характеризуются повышенными показателями антифрикционных свойств, что позволяет отнести их к группе перспективных триботехнических материалов. Одним из наиболее доступных и эффективных способов их изготовления является самораспространяющийся высокотемпературный синтез (СВС), который основан на экзотермическом взаимодействии прекурсоров титана и углерода непосредственно в алюминиевом расплаве и позволяет синтезировать карбидную фазу с размером частиц 100 нм – 2 мкм. Настоящая работа посвящена исследованию комплекса эксплуатационных и технологических характеристик композитов, полученных путем проведения СВС карбида титана в расплавах промышленных поршневых сплавов АМ4,5Кд и АК10М2Н, для определения возможности их применения в качестве антифрикционных материалов для изготовления поршней двигателей. Сравнительный анализ проводился на образцах исходных сплавов и полученных на их основах композиционных материалов после термической обработки в виде закалки и искусственного старения по режимам, обеспечивающим максимальные значения твердости. Результаты исследования показали, что у композита АМ4,5Кд–10 % TiC снизились скорость изнашивания в 2,4 раза, коэффициент трения в 2,7 раза и задиростойкость в 1,7 раза относительно матричного сплава, а у образца АК10М2Н–10 % TiC – скорость изнашивания уменьшилась в 17 раз и коэффициент трения в 4 раза при сохранении уровня задиростойкости. При этом оба материала характеризуются сопоставимыми (с изменениями в пределах 10 %) с показателями матричных сплавов уровнем саморазогрева в процессе трения, термическим коэффициентом линейного расширения при температуре 300 °C, жаропрочностью при 250 °C, жидкотекучестью и линейной усадкой. Полученные данные дают основание рекомендовать их к применению для изготовления отливок поршней двигателей вместо исходных сплавов.

Ключевые слова: композиционный материал (КМ), антифрикционный алюминиевый сплав, карбид титана, самораспространяющийся высокотемпературный синтез (СВС), трибологические свойства

Для цитирования: Луц А.Р. Разработка новых антифрикционных композиционных материалов путем армирования сплавов АМ4,5Кд и АК10М2Н высокодисперсной керамической фазой карбида титана. *Известия вузов. Порошковая металлургия и функциональные покрытия*. 2025;19(2):39–50. https://doi.org/10.17073/1997-308X-2025-2-39-50

Introduction

Antifriction materials with enhanced wear resistance are an essential component of modern mechanical engineering. These materials should have a low friction coefficient, exhibit plasticity, and ensure good running-in to the counterbody, while maintaining sufficient strength properties. Traditionally, babbitts and copper-based alloys such as brass and bronze have been widely used for these purposes. However, modern tribological assembly operating conditions necessitate reducing both the weight and cost of such materials, which has led to the increased adoption of aluminum-based antifriction materials. Replacing copper alloys with aluminum ones reduces the weight of a part of the same volume by a factor of 2.5–3.0 and significantly lowers casting costs. Aluminum alloys are easier to melt due to their lower melting point, are simpler to machine, and still possess sufficient strength and corrosion resistance. Furthermore, their high thermal conductivity helps maintain the lubricating layer at higher sliding speeds and under higher pressures [1–3].

The first aluminum-based antifriction alloys intended for bearings were developed according to the Sharpie principle, where the soft, plastic aluminum-based matrix contained intermetallic compounds ($CuAl_2$, $FeAl_3$, $NiAl_3$, Mg_2Si, etc.) that carried the primary load and formed a favorable microrelief capable of retaining the lubricant film. Later, to prevent excessive wear of shafts, low-melting tin and lead were introduced into the alloys, forming soft structural components that migrated to the surface during operation to create a protective film. This allowed such materials to be used under conditions of boundary and dry friction [4].

The most widely used alloys for manufacturing monometallic bearings are Al–Sn–Cu system alloys, such as AO3-7 and AO9-2, while bimetallic bearings utilize AO20-1, where strength is achieved through a thin antifriction layer (0.5–1.0 mm) applied onto a strong steel backing. However, despite their good antifriction properties, these alloys lack high mechanical properties, so research in this area continues.

One approach to addressing the insufficient mechanical properties of antifriction alloys involves their modification to enhance strength characteristics by refining the grain structure [5]. However, the effect of such refinement is usually limited. For this reason, researchers more often pursue the development of complexly alloyed materials containing a range of intermetallic phases that strengthen the matrix [6–9]. Specifically, there are reports of aluminum-based antifriction materials produced by introducing Cu, Si, Zn, and Ti, as well as 8–12 % Sn[1] and 2–4 % Pb into the alloy composition. Such materials meet all the requirements for sliding bearings and surpass conventional antifriction alloys like AO20-1, AO10S2, AO11S3, and bronze BrO4Ts4S17 in terms of performance [10]. A similar technology is used to produce an alloy containing Cu, Si, Zn, Mg, Ti, along with 5–11 % Sn and 2–4 % Pb. In addition to the slightly different chemical composition, this process also involves heat treatment – annealing the castings at 250–300 °C for 10–12 h. This treatment halts natural aging processes and improves both the antifriction and mechanical properties of monometallic sliding bearings [11]. However, a study [12] examining a similar Al–Cu–Si–Sn–Pb–Bi system as an antifriction alloy points out that adding more than 1 % lead and bismuth to aluminum alloys is impractical. During conventional melting and casting, there is a high risk of segregation of these elements, and their contribution to precipitation hardening through quenching and aging is insignificant. Based on this, the author of [13] recommends a base composition of Al–4 % Cu–5 % Si–6 % Sn, which offers comparable properties to expensive bronzes and should undergo the following heat treatment: holding at 500 °C for 6 h, quenching in water, and aging at 175 °C for 6 h. This treatment promotes spheroidization of the silicon phase, significantly improving both strength and wear resistance. Overall, the development of complexly alloyed materials is undoubtedly a promising direction. However, the high cost of tin and the ambiguous effect of lead and bismuth currently limit their widespread adoption.

A key trend in recent years in the production of antifriction materials is a new approach – the development of cast composite materials (CM) of this type, achieved by introducing or forming not only intermetallic phases but also ceramic phases within aluminum alloys [14–16]. Initially, silicon carbide was primarily used as the ceramic filler due to its low cost. However, studies revealed that at high temperatures and prolonged exposure, silicon carbide tends to degrade, forming undesirable phases [17]. As a result, titanium carbide has recently become the preferred filler. Firstly, titanium carbide exhibits the greatest similarity in lattice parameters to the face-centered cubic (FCC) aluminum matrix, ensuring good wettability and a modifying effect. Secondly, it is characterized by higher hardness, elastic modulus, and thermodynamic stability [18].

The first research efforts in this area in the Russian Federation were carried out using matrix alloys of the Al–Si system – the so-called silumins [19–23]. For example, in [24], antifriction composites were proposed based on AK12 and AK12M2MgN alloys, reinforced with intermetallic phases of the Al_3Me type (where Me = V, Ti, Cr, Hf, Zr, Sc), introduced ceramic particles of SiC or TiC, and modified with nanoscale additives (shungite, diamond (C), TiCN, etc.). It was found that composite materials containing 5 and 10 % TiC as the reinforcing phase demonstrate lower friction coefficients and reduced wear rates compared to materials reinforced with SiC.

The advantage of using titanium carbide as a reinforcing phase was also demonstrated in a later study [25], where ready-made ceramic particles of Al_2O_3, B_4C, SiC, or TiC were mechanically introduced into the melts of matrix alloys belonging to various alloying systems (Al–Si–Mg, Al–Si–Cu, Al–Mg, Al–Cu–Mg, Al–Sn–Cu, etc.). Two particle size groups were investigated: $d \leq 40$ μm and $d = 40–100$ μm. The resulting composites were then applied to steel surfaces using electric arc or plasma-powder cladding. Based on the comparison results, the authors concluded that the optimal filler is a composition with 10 % TiC and a particle size of 40–100 μm, as it provides the greatest increase in coating wear resistance – up to 10 times – and reduces the friction coefficient by 60 % compared to conventional antifriction alloys AO20-1 and B83.

Internationally, researchers are also actively developing antifriction composite materials by introducing titanium carbide into various aluminum alloys [26–30]. Reported concentrations range from as low as 0.07–0.18 vol. % [31] to more substantial levels of 5–15 wt. % [32; 33]. Studies indicate that reductions in wear rate and friction coefficient become more pronounced as the titanium carbide content increases. It is also reported that the improvement in wear resistance of CM in the presence of titanium carbide is retained

---

[1] Here and further in the text we mean wt. % unless otherwise stated.

at elevated temperatures of 150 and 200 °C [34]. The results of these studies have already been implemented in production. For example, the American company Martin Marietta successfully uses Al/TiC_p composites to manufacture engine pistons and connecting rods [35].

Most of the ongoing research and industrial production of composite materials reinforced with titanium carbide is currently carried out using the conventional and technologically simple method of mechanically introducing pre-synthesized particles into the melt. However, the practical implementation of this method is associated with several challenges. First, the wettability of particles by the melt largely depends on the stoichiometry of TiC_x, which has a wide stability range ($0.55 < C/Ti \leq 1$). As the carbon content x increases, wettability decreases. Therefore, introducing a stoichiometric compound with maximum mechanical properties requires a melt temperature of at least 1400 K [36]. Second, the introduction of highly dispersed titanium carbide particles poses a challenge. Despite their higher cost, such particles have a more pronounced effect [37; 38]. For example, study [39] demonstrated that the wear resistance of Al–5 % Cu alloys containing 0.5 % of nanosized TiC particles is 16.5 % higher than that of a composite with 5 % TiC particles of micron size at the same temperature. This substantial improvement in antifriction properties is explained by the fact that, in highly dispersed particles, the number of atoms in the surface layer is comparable to the number in the particle volume, leading to fundamentally new effects and activating different strengthening mechanisms [40; 41]. However, the mechanical introduction of highly dispersed titanium carbide particles into the melt is extremely difficult, as they tend to agglomerate and exhibit poor wettability [42; 43].

These challenges can be avoided by applying a fundamentally different technological approach, namely, forming a highly dispersed carbide phase directly in the melt using the Self-Propagating High-Temperature Synthesis (SHS) method. This involves initiating an exothermic reaction between the corresponding initial powder reagents in the heated matrix melt. Research in this area has been actively conducted by scientists in China [44–46], South Korea [47], India [48; 49], and other countries. However, the published results do not always confirm that the phase composition of the resulting materials, the amount of carbide phase, and the particle sizes meet the optimal levels required to ensure high antifriction properties.

At Samara State Technical University, intensive research has recently been carried out in this field. These efforts have led to the development of a technologically accessible method for producing composite materials, which includes four sequential stages [50; 51]:

1) heating the matrix alloy to 900 °C;

2) introducing an SHS charge into the melt, consisting of titanium and carbon powders taken in a stoichiometric ratio, as well as Na_2TiF_6 flux to facilitate the initiation of their exothermic interaction;

3) holding for 5 min to complete the chemical transformations, followed by melt stirring;

4) casting the composite material and its solidification.

The proposed technology features a lower melt temperature compared to mechanical mixing and a shorter process cycle, which already helps reduce production costs. Moreover, it guarantees the synthesis and uniform distribution of a highly dispersed titanium carbide phase that is fully wetted by the melt. This phase is produced directly from affordable industrial-grade titanium and carbon powders of micron size, which is also economically advantageous. The proposed method has been tested on aluminum alloys from the most common alloying systems (Al–Mg, Al–Cu, Al–Si), and it has been proven that stoichiometric titanium carbide with particle sizes ranging from 100 nm to 2 μm can be successfully synthesized in these melts. This made it possible to improve several mechanical and tribological properties of the developed composite materials [52; 53]. However, for further industrial implementation, it is necessary to consider the specific operating conditions of particular components and evaluate the required properties in combination. One of the most in-demand applications for antifriction materials is the production of cast engine pistons, which are currently made primarily from heat-resistant aluminum alloys such as AM4.5Kd and AK10M2N.

In this context, the objective of the present study was to comprehensively analyze the performance and processing characteristics of AM4.5Kd–10%TiC and AK10M2N–10%TiC composite materials produced via in-melt SHS to assess their feasibility for use as antifriction materials in engine piston manufacturing.

Materials and methods

The matrix melts were prepared using the casting alloys AM4.5Kd (GOST 1583–93) and AK10M2N (GOST 30620–98), produced by Sammet LLC, Russia. The charge mixture consisted of titanium powder (TPP-7, TU 1715-449-05785388) and carbon powder (P-701, GOST 7585–86), taken in a stoichiometric ratio to ensure the SHS reaction proceeds according to the equation: Ti + C = TiC. This mixture was combined with Na_2TiF_6 salt (GOST 10561–80), added in an amount of 5 % of the total charge weight. The prepared portions of the charge, wrapped in aluminum foil, were introduced into the melts of the specified alloys, heated to 900 °C in a graphite crucible placed in a PP-20/12 melting furnace (Russia). After the SHS reaction was completed and the melt was stirred, the melt containing TiC particles was cast into a metal mold to produce cast composite samples with a diameter of 20 mm and a height of approximately 150 mm. Cylindrical specimens with a diameter and height of 20 mm were then machined from these castings for further testing. All specimens underwent quenching and artificial aging to achieve maximum hardness, according to the following heat treatment conditions:

– AM4.5Kd: holding for 1 h at 545 °C, quenching, aging for 6 h at 170 °C (*HB* = 136);

– AM4.5Kd–10 % TiC: holding for 1 h at 545 °C, quenching, aging for 4 h at 170 °C (*HB* = 142);

– AK10M2N: holding for 2 h at 515 °C, quenching, aging for 2 h at 190 °C (*HB* = 152);

– AK10M2N–10 % TiC: holding for 1 h at 515 °C, quenching, aging for 2 h at 190 °C (*HB* = 171).

All heat treatment processes were performed in a SNOL laboratory chamber furnace (Russia) with a maximum operating temperature of 1300 °C.

The microstructures of the heat-treated composite materials are shown in Fig. 1. According to *X*-ray phase analysis, in addition to titanium carbide, the AM4.5Kd–10 % TiC specimen contains 2 % of the Al_2Cu phase, while the AK10M2N–10 % TiC specimen contains 2 % Al_2Cu, 1 % Al_3Ni, and 10 % Si.

Tribological tests were performed using the Universal-1B testing system (Russia) under a ring-on-flat configuration with a lubricating medium of GL-5 transmission oil.

The thermal linear expansion coefficient (TLEC) was determined using a mechanical dilatometer on rods with an initial length of 60 mm under the following conditions: test duration – 5 h, thermocouple – type K (Chromel-Alumel), temperature range – up to 300 °C, temperature step – 25 °C. TLEC values (α, K^{-1}) were calculated using the formula

$$\alpha = \frac{l_2 - l_1}{l_1 (t_2 - t_1)}, \qquad (1)$$

where t_1 and t_2 are the initial and final temperatures of the specimen, K; l_1 and l_2 are the corresponding specimen lengths at t_1 and t_2, mm.

Short-term high-temperature strength was evaluated by compression testing at temperatures of 150 °C and 250 °C using an Instron 8802 universal testing machine (USA) equipped with a 3119-406 thermal chamber, under a load of 100 kN and a crosshead speed of 1 mm/min.

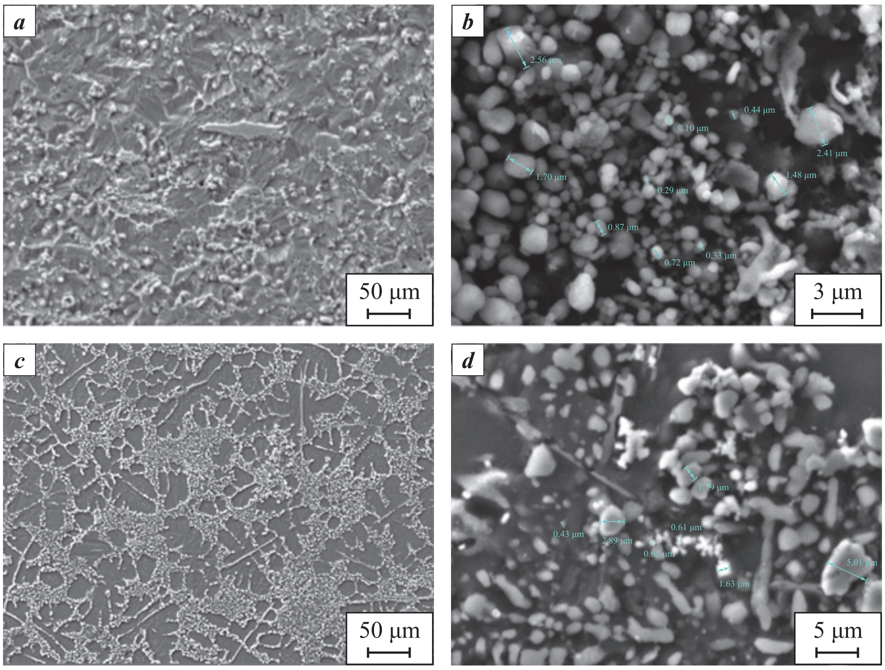

Fig. 1. Microstructures of composite materials AM4.5Kd–10 % TiC(***a***, ***b***) and AK10M2N–10 % TiC (***c***, ***d***)
a, ***c*** – magnification 500×, ***b*** – magnification 10,000×, ***d*** – magnification 5000×

Рис. 1. Микроструктуры композиционных материалов АМ4,5Кд–10 % TiC (***a***, ***b***) и АК10М2Н–10 % TiC (***c***, ***d***)
a, ***c*** – увеличение 500×, ***b*** – увеличение 10 000×, ***d*** – увеличение 5000×

Casting properties were evaluated using the Nekhendi–Kuptsov combined casting test mold. Melts of both the alloys and composite materials, heated to 710 °C, were poured into the preheated mold (200–250 °C). Fluidity was determined based on the height of the *U*-shaped cast bar. Linear shrinkage (ε_{lin}, %) was calculated using the formula

$$\varepsilon_{\text{lin}} = \frac{L_{\text{m}} - L_{\text{cast}}}{L_{\text{cast}}} \cdot 100\ \%, \qquad (2)$$

where L_{m} = 152 mm is thelength of the vertical cavity in the mold; L_{cast} is the actual length of the vertical cast bar measured at t = 20 °C, mm.

Results and discussion

The antifriction properties were investigated under conditions simulating the operating environment of the piston–piston pin friction pair in an internal combustion engine at a normal load of 400 N. The rotation speed of the counterbody was 600 rpm, and the test duration was 60 min or until complete seizure occurred.

The appearance of the friction surfaces of the base alloys and the corresponding composite materials after testing is shown in Fig. 2. Analysis of the surfaces of AM4.5Kd and AK10M2N alloys indicates the presence of seizure and abrasive wear, as well as the formation of deep grooves along the sliding direction. In contrast, the surfaces of the composite materials exhibited better conformability to the counterbody and the absence of pronounced scuff marks.

Further analysis of the friction force profiles confirmed that the presence of the titanium carbide phase significantly improved wear resistance. In the AM4.5Kd–10 % TiC composite, the wear rate decreased by a factor of 2.4, and the friction coefficient decreased by a factor of 2.7 compared to the matrix alloy. For AK10M2N–10 % TiC, the wear rate decreased by a factor of 17 and the friction coefficient decreased by a factor of 4. At the same time, the level of thermal self-heating during testing remained unchanged in both systems (Fig. 3).

To determine the maximum permissible load, scuff resistance tests were carried out under gradually

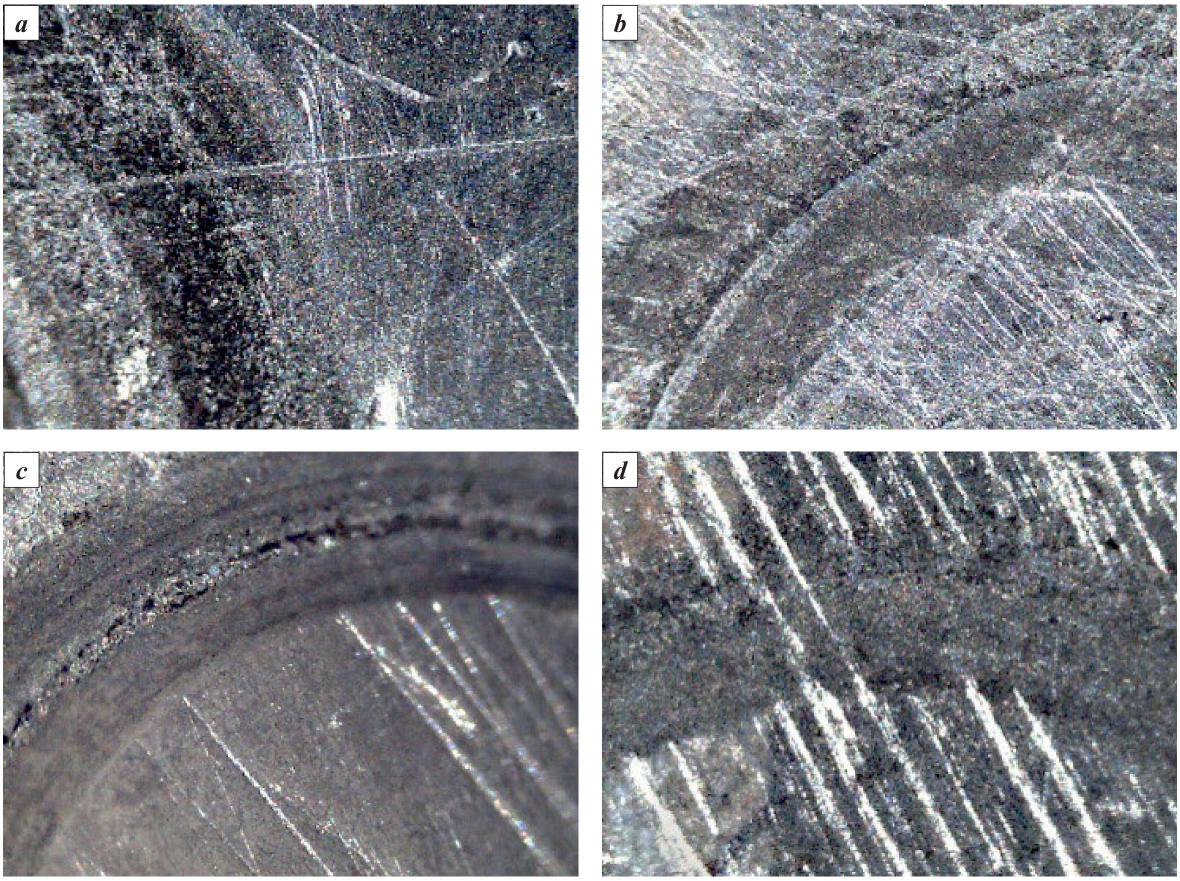

Fig. 2. Appearance of friction surfaces after testing ($100^{\times}$)
a – AM4.5Kd; ***b*** – AM4.5Kd–10 % TiC; ***c*** – AK10M2N; ***d*** – AK10M2N–10 % TiC

Рис. 2. Вид поверхностей трения после испытаний ($100^{\times}$)
a – АМ4,5Кд; ***b*** – АМ4,5Кд–10 % TiC; ***c*** – АК10М2Н; ***d*** – АК10М2Н–10 % TiC

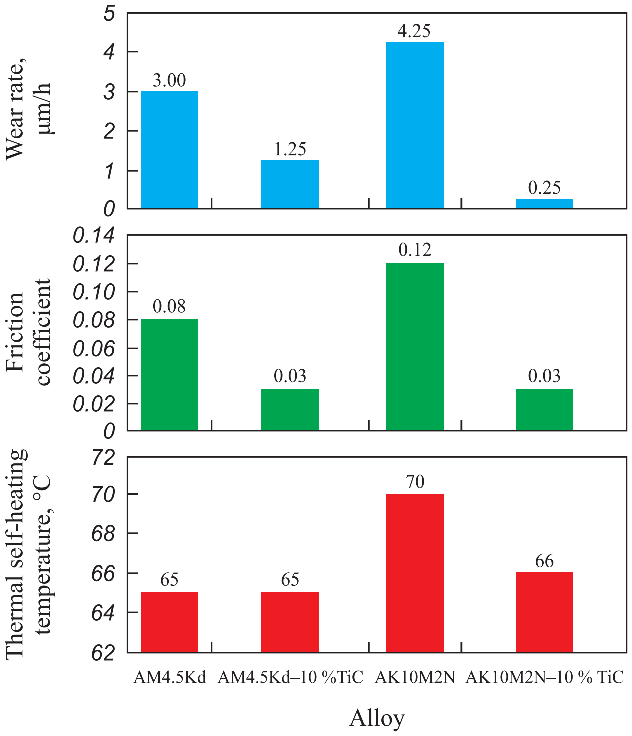

Fig. 3. Tribological characteristics of AM4.5Kd and AK10M2N alloys and the corresponding composite materials under a constant load of 400 N

Рис. 3. Трибологические характеристики сплавов АМ4,5Кд, АК10М2Н и композиционных материалов на их основе при постоянной нагрузке 400 Н

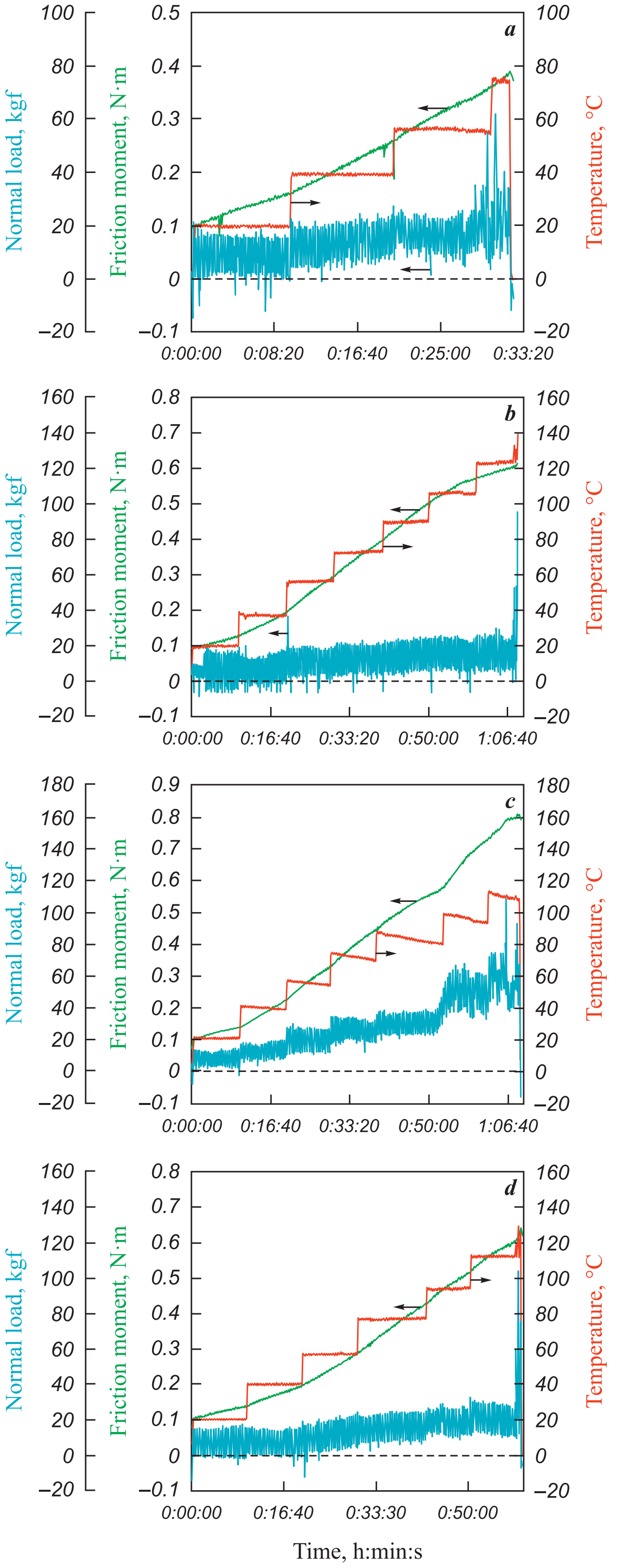

Fig. 4. Friction force profiles of specimens under increasing loads

a – AM4.5Kd; ***b*** – AM4.5Kd–10 % TiC;
c – AK10M2N; ***d*** – AK10M2N–10 % TiC

Рис. 4. Эпюры трибологических испытаний образцов при возрастающих нагрузках

a – АМ4,5Кд; ***b*** – АМ4,5Кд–10 % TiC;
c – АК10М2Н; ***d*** – АК10М2Н–10 % TiC

increasing load conditions. Each load stage lasted 10 min, with a load increment of 100 N, and the maximum applied load reached 1300 N. The results showed that seizure in AM4.5Kd occurred at a load of 700 N, while for the AM4.5Kd–10 % TiC composite, seizure was only observed at 1200 N – an increase by a factor of 1.7 (Fig. 4).

For the AK10M2N and AK10M2N–10 % TiC specimens, complete seizure occurred at the same load of 1100 N. However, for the matrix alloy, friction coefficient fluctuations were recorded at loads above 800 N, whereas the composite specimen maintained a stable friction coefficient up to the maximum load (see Fig. 4). These results confirm the enhanced scuff resistance of both composite materials.

In addition to antifriction properties, another critical performance characteristic for piston materials is the ability to maintain stable linear dimensions under heating [54]. Therefore, this study also evaluated the thermal linear expansion coefficients (TLEC) of both the base alloys and the composites at temperatures of 20 and 300 °C. The analysis of the results shown in Fig. 5 reveals a slight increase in TLEC with heating for all specimens. However, the thermal expansion of the composite materials in both systems remained close to that of the matrix alloys, confirming their comparable level of thermal stability. The obtained TLEC values are consistent with the data from [55], where a composite material based on Al–5 % Cu–0.8 % Mn reinforced with 5 % B_4C (particle size 5 μm) produced by mechanical mixing followed by pressure crystallization was investigated. Its TLEC was found to be $17.2 \cdot 10^{-6}$ K^{-1} in the 20–100 °C range and $19.8 \cdot 10^{-6}$ K^{-1} in the 20–200 °C range. That study also demonstrated that cyclic heating of the specimens did not affect the stability of these TLEC values.

The obtained data are highly significant, as it is known that the intrinsic thermal linear expansion coefficient (TLEC) of titanium carbide is higher than that of, for example, silicon carbide ($(6.52–7.15) \cdot 10^{-6}$ K^{-1} and $(4.63–4.7) \cdot 10^{-6}$ K^{-1}, respectively). This could have potentially had a negative effect on the TLEC of the composite. Moreover, study [56] showed that increasing the particle size of the SiC fraction from 50 to 320 μm reduced the TLEC of the Al–Mg–Cu–Si–65 vol. % SiC composite material by 15–20 %. The authors attributed this to the fact that smaller silicon carbide inclusions create a larger number of interphase boundaries with unstable structures, which facilitates thermal expansion. From this perspective, the highly dispersed particles in the developed composites should also form a very large number of interphase boundaries, which could theoretically result in a significant increase in TLEC. However, this effect is not observed. Apparently, this is due to the similarity between the lattice parameters of titanium carbide and the aluminum matrix, as well as the high quality of adhesive bonding at the interphase boundaries.

Since engine piston castings made from AM4.5Kd and AK10M2N alloys operate at elevated temperatures (up to 250 °C) under predominantly compressive stresses, another important functional characteristic – short-term high-temperature strength – was also studied. Compression tests were carried out at elevated temperatures under a load of up to 100 kN (Fig. 6). Compared to the base alloys, both composites showed slightly higher high-temperature strength at 20 and 150 °C, which can be explained by the refractory nature of the carbide phase. At 250 °C, the composites demonstrated strength comparable to the matrix alloys, which is associated with the onset of partial melting along the matrix grain boundaries.

In study [55], the temperature distribution in an operating engine piston was calculated, showing that the maximum piston temperature reaches 225 °C, with compressive stresses not exceeding 120 MPa. That same study also reported that the compressive strength of the Al–5 % Cu–0.8 % Mn–5 % B_4C composite at 260 °C is 149 MPa. Comparing these results shows that the composites containing 10 % TiC provide a significantly higher safety margin for high-temperature strength under operating conditions typical for engine pistons.

In addition to performance properties, the processing characteristics of AM4.5Kd- and AK10M2N-based composites are also critically important. The most relevant casting properties – fluidity and shrinkage – were evaluated using the Nekhendi–Kuptsov combined casting test mold (Fig. 7). During solidification, all specimens demonstrated high resistance to hot cracking. The composites of both systems also showed a general trend toward reduced linear shrinkage, which is presumably due to a slight increase in melt viscosity caused by the presence of carbide phase particles. At the same time, the high dispersity of these particles does not significantly hinder melt flow. As a result, the AM4.5Kd-based composites exhibited only a minor decrease in fluidity (>90 % of the matrix alloy's value),

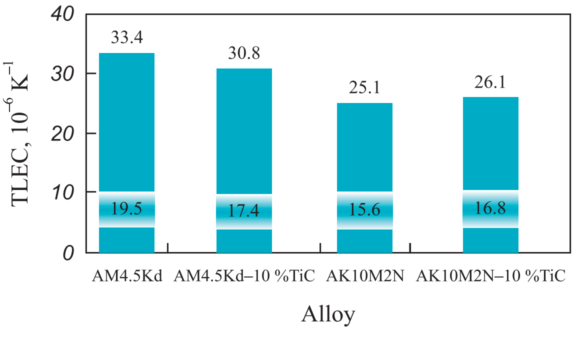

Fig. 5. TCLE of AM4.5Kd and AK10M2N alloys and the corresponding composite materials at temperatures of 20 °C (upper values) and 300 °C (lower values)

Рис. 5. ТКЛР сплавов АМ4,5Кд, АК10М2Н и композиционных материалов на их основе при температурах 20 °С (верхние значения) и 300 °С (нижние)

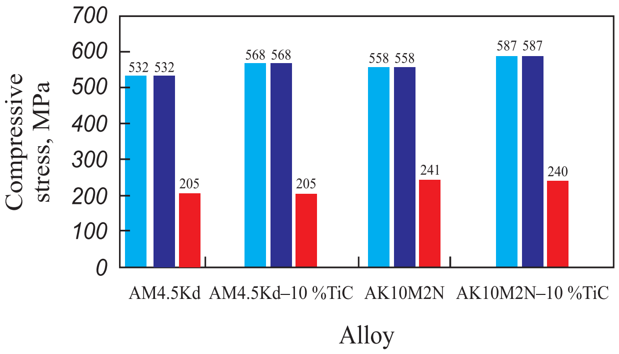

Fig. 6. Short-term high-temperature strength of AM4.5Kd and AK10M2N alloys and the corresponding composite materials

t, °C: 🟦 – 20, 🟦 – 150, 🟥 – 250

Рис. 6. Кратковременная жаропрочность сплавов АМ4,5Кд, АК10М2Н и композиционных материалов на их основе

t, °C: 🟦 – 20, 🟦 – 150, 🟥 – 250

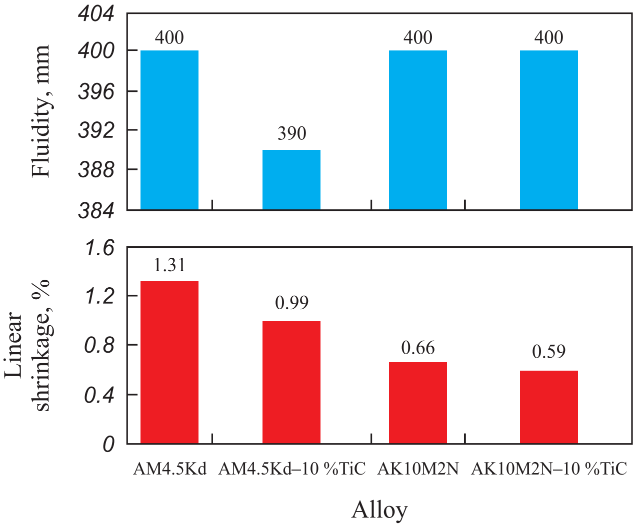

Fig. 7. Casting properties of AM4.5Kd and AK10M2N alloys and the corresponding composite materials

Рис. 7. Литейные свойства сплавов АМ4,5Кд, АК10М2Н и композиционных материалов на их основе

while the fluidity of the AK10M2N-based composites remained virtually unchanged.

It is generally assumed that the casting properties of composite materials deteriorate as the volume fraction of the carbide phase increases. However, study [17] examined the casting properties of AK9ch- and AK12MMgN-based composites containing 10–20 vol. % SiC, and it was found that at SiC contents of 10–15 vol. %, the composites retained high fluidity and lower linear shrinkage compared to the matrix alloys. Only at 20 vol. % SiC did fluidity decrease due to a sharp increase in melt viscosity. The high casting performance of composites containing titanium carbide particles can also be attributed to differences in TLEC. Titanium carbide has a thermal expansion coefficient that is an order of magnitude lower than aluminum ($(6.52–7.15)\cdot10^{-6}$ K^{-1} versus $2.4\cdot10^{-5}$ K^{-1}, respectively). Therefore, the presence of numerous highly dispersed block-shaped particles does not create significant resistance to melt flow, thus preserving adequate casting properties.

Conclusion

The comprehensive research conducted in this study demonstrated that synthesizing a highly dispersed titanium carbide phase directly in the melts of piston aluminum alloys AM4.5Kd and AK10M2N enables the production of new composite materials – AM4.5Kd–10 % TiC and AK10M2N–10 % TiC. These materials exhibit improved antifriction properties compared to the matrix alloys, while maintaining comparable thermal expansion during heating, high-temperature strength, and casting properties. These results provide grounds to recommend the developed composites for use in the production of cast engine pistons.

References / Список литературы

1. Bushe N.A., Dvoskina V.A., Rakov K.M., Gulyaev A.S. Bearings made of aluminum alloys. Moscow: Transport, 1974. 256 p. (In Russ.).

Буше Н.А., Двоскина В.А., Раков К.М., Гуляев А.С. Подшипники из алюминиевых сплавов. М.: Транспорт, 1974. 256 с.

2. Mironov A.E., Kotova (Karacharova) E.G. Development of new grades of cast aluminum antifriction alloys to replace bronze in friction units. *Izvestiya Samarskogo nauchnogo tsentra Rossiiskoi akademii nauk*. 2011;13(4); 1136–1140. (In Russ.).

Миронов А.Е., Котова (Карачарова) Е.Г. Разработка новых марок литейных алюминиевых антифрикционных сплавов для замены бронз в узлах трения. *Известия Самарского научного центра Российской академии наук*. 2011;13(4):1136–1140.

3. Menezes P.L., Ingole S.P., Nosonovsky M., Kailas S.V., Lovell M.R. Tribology for scientists and engineers. From basics to advanced concepts. NY: Springer, 2013. 948 p. https://doi.org/10.1007/978-1-4614-1945-7

4. Mironov A.E., Belov N.A., Stolyarova O.O. Aluminum alloys for antifriction purposes: Monograph. Moscow: MISIS, 2016. 222 p. (In Russ.).

Миронов А.Е., Белов Н.А., Столярова О.О. Алюминиевые сплавы антифрикционного назначения: Монография. М.: Изд. Дом МИСИС, 2016. 222 с.

5. Malikova E.V. Study of the possibility of modifying aluminum-tin alloy AO20-1. *Vestnik TGU*. 1997;2(3): 335–336. (In Russ.).

Маликова Е.В. Исследование возможности модифицирования алюминиево-оловянного сплава АО20-1. *Вестник ТГУ*. 1997;2(3):335–336.

6. Neuhaus P., Roth A., Steeg M. Antifriction alloy based on aluminum: Patent 1254 (Republic Kazakhstan). 1994. (In Russ.).

Нойхауз П., Рот А., Штеег М. Антифрикционный сплав на основе алюминия: Патент 1254 (Республика Казахстан). 1994.

7. Mironov A., Gershman I., Gershman E., Podrabinnik P., Kuznetsova E., Peretyagin P., Peretyagin N. Properties of journal bearing materials that determine their wear Resistance on the example of aluminum-based alloys. *Materials*. 202;14(3):535. https://doi.org/10.3390/ma14030535

8. Gershman I., Mironov A., Podrabinnik P., Kuznetsova E., Gershman E., Peretyagin P. Relationship of secondary structures and wear resistance of antifriction aluminum alloys for journal bearings from the point of view of self-organization during friction. *Entropy*. 2019;21(11):1048. https://doi.org/10.3390/e21111048

9. Mironov A.E., Antyukhin G.G., Gershman E.I., Podrabinnik P.A., Kuznetsova E.V., Peretyagin N.Yu. New antifriction aluminum alloys for cast monometallic plain bearings. Bench tests. *Vestnik nauchno-*

issledovatel'skogo instituta zheleznodorozhnogo transporta. 2020;79(4):217–223. (In Russ.).
https://doi.org/10.21780/2223-9731-2020-79-4-217-223

Миронов А.Е., Антюхин Г.Г., Гершман Е.И., Подрабинник П.А., Кузнецова Е.В., Перетягин Н.Ю. Новые антифрикционные алюминиевые сплавы для литых монометаллических подшипников скольжения. Стендовые испытания. *Вестник научно-исследовательского института железнодорожного транспорта*. 2020;79(4):217–223.
https://doi.org/10.21780/2223-9731-2020-79-4-217-223

10. Mironov A.E., Gershman I.S., Ovechkin A.V., Kotova E.G., Koshelev M.A., Gershman E.I. Antifriction alloy based on aluminum and the method of its manufacture: Patent 2577876 (RF). 2016. (In Russ.).

Миронов А.Е., Гершман И.С., Овечкин А.В., Котова Е.Г., Кошелев М.А., Гершман Е.И. Антифрикционный сплав на основе алюминия и способ его изготовления: Патент 2577876 (РФ). 2016.

11. Mironov A.E., Gershman I.S., Gershman E.I. Casting antifriction alloy based on aluminum for monometallic plain bearings and the method of its manufacture: Patent 2571665 (RF). 2015. (In Russ.).

Миронов А.Е., Гершман И.С., Гершман Е.И. Литейный антифрикционный сплав на основе алюминия для монометаллических подшипников скольжения и способ его изготовления: Патент 2571665 (РФ). 2015.

12. Stolyarova O.O. Justification of the composition and structure of casting antifriction aluminum alloys alloyed with low-melting metals: Abstract of the Diss. Cand. Sci. (Eng.). Moscow: MISIS, 2016. 27 p. (In Russ.).

Столярова О.О. Обоснование состава и структуры литейных антифрикционных алюминиевых сплавов, легированных легкоплавкими металлами: Автореф. дис. … канд. техн. наук. М.: МИСИС, 2016. 27 с.

13. Stolyarova O.O., Muravyova T.I., Zagorsky D.L., Belov N.A. Microscopy in the study of the surface of antifriction multicomponent aluminum alloys. *Fizicheskaya mezomekhanika*. 2016;19(5):105–114. (In Russ.).

Столярова О.О., Муравьева Т.И., Загорский Д.Л., Белов Н.А. Микроскопия в исследовании поверхности антифрикционных многокомпонентных алюминиевых сплавов. *Физическая мезомеханика*. 2016;19(5):105–114.

14. Rohatgi P.K., Tabandeh-Khorshid M., Omrani E., Lovell M.R., Menezes P.L. Tribology of metal matrix composites. In: *Tribology for Scientists and Engineers*. NY: Springer, 2013. P. 233–268.
https://doi.org/10.1007/978-1-4614-1945-7_8

15. Wazeer A., Mukherjee A., Das A., Sengupta B., Mandal G., Sinha A. Mechanical properties of aluminium metal matrix composites: Advancements, opportunities and perspective. In: *Structural Composite Materials. Composites Science and Technology. Singapore*: Springer, 2024. P. 145–160. https://doi.org/10.1007/978-981-99-5982-2_9

16. Rao J.K., Madhusudhan R., Rao T.B. Recent progress in stir cast aluminum matrix hybrid composites: overview on processing, mechanical and tribological characteristics, and strengthening mechanisms. *Journal of Bio- and Tribo-Corrosion*. 2022;8:74.
https://doi.org/10.1007/s40735-022-00670-4

17. Aksenov A.A. Optimization of the composition and structure of composite materials on aluminum and copper bases, obtained by liquid-phase methods and mechanical alloying: Abstract of Dissertation of Dr. Sci. (Eng.). Moscow: MISIS, 2007. 51 p. (In Russ.).

Аксенов А.А. Оптимизация состава и структуры композиционных материалов на алюминиевой и медной основах, получаемых жидкофазными методами и механическим легированием: Автореф. дис. … докт. техн. наук. М: МИСИС, 2007. 51 с.

18. Pan S., Jin K., Wang T., Zhang Z., Zheng L., Umehara N. Metal matrix nanocomposites in tribology: Manufacturing, performance, and mechanisms. *Friction*. 2022;10: 1596–1634. https://doi.org/10.1007/s40544-021-0572-7

19. Kurganova Yu.A., Kolmakov A.G. Structural metal matrix composite materials: textbook. M.: MSTU im. N.E. Bauman, 2015. 141 p.

Курганова Ю.А., Колмаков А.Г. Конструкционные металломатричные композиционные материалы: учебное пособие. М.: Изд-во МГТУ им. Н. Э. Баумана, 2015. 141 с.

20. Prusov E.S., Panfilov A.A., Kechin V.A. Role of powder precursors in production of composite alloys using liquid-phase methods. *Russian Journal of Non-Ferrous Metals*. 2017;58(3):308–316.
http://doi.org/10.3103/S1067821217030154

Прусов Е.С., Панфилов А.А., Кечин В.А. Роль порошковых прекурсоров при получении композиционных сплавов жидкофазными методами. *Известия вузов. Порошковая металлургия и функциональные покрытия*. 2016;2:47–58.
http://doi.org/10.17073/1997-308X-2016-2-47-58

21. Prusov E.S., Deev V.B., Aborkin A.V., Ri E.K., Rakhuba E.M. Structural and morphological characteristics of the friction surfaces of in-situ cast aluminum matrix composites. *Journal of Surface Investigation*. 2021;15(6):1332–1337.
https://doi.org/10.1134/S1027451021060410

22. Mikheyev R.S., Chernyshova T.A. Aluminum-matrix composite materials with carbide hardening for solving problems of new technology. Moscow: RFFI, 2013. 353 p. (In Russ.).

Михеев Р.С., Чернышова Т.А. Алюмоматричные композиционные материалы с карбидным упрочнением для решения задач новой техники. М.: Изд. РФФИ, 2013. 353 с.

23. Mikheev R.S., Kobernik N.V., Kalashnikov I.E., Bolotova L.K., Kobeleva L.I. Tribological properties of antifriction coatings based on composite materials. *Perspektivnyye materialy*. 2015;3:48–54. (In Russ.).

Михеев Р.С., Коберник Н.В., Калашников И.Е., Болотова Л.К., Кобелева Л.И. Триботехнические свойства антифрикционных покрытий на основе композиционных материалов. *Перспективные материалы*. 2015;3:48–54.

24. Kalashnikov I.E. Development of methods for reinforcing and modifying the structure of aluminum-matrix composite materials: Abstract of the Dissertation of Dr. Sci. (Eng.). Moscow: A.A. Baikov Institute of Metallurgy of the Russian Academy of Sciences, 2011. 50 p. (In Russ.).

Калашников И.Е. Развитие методов армирования и модифицирования структуры алюмоматричных композиционных материалов: Автореф. дис. ... докт. техн. наук. М.: ИМЕТ им. А.А. Байкова РАН. 2011. 50 с.

25. Mikheev R.S. Promising coatings with improved tribotechnical characteristics made of composite materials based on non-ferrous alloys: Abstract of the Dissertation of Dr. Sci. (Eng.). Moscow: A.A. Baikov Institute of Metallurgy of the Russian Academy of Sciences, 2018. 45 p. (In Russ.).

Михеев Р.С. Перспективные покрытия с повышенными триботехническими характеристиками из композиционных материалов на основе цветных сплавов: Автореф. дис. … докт. техн. наук. М.: ИМЕТ им. А.А. Байкова РАН, 2018. 45 с.

26. Lakshmikanthan A., Angadi S., Malik V., Saxena K.K., Prakash C., Dixit S., Mohammed K.A. Mechanical and tribological properties of aluminum-based metal-matrix composites. *Materials*. 2022;15:6111. https://doi.org/10.3390/ma15176111

27. Samal P., Vundavilli P.R., Meher A., Mahapatra M.M. Recent progress in aluminum metal matrix composites: A review on processing, mechanical and wear properties. *Journal of Manufacturing Processes*. 2020;59:131–152. https://doi.org/10.1016/j.jmapro.2020.09.010

28. Kareem A., Qudeiri J.A., Abdudeen A., Ahammed T., Ziout A. A Review on A 6061 metal matrix composites produced by stir casting. *Materials*. 2021;14(1):175. https://doi.org/10.3390/ma14010175

29. Prasad C., Gali A. Microstructure, mechanical, and tribological properties of TiC- and Ni-reinforced AA6061 matrix composite fabricated through stir casting. *Transactions of the Indian Institute of Metals*. 2024;77:2625–2636. https://doi.org/10.1007/s12666-024-03345-5

30. Lekatou A., Karantzalis A.E., Evangelou A., Gousia V., Kaptay G., Gacsi Z., Baumali P., Simon A. Aluminium reinforced by WC and TiC nanoparticles (*ex-situ*) and aluminid particles (*in-situ*): Microstructure, wear and corrosion behavior. *Materials and Design*. 2015;65:1121–1135. https://doi.org/10.1016/j.matdes.2014.08.040

31. Tyagi R. Synthesis and tribological characterization of in situ cast Al–TiC composites. *Wear*. 2005;259(1-6): 569–576. https://doi.org/10.1016/j.wear.2005.01.051

32. Liu G., Amara A.A., Eskin D., McKay B. Manufacture of nano-to-submicron-scale TiC particulate reinforced aluminium composites by ultrasound-assisted stir casting. In: *Light Metals 2023. TMS 2023. The Minerals, Metals and Materials Series*. Springer, 2023. P. 339–348. https://doi.org/10.1007/978-3-031-22532-1_47

33. Venkateshwar Reddy P., Rajendra Prasad P., Mohana Krishnudu D., Venugopal Goud E. An investigation on mechanical and wear characteristics of Al 6063/TiC metal matrix composites using RSM. *Journal of Bio- and Tribo-Corrosion*. 2019;5:90. https://doi.org/10.1007/s40735-019-0282-0

34. Jerome S. Synthesis and evaluation of mechanical and high temperature tribological properties of in-situ Al–TiC composites. *Tribology International*. 2010;43(11):2029–2036. https://doi.org/10.1016/j.triboint.2010.05.007

35. Sethi V. Effect of aging on abrasive wear resistance of silicon carbide particulate reinforced aluminum matrix composite. USA: University of Cincinnaty, 2007. 114 p.

36. Froumin N., Frage N., Polak M., Dariel M.P. Wettability and phase formation in the TiC_x/Al system. *Scripta Materialia*. 1997;37(8):1263–1267. https://doi.org/10.1016/S1359-6462(97)00235-2

37. Yi G., Li H., Zang C., Xiao W., Ma C. Remarkable improvement in strength and ductility of Al–Cu foundry alloy by submicron-sized TiC particles. *Materials Science and Engineering: A*. 2022;885:143903. https://doi.org/10.1016/j.msea.2022.143903

38. Yang H., Tian S., Gao T., Nie J., You Z., Liu G., Wang H., Liu X.. High-temperature mechanical properties of 2024 Al matrix nanocomposite reinforced by TiC network architecture. *Materials Science and Engineering: A*. 2019;763:138121. https://doi.org/10.1016/j.msea.2019.138121

39. Tian W.S., Zhao Q.L., Zhao C.J., Qiu F., Jiang Q.C. The dry sliding wear properties of nano-sized TiC_p /Al–Cu composites at elevated temperatures. *Materials*. 2017; 10(8):939. https://doi.org/10.3390/ma10080939

40. Sanaty-Zadeh A. Comparison between current models for the strength of particulate-reinforced metal matrix nanocomposites with emphasis on consideration of Hall–Petch effect. *Material Science and Engineering: A*. 2012;531(1):112–118. https://doi.org/10.1016/J.MSEA.2011.10.043

41. Zhang Z., Chen D.L. Contribution of Orowan strengthening effect in particulate-reinforced metal matrix nanocomposites. *Material Science and Engineering: A*. 2008;483(15):148–152. https://doi.org/10.1016/j.msea.2006.10.184

42. Borgonovo C., Apelian D. Manufacture of aluminum nanocomposites: A critical review. *Material Science Forum*. 2011;678:1–22. https://doi.org/10.4028/www.scientific.net/MSF.678.1

43. Rana R.S., Purohit R., Das S. Review of recent studies in Al matrix composites. *International Journal of Scientific and Engineering Research*. 2012;2(6):1–16.

44. Li C., Yin Y., Cao G. Effect of TiC on microstructure and strength of Al–Bi–Cu alloys. *Journal. of Material Engineering and Perform*. 2022;31:524–533. https://doi.org/10.1007/s11665-021-06188-z

45. Tang P., Zhou Y., Lai J. Preparation, microstructure and mechanical properties of in-situ TiC/Al–Si–Fe aluminum matrix composites. *Transactions of the Indian Institute of Metals*. 2023;76:1893–1903. https://doi.org/10.1007/s12666-023-02885-6

46. Song M.S., Huang B., Zhang M.X., Li J.G. Study of formation behavior of TiC ceramic obtained by self-propagating high-temperature synthesis from Al–Ti–C elemental powders. *International Journal of Refractory Metals and Hard Materials*. 2009;27(3):584–589. https://doi.org/10.1016/j.ijrmhm.2008.09.009

47. Cho Y.H., Lee J.M., Kim S.H. Composites fabricated by a thermally activated reaction process in an Al melt using Al–Ti–C–CuO powder mixtures. Part I: Microstructural evolution and reaction mechanism. *Metallurgical and Ma-*

terials Transactions A. 2014;45(12):5667–5678.
https://doi.org/10.1007/s11661-014-2476-x

48. Lingaraju S.V., Hatti G., Jadhav M.R. Investigation on tribological behavior of Al7075-TiC/Graphene nano-composite using Taguchi method. *Journal of Bio- and Tribo-Corrosion*. 2024;10:110.
https://doi.org/10.1007/s40735-024-00908-3

49. Sujith S.V., Mahapatra M.M., Mulik R.S. An investigation into fabrication and characterization of direct reaction synthesized Al–7079–TiC in situ metal matrix composites. *Archives of Civil and Mechanical Ehgineering*. 2019;19(1):63–78.
https://doi.org/10.1016/j.acme.2018.09.002

50. Li P., Kandalova E.G., Nikitin V.I., Makarenko A.G., Luts A.R., Yanfei Zh. Preparation of Al–TiC composites by self-propagating high-temperature synthesis. *Scripta Materialia*. 2003;49(7):699–703.
https://doi.org/10.1016/S1359-6462(03)00402-0

51. Amosov A.P., Luts A.R., Latukhin E.I., Ermoshkin A.A. Application of SHS processes for *in situ* preparation of alumomatrix composite materials discretely reinforced by nanodimensional titanium carbide particles (review). *Russian Journal of Non-Ferrous Metals*. 2016;57(2):117–123.
https://doi.org/10.3103/S1067821216020024

Амосов А.П., Луц А.Р., Латухин Е.И., Ермошкин А.А. Применение процессов СВС для получения *in situ* алюмоматричных композиционных материалов, дискретно армированных наноразмерными частицами карбида титана: обзор. *Известия вузов. Цветная металлургия*. 2016;(1):39–49.
https://doi.org/10.17073/0021-3438-2016-1-39-49

52. Luts A.R., Sherina Yu.V., Amosov A.P., Kachura A.D. Liquid matrix SHS manufacturing and heat treatment of Al–Mg composites reinforced with fine titanium carbide. *Izvestiya. Non-Ferrous Metallurgy*. 2023;29(4):70–86.
https://doi.org/10.17073/0021-3438-2023-4-70-86

Луц А.Р., Шерина Ю.В., Амосов А.П., Качура А.Д. Жидкофазное получение методом СВС и термическая обработка композитов на основе алюминиево-магниевых сплавов, упрочненных высокодисперсной фазой карбида титана. *Известия вузов. Цветная металлургия*. 2023;29(4):70–86.
https://doi.org/10.17073/0021-3438-2023-4-70-86

53. Luts A.R., Sherina Yu.V., Amosov A.P., Minakov E.A., Ibatullin I.D. Selection of heat treatment and its impact on the structure and properties of AK10M2N–10%TiC composite material obtained via SHS method in the melt. *Izvestiya. Non-Ferrous Metallurgy*. 2024;30(2):30–43.
https://doi.org/10.17073/0021-3438-2024-2-30-43

Луц А.Р., Шерина Ю.В., Амосов А.П., Минаков Е.А., Ибатуллин И.Д. Выбор термической обработки и исследование ее влияния на структуру и свойства композиционного материала АК10М2Н–10%TiC, полученного методом СВС в расплаве. *Известия вузов. Цветная металлургия*. 2024;30(2):30–43.
https://doi.org/10.17073/0021-3438-2024-2-30-43

54. Nikitin K.V., Nikitin V.I., Timoshkin I.Yu. The influence of modifiers on the change in the mechanical properties of silumins. *Izvestiya. Non-Ferrous Metallurgy*. 2017;3: 72–76. (In Russ.).
https://doi.org/10.17073/0021-3438-2017-3-72-76

Никитин К.В., Никитин В.И., Тимошкин И.Ю. Влияние модификаторов на изменение механических свойств силуминов. *Известия вузов. Цветная металлургия*. 2017;(3):72–76.
https://doi.org/10.17073/0021-3438-2017-3-72-76

55. Mostafa Ahmed Lotfi Mohammed. Structure and properties of aluminum-based composites with a low coefficient of thermal expansion: Abstract of the Diss. Cand. Sci. (Eng.). Moscow: MISIS, 2018. (In Russ.).

Мостафа Ахмед Лотфи Мохаммед. Структура и свойства композитов на основе алюминия с низким коэффициентом термического расширения: Автореф. дис. … канд. техн. наук. М.: МИСИС, 2018.

56. Nyafkin A.N., Shavnev A.A., Kurbatkina E.I., Kosolapov D.V. Study of the influence of silicon carbide particle size on the temperature coefficient of linear expansion of a composite material based on an aluminum alloy. *Trudy VIAM*. 2020;86:41–49. (In Russ.).
https://doi.org/10.18577/2307-6046-2020-0-2-41-49

Няфкин А.Н., Шавнев А.А., Курбаткина Е.И., Косолапов Д.В. Исследование влияния размера частиц карбида кремния на температурный коэффициент линейного расширения композиционного материала на основе алюминиевого сплава. *Труды ВИАМ*. 2020;86:41–49.
https://doi.org/10.18577/2307-6046-2020-0-2-41-49

Information about the Author

Alfiya R. Luts – Cand. Sci. (Eng.), Assistent Professor of the Department of Metal Science, Powder Metallurgy, Nanomaterials, Samara State Technical University
ORCID: 0000-0001-7889-9931
E-mail: alya_luts@mail.ru

Сведения об авторе

Альфия Расимовна Луц – к.т.н., доцент кафедры «Металловедение, порошковая металлургия, наноматериалы», Самарский государственный технический университет
ORCID: 0000-0001-7889-9931
E-mail: alya_luts@mail.ru

Received 18.12.2024
Revised 10.01.2025
Accepted 17.01.2025

Статья поступила 18.12.2024 г.
Доработана 10.01.2025 г.
Принята к публикации 17.01.2025 г.

Refractory, Ceramic, and Composite Materials
Тугоплавкие, керамические и композиционные материалы

UDC 621.762

https://doi.org/10.17073/1997-308X-2025-2-51-61

Research article
Научная статья

Grain contiguity of tungsten carbide and hardness of nanostructured and ultrafine-grained WC–(Co)–VC–Cr_3C_2 cemented carbides fabricated by spark plasma and liquid phase sintering

M. I. Dvornik[1], E. A. Mikhailenko[1] ✉, O. O. Shichalin[2],
I. Yu. Buravlev[2], A. A. Burkov[1], N. M. Vlasova[1],
E. V. Chernyakov[1], V. K. Khe[1], P. G. Chigrin[1]

[1] **Khabarovsk Federal Research Center of the Far Eastern Branch**
of the Russian Academy of Sciences
153 Tikhookeanskaya Str., Khabarovsk 680042, Russia
[2] **Far Eastern Federal University**
10 Ajax Bay, Russky Island Vladivostok 690922, Russia

✉ mea80@list.ru

Abstract. This study investigates the dependencies between contiguity and hardness in nanostructured and ultrafine-grained tungsten-cobalt cemented carbides and tungsten carbide samples fabricated using spark plasma sintering (SPS) and liquid phase sintering (LPS). The main microstructural parameters were determined: average WC grain size, grain contiguity, and mean free path in cobalt. The average WC grain size in tungsten-cobalt cemented carbides produced by spark plasma sintering does not exceed 0.2 µm, classifying them as nanostructured materials. In cemented carbides obtained by liquid phase sintering and tungsten carbide fabricated using spark plasma sintering, the average WC grain size ranges from 0.2 to 0.5 µm, which corresponds to ultrafine-grained materials. The applicability of existing models developed for medium- and fine-grained cemented carbides was analyzed to describe the dependencies of contiguity on the cobalt volume fraction in the obtained ultrafine-grained and nanostructured materials. It was found that an exponential dependence adequately describes this relationship for the samples sintered in this study. The applicability of the theoretical hardness dependence on key microstructural parameters was also analyzed. The hardness of the obtained alloys was lower than predicted by the theoretical dependence based on the Hall–Petch law. The highest hardness ($HV = 2260 \pm 30$) among all the samples was observed in the nanostructured WC–5Co–0.4VC–0.4Cr_3C_2 alloy produced by spark plasma sintering. The hardness of ultrafine-grained sintered tungsten carbide was slightly lower ($HV = 2250 \pm 20$).

Keywords: nanostructured cemented carbide, tungsten carbide, spark plasma sintering, liquid phase sintering, hardness, grain contiguity

Acknowledgements: This study was carried out within the framework of the state assignment of the KhFRC FEB RAS.

For citation: Dvornik M.I., Mikhailenko E.A., Shichalin O.O., Buravlev I.Yu., Burkov A.A., Vlasova N.M., Chernyakov E.V., Khe V.K., Chigrin P.G. Grain contiguity of tungsten carbide and hardness of nanostructured and ultrafine-grained WC–(Co)–VC–Cr_3C_2 cemented carbides fabricated by spark plasma and liquid phase sintering. *Powder Metallurgy and Functional Coatings*. 2025; 19(2):51–61. https://doi.org/10.17073/1997-308X-2025-2-51-61

Смежность зерен карбида вольфрама и твердость наноструктурных и ультрамелкозернистых твердых сплавов WC–(Co)–VC–Cr$_3$C$_2$, полученных искровым плазменным и жидкофазным спеканием

М. И. Дворник[1], Е. А. Михайленко[1] ✉, О. О. Шичалин[2], И. Ю. Буравлев[2], А. А. Бурков[1], Н. М. Власова[1], Е. В. Черняков[1], В. К. Хе[1], П. Г. Чигрин[1]

[1] **Хабаровский федеральный исследовательский центр Дальневосточного отделения Российской академии наук**
Россия, 680042, г. Хабаровск, ул. Тихоокеанская, 153
[2] **Дальневосточный федеральный университет**
Россия, 690922, г. Владивосток, о. Русский, п. Аякс, 10

✉ mea80@list.ru

Аннотация. Проведено исследование зависимостей смежности и твердости образцов наноструктурных и ультрамелкозернистых вольфрамокобальтовых твердых сплавов и карбида вольфрама, полученных методами искрового плазменного и жидкофазного спекания. Определены основные параметры микроструктуры: средний диаметр зерен WC, смежность зерна, средняя длина свободного пути в кобальте. Установлено, что средняя величина зерен WC в вольфрамокобальтовых металлокерамических твердых сплавах, полученных искровым плазменным спеканием, не превышает 0,2 мкм, поэтому их можно отнести к наноструктурным. Средний диаметр зерен WC в твердых сплавах, полученных жидкофазным или искровым плазменным спеканием, находится в пределах от 0,2 до 0,5 мкм, что позволяет классифицировать эти материалы как ультрамелкозернистые. Проанализирована пригодность существующих моделей, разработанных для средне- и мелкозернистых твердых сплавов, для описания зависимости смежности от объемной доли кобальта в полученных ультрамелкозернистых и наноструктурных материалах. Определено, что для спеченных в данной работе образцов подходит экспоненциальная зависимость. Проведен анализ применимости теоретической зависимости твердости от основных параметров микроструктуры. Твердость получаемых сплавов оказалась ниже, чем это предсказывает теоретическая закономерность, основанная на соотношении Холла–Петча. Наибольшей твердостью ($HV = 2260 \pm 30$) из всех полученных образцов обладает наноструктурный сплав состава WC–5Co–0,4VC–0,4Cr$_3$C$_2$, полученный искровым плазменным спеканием. Твердость ультрамелкозернистого спеченного карбида вольфрама оказалась немного ниже ($HV = 2250 \pm 20$).

Ключевые слова: наноструктурный твердый сплав, карбид вольфрама, жидкофазное спекание (ЖФС), искровое плазменное спекание (ИПС), твердость, смежность зерен

Благодарности: Работа выполнена в рамках государственного задания ХФИЦ ДВО РАН.

Для цитирования: Дворник М.И., Михайленко Е.А., Шичалин О.О., Буравлев И. Ю., Бурков А.А., Власова Н.М., Черняков Е.В., Хе В.К., Чигрин П.Г. Смежность зерен карбида вольфрама и твердость наноструктурных и ультрамелкозернистых твердых сплавов WC–(Co)–VC–Cr$_3$C$_2$, полученных искровым плазменным и жидкофазным спеканием. *Известия вузов. Порошковая металлургия и функциональные покрытия*. 2025;19(2):51–61. https://doi.org/10.17073/1997-308X-2025-2-51-61

Introduction

Tungsten-cobalt cemented carbides (WC–Co) are the most widely used tool materials in the industry for cutting applications due to their combination of hardness, strength, heat resistance, oxidation resistance, and wear resistance. The microstructure of cemented carbides is primarily characterized by the cobalt phase volume fraction (V_{Co}) and the average WC grain size (d). In industrial practice, the most commonly used materials include medium-grained (MG) ($d = 1.3$–2.5 μm), fine-grained (FG) ($d = 0.8$–1.3 μm), and submicron-grained (SM) ($d = 0.5$–0.8 μm) cemented carbides. Further improvement in the operational durability of cemented carbides, which significantly depends on their hardness, remains an important task. Hardness can be increased either by reducing the cobalt content or by decreasing the average WC grain size. The latter approach is considered more promising, as it allows increasing hardness without a significant reduction in fracture toughness.

In recent decades, ultrafine-grained (UFG) cemented carbides with grain sizes reduced to 0.2–0.5 μm have gained widespread attention, offering enhanced hardness and wear resistance. Additionally, recent years have seen intensive research into the fabrication of nanostructured (NS) cemented carbides, in which the average WC grain size does not exceed 0.2 μm. It has been confirmed that these materials demonstrate high hardness, with values reported as $HV = 1941$ [1; 2], 1620 [3], 2356 [4], 1836 [5], and 2100 [6], resulting in improved wear resistance under abrasive wear [7] and cutting conditions. This has already led to their increasing production and application as tool and wear-resistant materials in industry. Further progress in this field requires the development of models capable of accurately describing the structure and properties of UFG and NS cemented carbides.

The main challenge in sintering such materials is grain growth caused by high temperature and prolonged sintering times. Previous studies have shown that UFG cemented carbides can be fabricated via liquid phase sintering (LPS) in vacuum [1–3; 7] or under pressure [8], using grain growth inhibitors (VC, Cr_3C_2, etc.). However, these conditions are insufficient to produce nanostructured cemented carbides. In recent years, researchers have increasingly employed spark plasma sintering (SPS) [4; 9–11] for the fabrication of nanostructured and ultrafine-grained cemented carbides. During SPS, powder consolidation occurs under the action of pulsed electric currents and discharge plasma generated by spark discharges between powder particles. This process strongly enhances diffusion-controlled densification, significantly reducing the sintering time and preventing grain growth.

Maximizing hardness by reducing the cobalt content has also led to the development of sintered WC [12–16], which can only be densified to a sufficient density (>99 %) under applied pressure. SPS technology is the most effective method for producing sintered WC, as it combines the application of pressure with rapid heating, both of which help prevent excessive grain growth.

A large number of studies have investigated the microstructure and mechanical properties (primarily hardness) of UFG and NS cemented carbides, as well as sintered tungsten carbide. One of the key microstructural characteristics in these studies is contiguity, which quantifies the fraction of the specific WC grain surface area involved in WC/WC grain contacts [17]:

$$C = \frac{S_{\mathrm{WC/WC}}}{S_{\mathrm{WC/WC}} + S_{\mathrm{WC/Co}}}, \qquad (1)$$

where $S_{\mathrm{WC/WC}}$ and $S_{\mathrm{WC/Co}}$ denote the interfacial areas of WC/WC and WC/Co grain boundaries, respectively.

Contiguity affects the mean free path (λ) in the cobalt binder, hardness, fracture toughness, and other properties. Numerous empirical and theoretical dependencies describe the dependence of contiguity on the cobalt volume fraction in conventional tungsten-cobalt cemented carbides [4; 7; 10; 11]. However, the applicability of these dependencies to ultrafine-grained and nanostructured cemented carbides has not been confirmed.

Several models have been developed to describe the relationships between key microstructural parameters (d, V_{Co}, C and λ) and hardness in medium-grained, fine-grained, and submicron-grained cemented carbides. Currently, there is particular interest in investigating the applicability of the dependence of hardness on key microstructural parameters [18–20] for describing the hardness of UFG and NS cemented carbides, as well as sintered tungsten carbide.

The aim of this study was to analyze the dependencies between contiguity and hardness and the microstructural parameters in UFG and NS tungsten-cobalt cemented carbides produced by liquid phase sintering and spark plasma sintering.

Materials and methods

Three nanostructured tungsten-cobalt cemented carbide samples containing 4, 5, and 10 %[1] cobalt, as well as one sintered tungsten carbide (WC) sample, were fabricated using the powder metallurgy method via spark plasma sintering (SPS). Additionally, four UFG cemented carbide samples containing 6, 8, 10, and 15 % cobalt were produced using LPS technique. In cemented carbides obtained by LPS, the cobalt content must be at least 6 %, as lower cobalt concentrations make it difficult to achieve sufficient density while simultaneously limiting grain growth.

All materials were produced using nanosized tungsten carbide powder (Hongwu, China, $d = 80–100$ nm, purity 99.95 %) and cobalt powder (grade PK-1, Russia, GOST 9721–79, $d = 1–30$ μm) (Fig. 1). To suppress WC grain growth, chemically pure vanadium carbide (VC) and chromium carbide (Cr_3C_2) powders, supplied by Reohim (Russia), were added to the powder mixtures as grain growth inhibitors.

The powder mixtures (Table 1), each weighing 50 g, were prepared by mixing for 1 h in a PM-400 planetary ball mill (Retsch, Germany) at a rotation speed of 250 rpm, with a ball-to-powder mass ratio of 10:1, followed by drying at 100 °C. Prior to SPS, cylindrical compacts were pre-pressed from each powder mixture (mixtures *1–4*) under a pressure of 20 MPa. For mixtures 5–8, a 10 % rubber solution in gasoline was added

---

[1] Here and throughout the text, weight percent (wt. %) is implied unless otherwise stated.

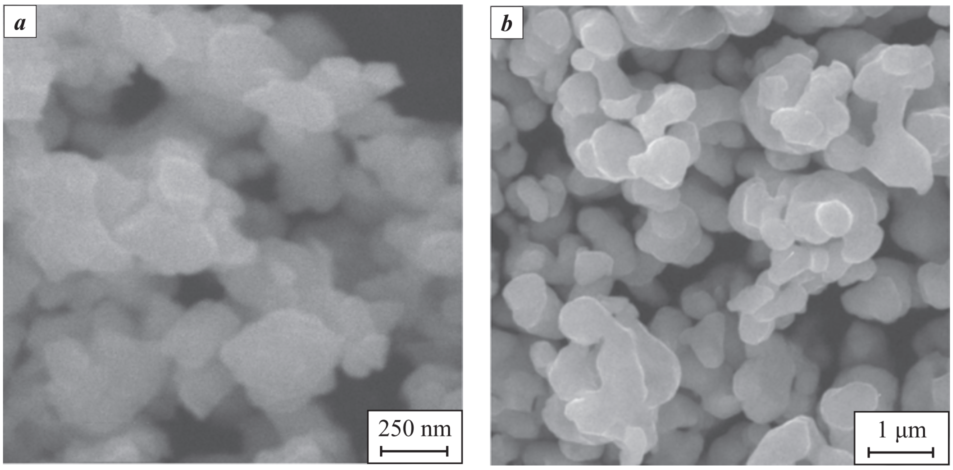

Fig. 1. Images of the initial commercial powders: tungsten carbide (***a***) and cobalt (***b***), used for the fabrication of sintered tungsten carbide and cemented carbide

Рис. 1. Фотографии исходных коммерческих порошков карбида вольфрама (***a***) и кобальта (***b***), использованных для получения спеченного карбида вольфрама и твердого сплава

as a plasticizer, in an amount ensuring that the granules prepared for pressing contained 1 % rubber after drying. After secondary drying to remove gasoline, four compacts were pressed from each powder mixture, with dimensions of 24×8×8 mm and a mass of 12 g.

Mixtures *1–4* were sintered using SPS in a graphite cylindrical die with an inner diameter of 10.5 mm on an SPS-515S system (Dr. Sinter LAB, Japan), under aconstant pressure of 57.3 MPa and a heating rate of 87.5 °C/min. To achieve the highest density, the cemented carbide samples were held at the maximum sintering temperature of 1200 °C for 5 min, while the tungsten carbide samples were held at $t_{max} = 2000$ °C for 10 min. The temperature and dwell time were selected based on previous experience with spark plasma sintering of nanostructured cemented carbides [5; 10; 15], aiming to prevent WC grain growth and avoid cobalt extrusion from the samples under applied pressure. The sintering parameters for tungsten carbide were taken from [15] to ensure the highest possible density. The compacts obtained from mixtures *5–8* underwent liquid phase sintering in a Carbolite STF vacuum furnace (Carbolite Gero, UK) at $t_{max} = 1450$ °C for 1 h to achieve high density, following the recommendations in [1–3; 7]. The compositions of the fabricated samples, sintering techniques, and maximum sintering temperatures are presented in Table 1. The cobalt volume fraction (V_{Co}) in the microstructure of tungsten-cobalt cemented carbides was calculated using the known densities of tungsten carbide (15.65 g/cm^3) and cobalt (8.7 g/cm^3), taking into account the mass concentrations of the components (see Table 1).

The density of the samples was measured by hydrostatic weighing using Vibra scales (Shinko, Japan). The surfaces of the sintered samples were ground and

Table 1. **Compositions of cemented carbide samples, cobalt volume fraction, and maximum sintering temperature**

Таблица 1. **Составы образцов твердых сплавов, объемная доля кобальта и максимальная температура спекания**

Mixture No.	Sample designation	Component content, wt. %				V_{Co}, vol. %	Sintering method	t_{max}, °C
		WC	Co	Cr_3C_2	VC			
1	WC–4Co–0.4VC–0.4Cr_3C_2	95.2	4.0	0.4	0.4	7.6	SPS	1200
2	WC–5Co–0.4VC–0.4Cr_3C_2	94.2	5.0	0.4	0.4	8.4	SPS	1200
3	WC–10Co–0.4VC–0.4Cr_3C_2	89.2	10.0	0.4	0.4	16.3	SPS	1200
4	WC–0.4VC–0.4Cr_3C_2	100.0	0	0.4	0.4	0	SPS	2000
5	WC–6Co–0.4VC–0.4Cr_3C_2	93.2	6.0	0.4	0.4	10.0	LPS	1450
6	WC–8Co–0.4VC–0.4Cr_3C_2	91.2	8.0	0.4	0.4	13.2	LPS	1450
7	WC–10Co–0.4VC–0.4Cr_3C_2	89.2	10.0	0.4	0.4	16.3	LPS	1450
8	WC–15Co–0.4VC–0.4Cr_3C_2	84.2	15.0	0.4	0.4	23.6	LPS	1450

polished for further microstructural analysis using a Vega scanning electron microscope (Tescan Orsay Holding, Czech Republic). WC grain boundaries were revealed by etching according to Standard Method 3 of ASTM B657-92. The etchant consisted of equal parts (by weight) of 10 % potassium ferricyanide and 10 % sodium hydroxide solutions. The average WC grain size (d) and the mean free path in cobalt (λ) were determined using the linear intercept method in accordance with ASTM E112-24. The experimental WC grain contiguity was determined using the intercept method according to the formula

$$C = \frac{N_{\mathrm{WC/WC}}}{N_{\mathrm{WC/WC}} + N_{\mathrm{WC/Co}}}, \qquad (2)$$

where $N_{\mathrm{WC/WC}}$ and $N_{\mathrm{WC/Co}}$ are the numbers of intersections of a random test line with WC/WC and WC/Co grain boundaries, respectively.

Equations (1) and (2) are equivalent [2]. The hardness of the samples was measured using an HVS-50 hardness tester (Time Group Inc., China) under a load of 30 kgf.

Results and discussions

Fig. 2 presents the microstructures of materials fabricated using spark plasma sintering and liquid phase sintering. The density of the sintered cemented carbides (Fig. 2, samples *1*–*3*) increases from 98.4 to 99.5 % as the cobalt content rises from 4 to 10 wt. %, which is attributed to the higher plasticity of cobalt (Fig. 3). Further increasing the density by raising the SPS temperature above 1200 °C is limited by the need to prevent grain growth and the extrusion of the cobalt phase from the samples. The use of a relatively low sintering temperature and the addition of grain growth inhibitors made it possible to limit the grain size to 0.17–0.19 μm (samples *1*–*3*, Table 2). Therefore, all tungsten-cobalt cemented carbide samples sintered by SPS can be classified as nanostructured. In these samples, the grain faceting is not pronounced, since grain growth was insufficiently intensive.

The relative density of tungsten carbide produced by SPS reached 99.9 %, which is ensured by the high sintering temperature (2000 °C) and prolonged holding time (Table 2). The resulting WC is classified as an ultrafine-grained material, as its average grain size does not exceed 0.5 μm (see Fig. 2, sample *4*), despite the presence of grain growth inhibitors.

The maximum temperature and holding time during LPS are limited only by grain growth. An increase in cobalt concentration from 6 to 15 % leads to a rise in the density of all fabricated samples (see Fig. 3, Table 2). During LPS, intense grain growth occurs through recrystallization via the liquid phase. As a result, the average WC grain size in samples *5*–*8* is significantly larger than that in the SPS-processed samples (Fig. 2, samples *1*–*4*). The tungsten carbide grains in these alloys acquire a characteristic faceted shape.

It can be expected that the contiguity values of materials obtained by SPS and LPS in vacuum will also deviate from existing empirical relationships [4; 7;

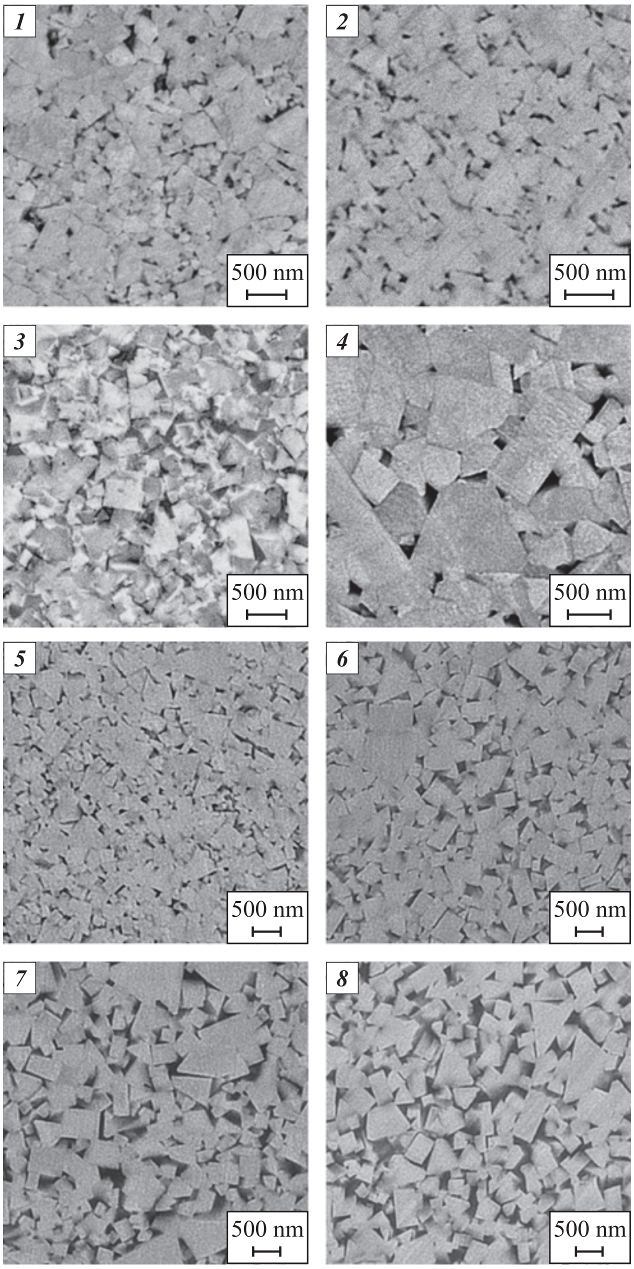

Fig. 2. Microstructures of the samples fabricated using spark plasma sintering (***1***–***4***) and liquid phase sintering vacuum (***5***–***8***)

Рис. 2. Микроструктуры образцов, полученных методом ИПС (***1***–***4***) и по технологии ЖФС в вакууме (***5***–***8***)

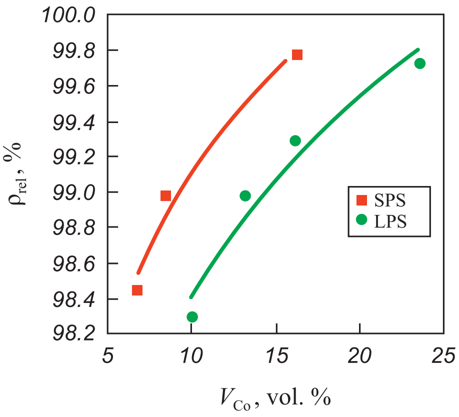

Fig. 3. Dependence of the relative density of sintered samples on the cobalt volume fraction

Рис. 3. Зависимость относительной плотности спеченных образцов от объемной доли кобальта

10; 11]. To describe contiguity, the authors of [21] proposed using exponential and power-law dependencies:

$$C = 1.03e^{-5V_{Co}}, \tag{3}$$

$$C = 0.074V_{Co}^{-1}. \tag{4}$$

In [22], linear and power-law dependencies were presented:

$$C = 0.85 - 1.8V_{Co}, \tag{5}$$

$$C = 0.2V_{Co}^{-0.45}. \tag{6}$$

The authors of [17] described the results of contiguity measurements using a scanning electron microscope, employing a power-law relationship:

$$C = 1 - 1.43V_{Co}^{0.63}. \tag{7}$$

The authors of [23] proposed an additional exponential dependence and a quadratic function-based equation to describe contiguity in their experimental data [23]:

$$C = e^{-8.4V_{Co}}, \tag{8}$$

$$C \cong 1 - \frac{V_{Co}}{\left(1 - V_{Co}\right)\left(5.975V_{Co}^2 - 0.691V_{Co} + 0.214\right)}. \tag{9}$$

Fig. 4 presents the experimental contiguity values of the obtained materials alongside the theoretical relationships (3)–(9). For each equation, the coefficient of determination was calculated to assess the deviation of the experimental data from the theoretical predictions. It can be observed that the relationships (3), (5), (6), and (7) provide the best fit, with determination coefficients in the range of 0.75–0.89, which is significantly higher than the threshold value (0.5), and are superior to the remaining equations (4), (8), and (9). This may be attributed to the fact that the contiguity

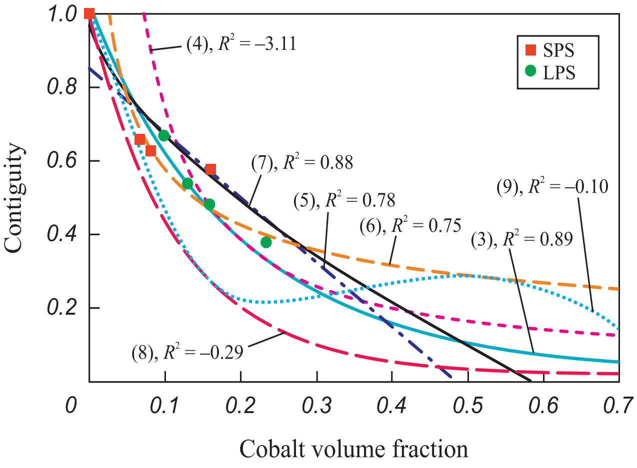

Fig. 4. Dependence of the experimental contiguity values on the cobalt volume fraction in the microstructure of ultrafine-grained cemented carbide fabricated using SPS and LPS in this study

Рис. 4. Зависимость экспериментальных значений смежности от объемной доли кобальта в микроструктуре исследуемых ультрамелкозернистых твердых сплавов, полученных методами ИПС и ЖФС в данном исследовании

Table 2. **Characteristics of the sintered samples**

Таблица 2. **Характеристики спеченных образцов**

Sample No.	ρ_{rel}, %	d_{WC}, μm	λ, μm	C	HV	K_{1c}, MPa·m$^{1/2}$
1	98.4	0.19	0.06	0.60	2160 ± 10	10.6 ± 0.2
2	99.0	0.17	0.11	0.57	2260 ± 30	11.0 ± 0.4
3	99.9	0.19	0.16	0.47	1850 ± 20	15.0 ± 0.6
4	99.9	0.50	0	1.00	2250 ± 20	9.1 ± 0.3
5	98.3	0.25	0.08	0.68	1870 ± 40	8.6 ± 1.0
6	99.0	0.24	0.14	0.46	1920 ± 20	9.7 ± 0.4
7	99.4	0.29	0.12	0.42	1880 ± 30	10.4 ± 0.7
8	99.9	0.28	0.12	0.16	1610 ± 20	12.1 ± 1.6

of WC grains in UFG and NS cemented carbides is higher than in conventional cemented carbides. A possible reason for this is that cobalt atoms are not always able to completely fill the intergranular space between WC grains when the intergranular distance approaches the lattice parameter of cobalt (≈0.4 nm). In such cases, the length of WC/WC contacts increases, while the length of the WC/Co phase boundary decreases. It is important to note that the limited resolution of scanning electron microscopes makes it difficult to observe such microstructural features.

To confirm this effect, an additional analysis was performed to assess the applicability of these relationships (Figs. 4 and 5) for describing the microstructures of ultrafine-grained cemented carbides compared to conventional cemented carbides based on literature data [4; 5; 11; 18; 23–26]. It should be noted that all contiguity measurements in the cited studies were performed using images obtained by conventional scanning electron microscopy (SEM). The use of electron backscatter diffraction (EBSD) enables the identification of a greater number of WC/WC grain boundaries, thus providing a more accurate assessment of contiguity [6; 19–23; 25–28]. However, applying this method to UFG and NS tungsten-cobalt cemented carbides is challenging due to its limited resolution. Moreover, the existing relationships between hardness, strength, contiguity, and other microstructural parameters have been established based on SEM-derived data. Consequently, contiguity values obtained via EBSD are not applicable to these models.

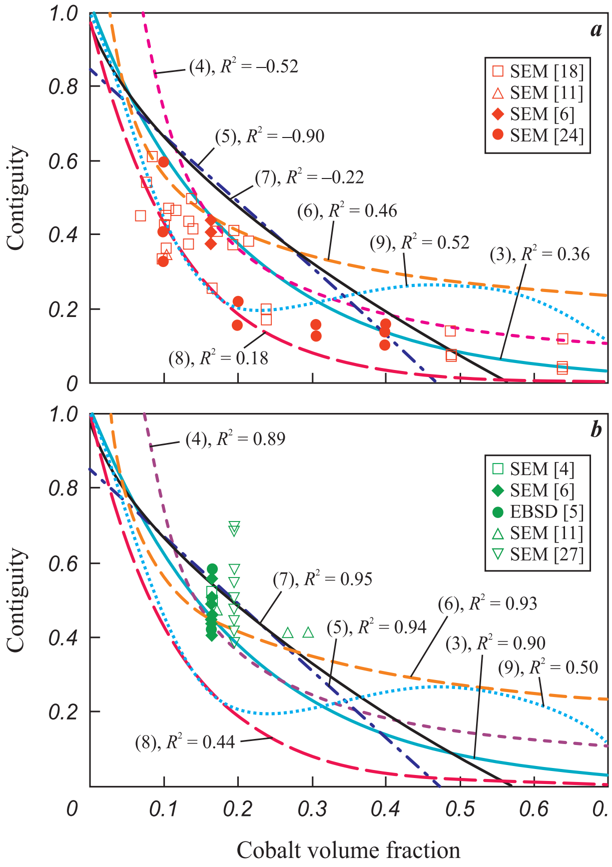

Fig. 5. Dependence of the experimental contiguity values on the cobalt volume fraction in the microstructure of submicron, fine-, and medium-grained (***a***), as well as nanostructured and ultrafine-grained (***b***) tungsten-cobalt cemented carbides fabricated by various researchers

Рис. 5. Зависимость экспериментальных значений смежности от объемной доли кобальта в микроструктуре субмикронных, мелко- и среднезернистых (***a***), а также наноструктурных и ультрамелкозернистых (***b***) металлокерамических вольфрамокобальтовых сплавов, полученных разными исследователями

From Fig. 5, *a*, it can be seen that only dependence (9) satisfactorily describes ($R^2 = 0.52 > 0.50$) the contiguity of conventional tungsten-cobalt cemented carbides, based on a sufficiently large dataset (87 values) from 10 different studies. Dependence (9) is positioned lower than relationships (3), (5), (6), and (7), which describe ultrafine-grained and nanostructured cemented carbides. Fig. 5, *b* presents contiguity values for UFG and NS cemented carbides, extracted from the same literature sources. It is evident that the dataset is incomplete due to the uneven representation of different cobalt concentrations, making it impossible to reliably assess the applicability of these dependencies for describing the contiguity of UFG and NS tungsten-cobalt cemented carbides. However, from Fig. 5, *b*, it follows that the contiguity values of UFG and NS cemented carbides fall in the upper range, close to dependencies (3)–(7) and far from (8)–(9), which are positioned lower. This suggests that the literature data also confirm that the contiguity of UFG and NS cemented carbides is higher than that of conventional cemented carbides.

All existing models describing the hardness of cemented carbides are based on the theory of mutual dislocation motion blocking in the cobalt matrix and the carbide skeleton [11; 18; 29]. The influence of microdefects on the hardness of cemented carbides has not been sufficiently studied [11]. The most widely accepted and commonly used model for describing the hardness of conventional cemented carbides is the one proposed by [18–20], which serves as the null hypothesis for all researchers developing new models [30–33]. This model is based on the rule of mixtures and the hypothesis of mutual dislocation motion blocking in the carbide framework and cobalt layers:

$$HV = HV_{\mathrm{WC}} V_{\mathrm{WC}} C + HV_{\mathrm{Co}} (1 - V_{\mathrm{WC}} C). \qquad (10)$$

The hardness of the carbide framework (HV_{WC}) and cobalt layers (HV_{Co}) is determined using the Hall–Petch law [11; 18; 29]:

$$HV_{\text{WC}} = 1382 + \frac{23.1}{\sqrt{d / 1000}}, \tag{11}$$

$$HV_{\text{Co}} = 304 + \frac{12.7}{\sqrt{\lambda / 1000}}. \tag{12}$$

where d is the average WC grain size, μm; λ is the mean free path in cobalt, μm.

Fig. 6 shows that the experimental hardness values of all samples are lower than the theoretical estimates calculated using equations (10)–(12) based on microstructural parameters (see Table 2). This discrepancy is likely related to deviations in the hardness of the alloy constituents (WC and Co) from the values predicted by the Hall–Petch relationships (11) and (12). The most significant deviation is observed in nanostructured alloys *1*–*3*. The hardness values of ultrafine-grained cemented carbides reported by other researchers [5; 6], the highest of which does not exceed 2100 HV, are satisfactorily described by the relationship (10) ($R^2 = 0.53$ and 0.88). However, the hardness of the nanostructured alloy (2356 HV) reported in [4] was found to be 50 % lower than the calculated value (3517 HV). The deviations of experimental hardness values from theoretical predictions in nanostructured cemented carbides, as confirmed in this study, are likely due to the activation of non-dislocation deformation mechanisms.

Due to their smaller grain size, all samples (Fig. 6) exhibited significantly higher hardness values ($HV = 1770 \div 2260$), compared to conventional cemented carbides ($HV = 1063 \div 1630$). As a result, such tool materials are expected to demonstrate superior operational performance, including wear resistance and machining precision. The hardness of samples *5*–*8*, produced via liquid phase sintering, was lower than that of the SPS-sintered samples (samples *1*–*4*). This can be attributed to their higher cobalt content and larger average WC grain size. Due to its small carbide grain size (0.17 μm) and high WC content, nanostructured cemented carbide sample *2* ($WC–5Co–0.4VC–0.4Cr_3C_2$) exhibited the highest hardness ($HV = 2260 \pm 30$). The SPS-sintered tungsten carbide, with a larger average grain size (0.5 μm), demonstrated slightly lower hardness ($HV = 2250 \pm 20$).

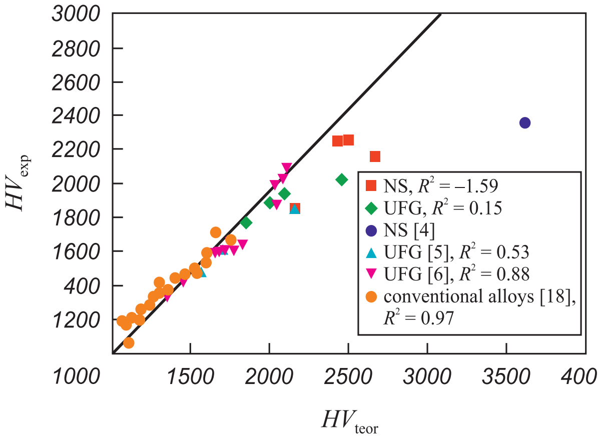

Fig. 6. Comparison of experimental and theoretical hardness values of ultrafine-grained and nanostructured conventional cemented carbides and those fabricated using LPS and SPS

Рис. 6. Сопоставление экспериментальных и теоретических значений твердости образцов УМЗ и НС обычных твердых сплавов и полученных методами ЖФС и ИПС

Conclusions

Nanostructured tungsten-cobalt cemented carbides with an average grain size of $d \sim 0.2$ μm can be fabricated via spark plasma sintering of nanopowders with grain growth inhibitors at 1200 °C. Increasing the cobalt volume fraction from 6.8 wt. % to 16.3 wt. % leads to an increase in the relative density of sintered nanostructured cemented carbides from 98.4 to 99.5 % while having little effect on the WC grain size. Using liquid phase sintering at 1450 °C for 1 h, alloys with a density ranging from 98.3 to 99.9 % and $d = 0.24–0.28$ μm can be obtained from powders containing 6–15 wt. % Co. An increase in cobalt concentration results in higher density (due to an increased pore-filling rate) and larger grain size due to recrystallization via the liquid phase. Spark plasma sintering of nanopowdered tungsten carbide at 2000 °C enables the fabrication of an ultrafine-grained ceramic material with an average grain size of 0.5 μm and a maximum relative density of 99.9 %.

Measuring contiguity in nanostructured tungsten-cobalt cemented carbides is challenging due to their small grain size. The dependence of contiguity in sintered nanostructured and ultrafine-grained cemented carbides on the cobalt volume fraction was best described by a known exponential relationship $C = 1.03\exp(-5V_{\text{Co}})$. Analysis of literature data has shown that many previously developed contiguity dependencies for conventional medium-grained, fine-grained, and submicron-grained cemented carbides are not applicable for describing nanostructured and ultrafine-grained materials, as their predicted values underestimate the experimental data.

The tungsten-cobalt cemented carbides obtained in this study exhibited significantly higher hardness than conventional medium-grained, fine-grained, and submicron-grained cemented carbides, primarily due to their smaller WC grain size. However, the experimental hardness values of the sintered cemented carbides were lower than theoretical predictions based on the Gurland and Lee model [18], which is derived from the Hall–Petch relationship. This discrepancy is likely due to the activation of non-dislocation deformation mechanisms. Due to its small WC grain size and high tungsten carbide content, sample *2* ($WC–5Co–0.4VC–0.4Cr_3C_2$) with an average WC grain size of 0.17 μm exhibited the highest hardness ($HV = 2260 \pm 30$). The SPS-sintered tungsten carbide, with a larger WC grain size of 0.5 μm, exhibited a comparable hardness ($HV = 2250 \pm 20$).

References / Список литературы

1. Dvornik M.I., Zaitsev A.V. Change in strength, hardness and cracking resistance in transition from medium-grained to ultrafine hard alloy. *Powder Metallurgy and Functional Coatings*. 2017;(2):39–46. (In Russ.).
https://doi.org/10.17073/1997-308X-2017-2-39-46

Дворник М.И., Зайцев А.В. Изменение прочности, твердости и трещиностойкости при переходе от среднезернистого к ультрамелкозернистому твердому сплаву. *Известия вузов. Порошковая металлургия и функциональные покрытия*. 2017;(2):39–46.
https://doi.org/10.17073/1997-308X-2017-2-39-46

2. Dvornik M.I., Zaitsev A.V. Variation in strength, hardness, and fracture toughness in transition from medium-grained to ultrafine hard alloy. *Russian Journal of Non-Ferrous Metals*. 2018;59(5):563–569.
https://doi.org/10.3103/S1067821218050024

3. Dvornik M.I., Mikhailenko E.A. Production of WC–15Co ultrafine-grained hard alloy from powder obtained by VK15 alloy waste spark erosion in water. *Powder Metallurgy and Functional Coatings*. 2020;14(3):4–16. (In Russ.).
https://doi.org/10.17073/1997-308X-2020-3-4-16

Дворник М.И., Михайленко Е.А. Создание ультрамелкозернистого твердого сплава WC–15Co из порошка, полученного электроэрозионным диспергированием отходов сплава ВК15 в воде. *Известия вузов. Порошковая металлургия и функциональные покрытия*. 2020;14(3):4–16.
https://doi.org/10.17073/1997-308X-2020-3-4-16

4. Peng Y., Wang H., Zhao C., Hu H., Liu X., Song X. Nanocrystalline WC–Co composite with ultrahigh hardness and toughness. *Composites Part B: Engineering*. 2020;197:108161.
https://doi.org/10.1016/j.compositesb.2020.108161

5. Zhao S., Song X., Wei C., Zhang L., Liu X., Zhang J. Effects of WC particle size on densification and properties of spark plasma sintered WC–Co cermet. *International Journal of Refractory Metals and Hard Materials*. 2009;27(6):1014–1018.
https://doi.org/10.1016/j.ijrmhm.2009.07.017

6. Zhao S., Wei C. Quantitative relationships between microstructure parameters and mechanical properties of ultrafine cemented carbides. *Acta Metallurgica Sinica*. 2011;47(9):1188–1194.

7. Dvornik M., Mokritskiy B., Zaytsev A. Comparative analysis of microabrasive wear resistance of traditional hard alloys and submicron hard alloy $WC–8Co–1Cr_3C_2$. *Voprosy materialovedeniya*. 2015;(1):45–51. (In Russ.).

Дворник М., Мокрицкий Б., Зайцев А. Сравнительный анализ микроабразивной износостойкости традиционных твердых сплавов и субмикронного твердого сплава $WC–8Co–1Cr_3C_2$. *Вопросы материаловедения*. 2015;(1):45–51.

8. Fedorov D.V., Semenov O.V., Rumyantsev V.I., Ordanyan S.S. Peculiarities of compacting during sintering of VH8M alloy with addition of nanosized tungsten carbide. *Powder Metallurgy and Functional Coatings*. 2014;(3):26–30. (In Russ.).
https://doi.org/10.17073/1997-308X-2014-3-26-30

Федоров Д.В., Семенов О.В., Румянцев В.И., Орданьян С.С. Особенности уплотнения при спекании сплава ВН8М с добавками наноразмерного карбида вольфрама. *Известия вузов. Порошковая металлургия и функциональные покрытия*. 2014;(3):26–30.
https://doi.org/10.17073/1997-308X-2014-3-26-30

9. Wu Y., Lu Z., Qin Y., Bao Z., Luo L. Ultrafine/nano WC–Co cemented carbide: Overview of preparation and key technologies. *Journal of Materials Research and Technology*. 2023;27:5822–5839.
https://doi.org/10.1016/j.jmrt.2023.10.315

10. Siwak P. Indentation induced mechanical behavior of spark plasma sintered WC–Co cemented carbides alloyed with Cr_3C_2, TaC–NbC, TiC, and VC. *Materials*. 2021;14(1):217–234. https://doi.org/10.3390/ma14010217

11. Jia K., Fischer T., Gallois B. Microstructure, hardness and toughness of nanostructured and conventional WC–Co composites. *Nanostructured materials*. 1998;10(5):875–891.
https://doi.org/10.1016/s0965-9773(98)00123-8

12. Sun J., Zhao J., Huang Z., Yan K., Shen X., Xing J., Gao Y., Jian Y., Yang H., Li B. A review on binderless tungsten carbide: Development and application. *Nano-Micro Letters*. 2020;12(1):1–37.
https://doi.org/10.1007/s40820-019-0346-1

13. Kim H.-C., Shon I.-J., Garay J., Munir Z. Consolidation and properties of binderless sub-micron tungsten carbide by field-activated sintering. *International Journal of Refractory Metals and Hard Materials*. 2004;22(6):257–264.
https://doi.org/10.1016/j.ijrmhm.2004.08.003

14. Kim H.-C., Yoon J.-K., Doh J.-M., Ko I.-Y., Shon I.-J. Rapid sintering process and mechanical properties of binderless ultra fine tungsten carbide. *Materials Science and Engineering: A*. 2006;435–436:717–724.
https://doi.org/10.1016/j.msea.2006.07.127

15. Huang B., Chen L., Bai S. Bulk ultrafine binderless WC prepared by spark plasma sintering. *Scripta Materialia*. 2006;54(3):441–445.
https://doi.org/10.1016/J.SCRIPTAMAT.2005.10.014

16. Dopita M., Salomon A., Chmelik D., Reichelt B., Rafaja D. Field assisted sintering technique compaction of ultrafine-grained binderless WC hard metals. *Acta Physica Polonica A*. 2012;122(3):639–642.
http://dx.doi.org/10.12693/APhysPolA.122.639

17. Mingard K. P., Roebuck B. Interlaboratory measurements of contiguity in WC–Co hardmetals. *Metals*. 2019; 9(3):328. https://doi.org/10.3390/MET9030328

18. Lee H.-C., Gurland J. Hardness and deformation of cemented tungsten carbide. *Materials science and engineering*. 1978;33(1):125–133.
https://doi.org/10.1016/0025-5416(78)90163-5

19. Chermant J., Osterstock F. Elastic and plastic characteristics of WC–Co composite materials. *Journal of Materials Science*. 1976;11(3):106–109.

20. Gurland J. A structural approach to the yield strength of two-phase alloys with coarse microstructures. *Materials Science and Engineering*. 1979;40(1):59–71.
https://doi.org/10.1016/0025-5416(79)90008-9

21. Exner H., Fischmeister H. Structure of sintered tungsten carbide-cobalt alloys. *Archiv für das Eisenhüttenwesen*. 1966;(37):409–415.

22. Roebuck B., Bennett E.G. Phase size distribution in WC/Co hardmetal. *Metallography*. 1986;19(1):27–47.
https://doi.org/10.1016/0026-0800(86)90005-4

23. Luyckx S., Love A. The dependence of the contiguity of WC on Co content and its independence from WC grain size in WC–Co alloys. *International Journal of Refractory Metals and Hard Materials*. 2006;24(1-2):75–79.
https://doi.org/10.1016/j.ijrmhm.2005.04.012

24. Nakamura M., Gurland J. The fracture toughness of WC–Co two-phase alloys – A preliminary model. *Metallurgical and Materials Transactions A*. 1980;11(1):141–146.
https://doi.org/10.1007/BF02700449

25. Mingard K., Roebuck B., Bennett E., Gee M., Nordenstrom H., Sweetman G., Chan P. Comparison of EBSD and conventional methods of grain size measurement of hardmetals. *International Journal of Refractory Metals and Hard Materials*. 2009;27(2):213–223.
https://doi.org/10.1016/J.IJRMHM.2008.06.009

26. Tarrago J.M., Coureaux D., Torres Y., Wu F., Al-Dawery I., Llanes L. Implementation of an effective time-saving two-stage methodology for microstructural characterization of cemented carbides. *International Journal of Refractory Metals and Hard Materials*. 2016;55:80–86.
https://doi.org/10.1016/J.IJRMHM.2015.10.006

27. Mandel K., Krüger L., Schimpf C. Study on parameter optimisation for field-assisted sintering of fully-dense, near-nano WC–12Co. *International Journal of Refractory Metals and Hard Materials*. 2014;45:153–159.
https://doi.org/10.1016/j.ijrmhm.2014.04.009

28. Pellan M., Lay S., Missiaen J. M., Norgren S., Angseryd J., Coronel E., Persson T. Effect of binder composition on WC grain growth in cemented carbides. *Journal of the American Ceramic Society*. 2015;98(11):3596–3601.
https://doi.org/10.1111/jace.13748

29. Liu X., Zhang J., Hou C., Wang H., Song X., Nie Z. Mechanisms of WC plastic deformation in cemented carbide. *Materials & Design*. 2018;150:154–164.
https://doi.org/10.1016/j.matdes.2018.04.025

30. Xu Z.-H., Ågren J.A modified hardness model for WC–Co cemented carbides. *Materials Science and Engineering: A*. 2004;386(1-2):262–268.
https://doi.org/10.1016/j.msea.2004.07.061

31. Cha S.I., Lee K.H., Ryu H.J., Hong S.H. Analytical modeling to calculate the hardness of ultra-fine WC–Co cemented carbides. *Materials Science and Engineering: A*. 2008;489(1-2):234–244.
https://doi.org/10.1016/j.msea.2007.12.036

32. Makhele-Lekala L., Luyckx S., Nabarro F. Semi-empirical relationship between the hardness, grain size and mean free path of WC–Co. *International Journal of Refractory Metals and Hard Materials*. 2001;19(4-6):245–249.
https://doi.org/10.1016/S0263-4368(01)00022-1

33. Kresse T., Meinhard D., Bernthaler T., Schneider G. Hardness of WC–Co hard metals: Preparation, quantitative microstructure analysis, structure-property relationship and modeling. *International Journal of Refractory Metals & Hard Materials*. 2018;(75):287–293.
https://doi.org/10.1016/j.ijrmhm.2018.05.003

Information about the Authors

Maksim I. Dvornik – Cand. Sci. (Eng.), Senior Research Scientist, Head of the Powder Metallurgy Laboratories, Khabarovsk Federal Research Center of the Far Eastern Branch of the Russian Academy of Sciences (KhFRC FEB RAS)
ORCID: 0000-0002-1216-4438
E-mail: maxxxx80@mail.ru

Elena A. Mikhailenko – Cand. Sci. (Phys.-Math.) Senior Research Scientist of the Laboratory of Powder Metallurgy, KhFRC FEB RAS
ORCID: 0000-0002-4515-9109
E-mail: mea80@list.ru

Oleg O. Shichalin – Cand. Sci. (Chem.) Senior Research Scientist of the Institute of Science-Intensive Technologies and Advanced Materials, Far Eastern Federal University
ORCID: 0000-0002-2441-6209
E-mail: oleg_shich@mail.ru

Igor Yu. Buravlev – Cand. Sci. (Chem.) Deputy Director for Development of the Institute of Science-Intensive Technologies and Advanced Materials, Far Eastern Federal University
ORCID: 0000-0003-3944-3629
E-mail: buravlev.i@gmail.com

Сведения об авторах

Максим Иванович Дворник – к.т.н., ст. науч. сотрудник, зав. лабораторией порошковой металлургии, Хабаровский федеральный исследовательский центр Дальневосточного отделения Российской академии наук (ХФИЦ ДВО РАН)
ORCID: 0000-0002-1216-4438
E-mail: maxxxx80@mail.ru

Елена Альбертовна Михайленко – к.ф.-м.н., ст. науч. сотрудник лаборатории порошковой металлургии, ХФИЦ ДВО РАН
ORCID: 0000-0002-4515-9109
E-mail: mea80@list.ru

Олег Олегович Шичалин – к.х.н., ст. науч. сотрудник Института наукоемких технологий и передовых материалов, Дальневосточный федеральный университет
ORCID: 0000-0002-2441-6209
E-mail: oleg_shich@mail.ru

Игорь Юрьевич Буравлев – к.х.н., зам. директора по развитию Института наукоемких технологий и передовых материалов, Дальневосточный федеральный университет
ORCID: 0000-0003-3944-3629
E-mail: buravlev.i@gmail.com

Aleksandr A. Burkov – Cand. Sci. (Phys.-Math.), Senior Researcher, Head of the Laboratory of Physical and Chemical Fundamentals of Material's Technology, KhFRC FEB RAS
ORCID: 0000-0002-5636-4669
E-mail: burkovalex@mail.ru

Nuriya M. Vlasova – Cand. Sci. (Eng.), Research Scientist of the Powder Metallurgy Laboratories, KhFRC FEB RAS
ORCID: 0000-0003-0198-0912
E-mail: vlasova64@yandex.ru

Evgeny V. Chernyakov – Laboratory Assistant of the Powder Metallurgy Laboratories, KhFRC FEB RAS
E-mail: tchernyakoffevgeny@yandex.ru

Vladimir K. Khe – Junior Research Scientist of the Laboratories of Construction and Instrumental Materials, KhFRC FEB RAS
ORCID: 0000-0001-7672-1013
E-mail: khevlad@ya.ru

Pavel G. Chigrin – Cand. Sci. (Chem.) Senior Research Scientist of the Laboratory of Physical and Chemical Fundamentals of Material's Technology, KhFRC FEB RAS
ORCID: 0000-0002-1560-489X
E-mail: pal_chig@mail.ru

Александр Анатольевич Бурков – к.ф.-м.н., ст. науч. сотрудник, зав. лабораторией физико-химических основ технологии материалов, ХФИЦ ДВО РАН
ORCID: 0000-0002-5636-4669
E-mail: burkovalex@mail.ru

Нурия Мунавировна Власова – к.т.н., науч. сотрудник лаборатории порошковой металлургии, ХФИЦ ДВО РАН
ORCID: 0000-0003-0198-0912
E-mail: vlasova64@yandex.ru

Евгений Витальевич Черняков – лаборант лаборатории порошковой металлургии, ХФИЦ ДВО РАН
E-mail: tchernyakoffevgeny@yandex.ru

Владимир Канчерович Хе – мл. науч. сотрудник лаборатории конструкционных и инструментальных материалов, ХФИЦ ДВО РАН
ORCID: 0000-0001-7672-1013
E-mail: khevlad@ya.ru

Павел Геннадьевич Чигрин – к.х.н., ст. науч. сотрудник лаборатории физико-химических основ технологии материалов, ХФИЦ ДВО РАН
ORCID: 0000-0002-1560-489X
E-mail: pal_chig@mail.ru

Contribution of the Authors

M. I. Dvornik – formulated the research objectives, conducted experiments, analyzed the results, and wrote the article.

E. A. Mikhailenko – conducted experiments and participated in result discussions.
O. O. Shichalin – performed spark plasma sintering and participated in result discussions.
I. Yu. Buravlev – performed spark plasma sintering and participated in result discussions.
A. A. Burkov – conducted experiments and participated in result discussions.
N. M. Vlasova – conducted experiments.
E. V. Chernyakov – conducted experiments and calculations.
V. K. Khe – conducted experiments.
P. G. Chigrin – conducted experiments and participated in result discussions.

Вклад авторов

М. И. Дворник – определение цели и задач исследования, проведение экспериментов, анализ результатов, написание текста статьи.
Е. А. Михайленко – проведение экспериментов, участие в обсуждении результатов.
О. О. Шичалин – искровое плазменное спекание, обсуждение результатов.
И. Ю. Буравлев – искровое плазменное спекание, обсуждение результатов.
А. А. Бурков – проведение экспериментов, участие в обсуждении результатов.
Н. М. Власова – проведение экспериментов.
Е. В. Черняков – проведение экспериментов и расчетов.
В. К. Хе – проведение экспериментов.
П. Г. Чигрин – проведение экспериментов.

Received 28.11.2024
Revised 06.02.2025
Accepted 10.02.2025

Статья поступила 28.11.2024 г.
Доработана 06.02.2025 г.
Принята к публикации 10.02.2025 г.

Nanostructured Materials and Functional Coatings
Наноструктурированные материалы и функциональные покрытия

UDC 621.762

https://doi.org/10.17073/1997-308X-2025-2-62-72

Research article
Научная статья

Use of Ni and Al granules and WC powder for electric spark deposition of metalloceramic coatings

A. A. Burkov

Khabarovsk Federal Research Center
of the Far Eastern Branch of the Russian Academy of Sciences
153 Tikhookeanskaya Str., Khabarovsk 680042, Russia

✉ burkovalex@mail.ru

Abstract. Research on novel metalloceramic coatings that combine high-temperature oxidation resistance and wear resistance remains a relevant topic. Ni–Al–Fe coatings reinforced with varying amounts of tungsten carbide were synthesized for the first time using electric spark deposition on 35 steel. Their structure was analyzed using *X*-ray phase analysis and scanning electron microscopy. The average thickness of the WC/Ni–Al–Fe coatings ranged from 23 to 33 μm. The identified phases included AlNi, (Fe, Ni), α-WC, and W_2C. The coating microstructure exhibited reinforcing tungsten carbide inclusions with diameters ranging from 1.49 to 10.12 μm. The corrosion behavior of coated samples was studied using potentiodynamic polarization and impedance spectroscopy in a 3.5 % NaCl solution. The coatings' high-temperature oxidation resistance was evaluated at 700 °C for 110 h under natural aeration conditions. Wear testing was conducted under dry friction conditions at loads of 25 and 50 N. The results demonstrate that the application of WC/Ni–Al–Fe-coatings can reduce the specific wear of the steel surface by a factor of 11 to 24 and enhances resistance to high-temperature oxidation by a factor of 10.5 to 49.9.

Keywords: WC/Ni–Al–Fe coatings, electric spark deposition, nonlocalized electrode (NLE), St3 steel, *X*-ray phase analysis, corrosion, friction coefficient, hardness, wear

Acknowledgements: The work was carried out within the framework of state assignment No. 075-01108-23-02.

For citation: Burkov A.A. Use of Ni and Al granules and WC powder for electric spark deposition of metalloceramic coatings. *Powder Metallurgy and Functional Coatings*. 2025;19(2):62–72. https://doi.org/10.17073/1997-308X-2025-2-62-72

Использование гранул Ni и Al и порошка WC для электроискрового нанесения металлокерамических покрытий

А. А. Бурков

Хабаровский федеральный исследовательский центр
Дальневосточного отделения Российской академии наук
Россия, 680042, г. Хабаровск, ул. Тихоокеанская, 153

✉ burkovalex@mail.ru

Аннотация. Исследования новых металлокерамических покрытий, сочетающих высокую жаростойкость и устойчивость к износу, являются актуальными. Ni–Al–Fe покрытия, армированные различным количеством карбида вольфрама, впервые получены методом электроискрового легирования на стали 35. Их структура исследовалась методами рентгеноструктурного фазового анализа и сканирующей электронной микроскопии. Средняя толщина WC/Ni–Al–Fe-покрытий составляла от 23 до 33 мкм. В их составе идентифицированы фазы AlNi, (Fe, Ni), α-WC и W_2C. В микроструктуре покрытий наблюдались армирующие включения карбида вольфрама диаметром от 1,49 до 10,12 мкм. Коррозионное поведение образцов с покрытиями изучалось методами потенциодинамической поляризации и импедансной спектроскопии в 3,5 %-ном растворе NaCl. Жаростойкость покрытий исследовалась при температуре 700 °C в течение 110 ч в условиях естественной аэрации. Тестирование на износ проводилось в режиме сухого трения при нагрузках 25 и 50 Н. Показано, что применение WC/Ni–Al–Fe-покрытий позволяет сократить приведенный износ поверхности стальных изделий с 11 до 24 раз и повысить стойкость к высокотемпературной газовой коррозии с 10,5 до 49,9 раза.

Ключевые слова: покрытия WC/Ni–Al–Fe, электроискровое легирование, нелокализованный электрод (НЭ), сталь Ст3, рентгенофазовый анализ, коррозия, коэффициент трения, твердость, износ

Благодарности: Работа выполнена в рамках государственного задания № 075-01108-23-02.

Для цитирования: Бурков А.А. Использование гранул Ni и Al и порошка WC для электроискрового нанесения металлокерамических покрытий. *Известия вузов. Порошковая металлургия и функциональные покрытия*. 2025;19(2):62–72. https://doi.org/10.17073/1997-308X-2025-2-62-72

Introduction

Metalloceramic composites (MCCs) are among the most widely used wear-resistant materials [1]. They typically consist of hard carbide particles (WC, TiC, TiB_2, TaC, NbC) bonded by ductile metallic phases such as Co, Fe, and Ni [2]. The carbide particles in these composites provide high hardness and wear resistance, while the binder phase enhances toughness. Over the past century, among various carbide-based materials, tungsten carbide (WC) composites have found the broadest application across multiple industries [3–5]. A key aspect of this class of metalloceramics is the type of metallic binder used.

For many years, cobalt has been the most commonly used metallic binder due to its excellent wettability with tungsten carbide grains and the high impact toughness it provides [6]. However, its use raises serious environmental concerns and is further limited by its high cost. Studies indicate that prolonged inhalation exposure to cobalt can cause allergic reactions and cancer [7]. Additionally, its poor corrosion and oxidation resistance, along with unsatisfactory mechanical performance at temperatures above 600 °C, have driven researchers to seek alternative binders [8].

For instance, intermetallic Ni–Al alloys are sometimes considered as metallic binders [9; 10] due to their favorable properties, including high melting points, heat resistance, low density, and excellent oxidation resistance, which can compensate for tungsten carbide's poor oxidation resistance [11].

Iron aluminide (FeAl) is known to be a suitable binding matrix for tungsten carbide due to its favorable properties, including good wettability with WC, enhanced hardness, low density, and high oxidation resistance in oxidative, carburizing, and sulfidizing environments [12]. A dense Al_2O_3 film, known for its excellent protective properties, can form on the surface of nickel and iron aluminides [13]. However, ternary Al–Ni–Fe alloys remain significantly less studied [14], despite their potential for enhanced hardness and oxidation resistance, while also requiring less nickel compared to NiAl-based materials. Additionally, nickel alloying of FeAl has been shown to induce significant solid-solution strengthening [15].

Tungsten carbide-based metalloceramic composites are widely used as coatings on structural metals to improve hardness, wear resistance, and oxidation resistance [16; 17]. For instance, in studies [18; 19], WC/FeAl coatings were deposited onto structural steels using laser cladding and high-velocity arc spraying. However, tungsten carbide-based coatings with Ni–Al and Ni–Al–Fe matrices have been explored to a much lesser extent. In [20], WC/NiAl/TiC coatings were prepared using laser cladding. A $(NiAl)_{0.8}WC_{0.2}$–Fe(0–15 wt. %) coating with a ternary Ni–Al–Fe matrix was deposited onto low-alloy Q235 steel using plasma cladding [17].

The electric spark deposition (ESD) method is employed for depositing metallic and metalloceramic materials onto metal substrates and is characterized by minimal thermal impact on the base material's structure, while producing coatings with strong adhesion [21]. The use of a nonlocalized electrode (NLE) in ESD enables automation of the deposition process, including applications on complex-shaped components [22]. In our previous study, the electric spark deposition with a nonlocalized electrode (ESD-NLE) method was used to produce WC/Fe–Al coatings, where the NLE consisted of aluminum and iron granules combined with α-WC powder [23].

The objective of this study is to investigate the feasibility of producing metalloceramic coatings using the ESD-NLE method on 35 steel, using Ni and Al granules along with WC powder.

Materials and methods

The composition of the NLE is shown in Table 1. The aluminum alloy 1188 and high-purity nickel (99.99 %) granules were shaped as cylinders ($h = 4 \pm 1$ mm, $d = 4 \pm 0.5$ mm) and cubes

Table 1. **Coating designation based on NLE composition**

Таблица 1. **Маркировка покрытий в зависимости от состава НЭ**

Sample	Granule ratio, at. %		Granule fraction, vol. %	WC powder fraction, vol. %
	Al	Ni		
ANW2	15	85	98	2
ANW4			96	4
ANW6			94	6

(4×4×4 ± 0.5 mm), respectively. The tungsten carbide powder (TU 6-09-03-360-78) had a purity of 99.9 % and an average particle diameter of 1.1 ± 0.3 μm. The NLE composition was designed with a dominance of nickel, maintaining a Ni/Al ratio of 17:3, as aluminum has significantly lower electroerosion resistance than nickel [24]. The 35 steel substrate acted as an iron source for the WC/Ni–Al–Fe coatings, as iron from the steel base is known to diffuse into ESD coatings [23]. Fig. 1 illustrates the schematic of the ESD setup operating in an environment of granules and powder.

The 35 steel substrate was fabricated in the form of a cylinder ($d = 12$ mm, $h = 10$ mm). The IMES-40 power generator, operating at 30 V, produced current pulses with an amplitude of 110 A, a duration of 100 μs, and a period of 1000 μs. To minimize oxidation, coating deposition was carried out under an argon flow (5 L/min). The deposition time for each sample was 10 min.

The phase composition of the obtained coatings was analyzed using a DROH-7 X-ray diffractometer (NPP Burevestnik, Russia) with CuK_α radiation ($\lambda = 1.54056$ Å). The microstructure and elemental composition of the coatings were examined using a Vega 3 LMH scanning electron microscope (Tescan, Czech Republic) equipped with an X-max 80 energy-dispersive spectrometer (EDS) (Oxford Instruments, UK). The surface roughness of the coatings was measured using the R_a parameter with a Profilometer 296 (USSR). The wettability of the coated surfaces with deionized water was evaluated using the sessile drop method at 25 °C [25]. The Vickers hardness of the coatings was measured using a PMT-3M microhardness tester under a 1.96 N load. Tribological tests were conducted following the ASTM G99-17 procedure using the pin-on-disk configuration (without rounding of the pin end) at a rotation frequency of 3 rev/s under loads of 25 and 50 N for 10 min. High-speed steel M45 disks ($d = 50$ mm, 60 HRC) were used as counterbodies.

The tribological tests were performed on a laboratory test bench equipped with a M40-50 non-contact torque sensor (Belarus). The specific wear rate was determined gravimetrically, considering the density of the coatings, which was calculated using the rule of mixtures based on the chemical composition. The electrochemical corrosion tests of coated samples were conducted using a P-40X potentiostat-galvanostat (Electro Chemical Instruments, Russia) equipped with an impedance measurement module, in a standard

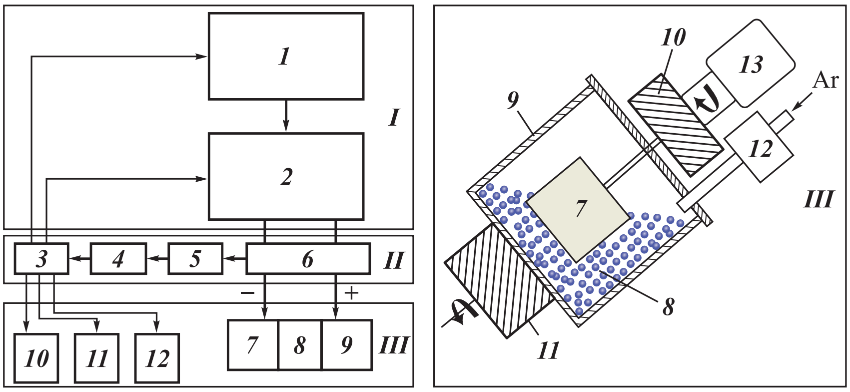

Fig. 1. Schematic of the experimental setup for electric spark granules deposition of granules

I – pulse discharge generation unit, ***II*** – measuring and control unit, ***III*** – electrode switching unit
1 – control pulse generator, ***2*** – power generator, ***3*** – microcontroller, ***4*** – computer, ***5*** – analog-to-digital converter,
6 – current and voltage measuring device, ***7*** – cathode (35 steel), ***8*** – Ni and Al granules, WC powder, ***9*** – current lead (container),
10, ***11*** – motors for the cathode and the granule container, respectively, ***12*** – gas solenoid valve, ***13*** – micromanipulator

Рис. 1. Схема экспериментальной установки для электроискрового осаждения гранул

I – блок генерации разрядных импульсов, ***II*** – измерительный и управляющий блок,
III – блок коммутации электродов
1 – генератор управляющих импульсов, ***2*** – силовой генератор, ***3*** – микроконтроллер, ***4*** – компьютер,
5 – аналого-цифровой преобразователь, ***6*** – измерительное устройство тока и напряжения, ***7*** – катод (сталь 35),
8 – гранулы Ni и Al, порошок WC, ***9*** – токопровод (контейнер), ***10***, ***11*** – двигатели катода и контейнера с гранулами соответственно,
12 – газовый электроклапан, ***13*** – микроманипулятор

three-electrode cell containing a 3.5 % NaCl solution. An Ag/AgCl electrode served as the reference electrode, while an ETP-02 platinum electrode was used as the counter electrode. To stabilize the open-circuit potential, the samples were immersed in the electrolyte solution for 60 min before measurements.

Cyclic oxidation resistance was tested at 700 °C. The samples were placed in a preheated muffle furnace, held for approximately 6 h, then transferred to a desiccator until fully cooled before weighing. During testing, the samples were kept in corundum crucibles to prevent the loss of spalled oxide scale. The total test duration was 100 h.

Results and discussion

When testing new electrode materials, it is essential to record mass transfer during ESD to determine the specific mass gain of the cathode, as this parameter defines the thickness of the formed coating [21]. As the number of discharge pulses increased (i.e., with longer ESD-NLE duration), the cathode continuously gained mass (Fig. 2). Over 10 min of ESD-NLE, the total specific mass gain ranged from 4.2 to 6.3 mg/cm^2. The average values were independent of the electrode type, considering the measurement error.

Fig. 3, *a*, *c*, and *e* show cross-sections of WC/Ni–Al–Fe coatings. As seen from Table 2, their average thickness is practically independent of the WC powder content in the NLE, ranging from 31.5 to 32.7 μm. The coating structure consists of a gray matrix reinforced with bright inclusions of micron- and submicron-sized particles. The diameter of the micron-sized inclusions ranges from 3 to 20 μm, and these are agglomerates of the original WC powder particles. According to EDS data, as the WC powder content in the NLE increases, the coating matrix composition is monotonically enriched with tungsten and iron, while the nickel and aluminum concentrations decrease (Fig. 3, *b*, *d*, *f*).

As the WC content in the NLE increases from ANW2 to ANW6, the average tungsten concentration in the coating matrix rises from 5.3 to 23.2 at. %, while the iron content increases from 35.5 to 57.6 at. %, and the nickel concentration decreases from 35.3 to 4.8 at. %. This is due to the fact that the powder elements in the ESD-NLE coating are present in disproportionately higher amounts than the granule components, a trend we previously observed [26]. ANW2 coating has the most balanced atomic ratio of aluminum, nickel, and iron.

Thus, adjusting the WC powder fraction in the electrode enables control over the metal ratio in the coating. The high iron concentration in the ANW6 coating matrix confirms the substrate material's involvement in the formation of the ESD coating. As the WC powder fraction in the NLE increases, the proportion of white inclusions in the coatings also rises, as seen in Fig. 3, *a*, *c*, *e*.

A small number of transverse microcracks are present in the coatings. These form due to rapid cooling of the material after discharge, caused by the difference in the coefficients of linear thermal expansion between the coating and the substrate [27]. The absence of longitudinal cracks and the gradual change in metal concentrations at the coating-substrate interface indicate strong adhesion of the WC/Ni–Al–Fe coatings to 35 steel. The coating roughness (R_a) ranged from 4.5

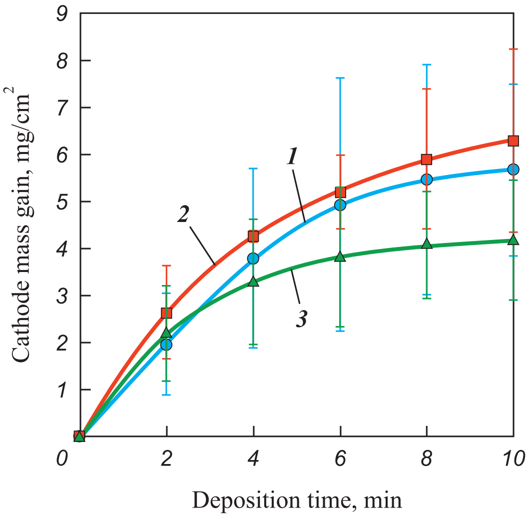

Fig. 2. Dependence of cathode mass gain on ESD-NLE duration

1 – ANW2, ***2*** – ANW4, ***3*** – ANW6

Рис. 2. Зависимость привеса катода от продолжительности ЭИЛНЭ

1 – ANW2, ***2*** – ANW4, ***3*** – ANW6

Table 2. **Characteristics of WC/Ni–Al–Fe coatings**

Таблица 2. **Характеристики WC/Ni–Al–Fe-покрытий**

Characteristic	ANW2	ANW4	ANW6
Thickness, μm	32.42 ± 1.77	31.48 ± 6.93	32.66 ± 2.48
Roughness, μm	4.50 ± 0.90	4.77 ± 1.10	4.51 ± 0.80
Wettability, deg	80.0	82.1	81.9

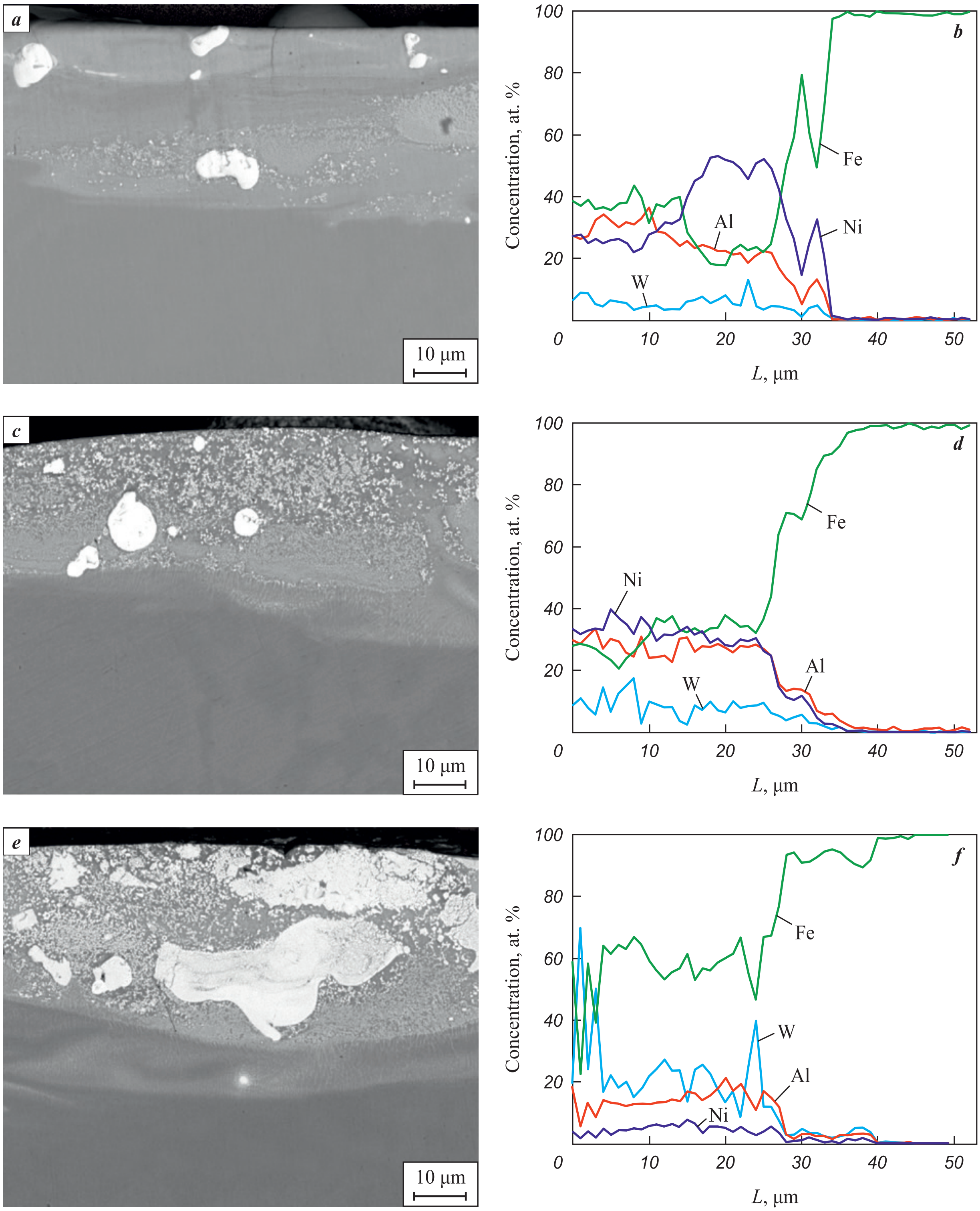

Fig. 3. SEM images and elemental distribution in the cross-section of ANW2 (***a***, ***b***), ANW4 (***c***, ***d***), and ANW6 (***e***, ***f***) coatings

Рис. 3. СЭМ-изображения и распределение элементов в поперечном сечении покрытий ANW2 (***a***, ***b***), ANW4 (***c***, ***d***) и ANW6 (***e***, ***f***)

to 4.77 μm and did not depend on the WC powder concentration (see Table 2). The contact angle of the coating surface with distilled water was between 80.0 and 82.1°, significantly higher than that of 35 steel (65.9°). Thus, the application of WC/Ni–Al–Fe coatings imparts hydrophobic properties to the steel surface.

According to Fig. 4, *a*, *c*, the large inclusions correspond to grains of the initial tungsten carbide (α-WC). Submicron inclusions formed after the discharge ceased, during the solidification of the Fe–W–Ni–Al–C melt (Fig. 4, *b*). A similar microstructure was previously observed in ESD coatings on 35 steel deposited using WC–Co anodes [28]. Thus, the formation of WC/Ni–Al–Fe coatings via ESD proceeds through two stages: sintering of refractory agglomerated WC particles and eutectic crystallization of the Fe–W–Ni–Al–C melt [29].

The results of *X*-ray phase analysis of the WC/Ni–Al–Fe coatings are shown in Fig. 5. The data indicate that, in addition to WC and W_2C, the coatings contain the intermetallic compound AlNi (PDF card #44-1188 from the PdWin database) and a face-centered cubic (FCC) Fe–Ni solid solution [30], which serve as the metallic matrix. The presence of ferro-nickel is attributed to the high nickel concentration in the ANW2 coating (see Fig. 2, *b*). The α-WC carbide and W_2C subcarbide act as reinforcing phases in the metalloceramic coating. The formation of W_2C occurs due to the decarburization of WC when it interacts with the iron melt in the micro-melt pool under electric discharge temperatures [24]. This is supported by an increase in the W_2C content from 14.1 to 24.1 vol. % (Table 3) as the iron concentration rises from ANW2 to ANW6 (see Figs. 3, *b*, *d*, *f*). Fig. 4, *a* illustrates the interaction between a tungsten carbide particle and the iron melt.

The WC phase fraction in the coatings increased from 48.6 to 65.5 vol. % with the addition of tungsten carbide powder to the NLE, while the intermetallic fraction decreased from 28.2 to 10.3 vol. %. Notably, such a high WC content in the coatings cannot be achieved using conventional single-electrode ESD on steels with hardmetal anodes, due to the high solubility of WC in liquid iron [31].

Based on the coating microstructure, the formation of mechanism of WC/Ni–Al–Fe coating during ESD-NLE can be described as follows: when a Ni or Al granule comes into electrical contact with the substrate, low-voltage discharges occur, causing the transfer of molten granule material into the micro-melt pool on the cathode surface. Tungsten carbide powder particles, located on the electrode surface within the discharge initiation and propagation zone, become wetted by metal droplets and are incorporated into

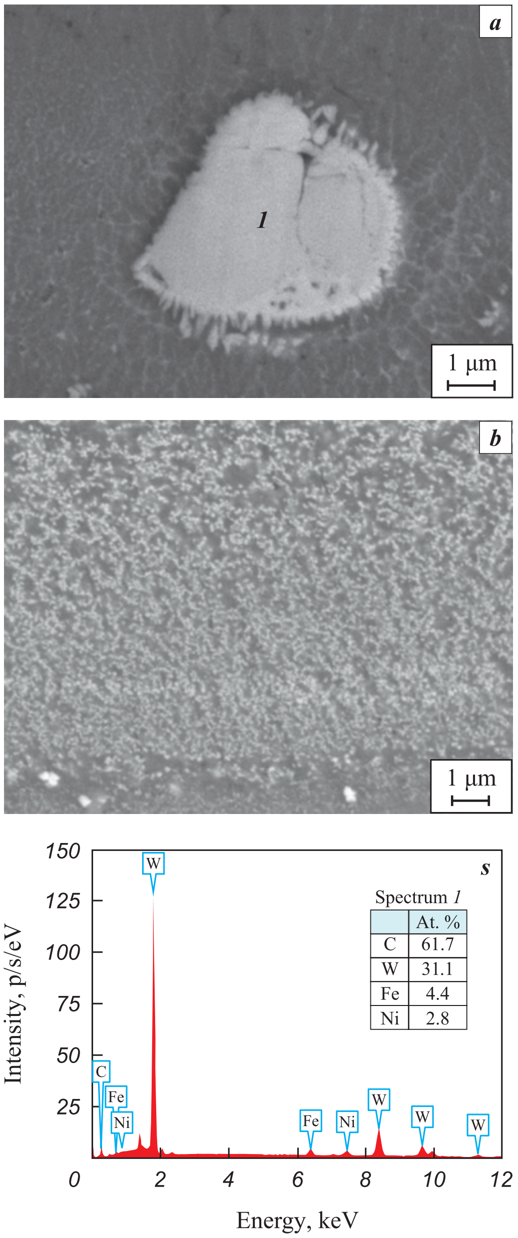

Spectrum *1*

	At. %
C	61.7
W	31.1
Fe	4.4
Ni	2.8

Fig. 4. Microstructure images of the cross-section of ANW2 at magnifications of 25,000× (***a***) and 20,000× (***b***)
c – EDS spectrum corresponding to Fig. 4, ***a***

Рис. 4. Изображения микроструктуры поперечного сечения образца ANW2 при увеличениях 25 000× (***a***) и 20 000× (***b***)
c – ЭДС-спектр к рис. 4, ***a***

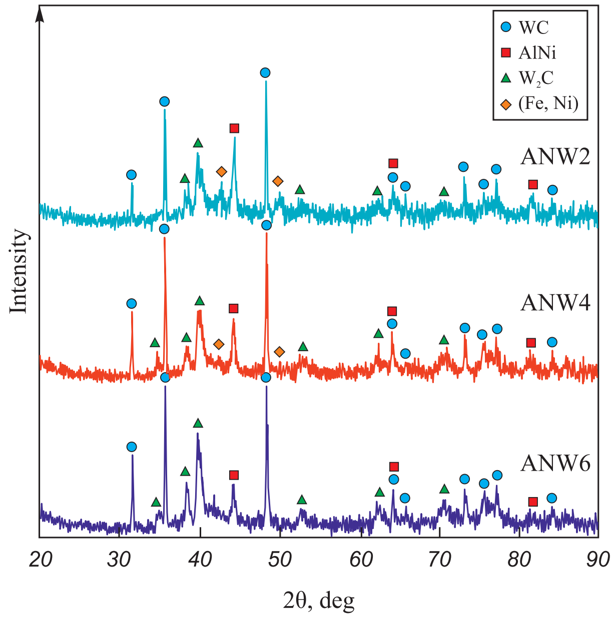

Fig. 5. XRD patterns of the obtained coatings

Рис. 5. Рентгеновские дифрактограммы полученных покрытий the micro-melt pool on the substrate, ultimately forming the coating.

Microhardness measurements of WC/Ni–Al–Fe coatings revealed a monotonic increase in average values from 7.2 to 10.6 GPa as the tungsten carbide powder content in the NLE increased (Fig. 6). The microhardness of ANW2 and ANW4 samples remained similar (~7.5 GPa), which can be attributed to their structural similarity (see Figs. 3, *a–d*). Literature data indicate that the microhardness of plasma-clad $(NiAl)_{0.8}WC_{0.2}$–Fe(0–15 wt. %) coatings is significantly lower (4–6 GPa) due to their lower tungsten carbide content [17].

The results of tribological tests of WC/Ni–Al–Fe coatings are presented in Fig. 6. Depending on the WC concentration in the coatings, the friction coefficient varies non-monotonically from 0.61 to 0.73 under a 25 N load and from 0.62 to 0.70 under a 50 N load (Fig. 7, *a*). In both cases, the highest friction force values were observed for the ANW4 sample. The friction coefficient of the coatings was 8–31 % lower than that of 35 steel, demonstrating the anti-friction effect of tungsten carbide. Additionally, the amplitude of friction coefficient fluctuations for all coatings was significantly lower compared to 35 steel.

The specific wear rate of WC/Ni–Al–Fe coatings ranged from $(36–55)\cdot10^{-7}$ mm^3/(N·m) under a 25 N load and $(28–31)\cdot10^{-7}$ mm^3/(N·m) under a 50 N load, which is 11–24 times lower than that of 35 steel (Fig. 7, *b*). Unlike uncoated steel, the specific wear rate of the coatings at 50 N was lower than at 25 N. As the WC powder content in the NLE increased, the specific wear rate of the WC/Ni–Al–Fe coatings monotonically decreased under both loads. This trend aligns with Archard's wear theory, as it is attributed to the increase in coating hardness. Although the minimum specific wear rate was

***Table 3.* Semi-quantitative composition of the coatings**

***Таблица 3.* Полуколичественный состав покрытий**

Sample	Phase, vol. %			
	WC	W_2C	AlNi	FeNi
ANW2	48.6	14.1	28.2	9.0
ANW4	61.5	14.9	18.7	4.9
ANW6	65.5	24.1	10.3	–

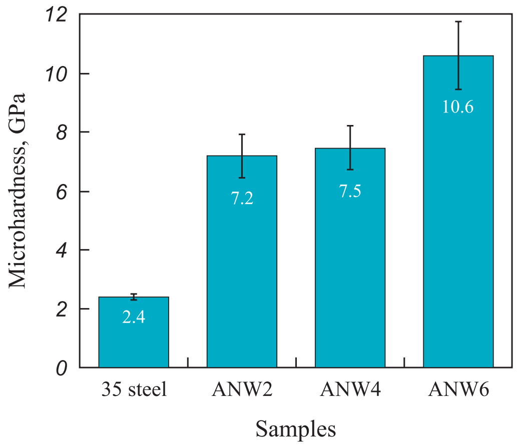

Fig. 6. Average microhardness values of the coatings

Рис. 6. Средние значения микротвердости покрытий

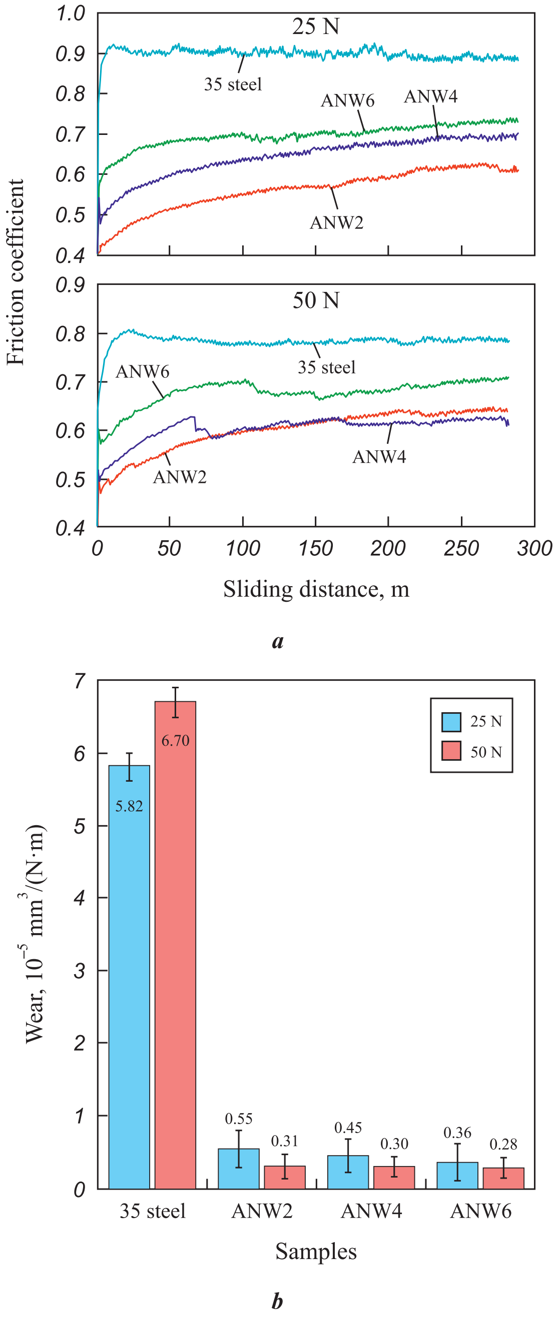

a

b

Fig. 7. Coefficient of friction (***a***) and wear rate (***b***) of coatings compared to steel 35 at loads of 25 and 50 N

Рис. 7. Коэффициент трения (***a***) и интенсивность изнашивания (***b***) исследуемых покрытий по сравнению со сталью 35 при нагрузках 25 и 50 Н not observed within the tested compositions, further increasing the WC powder concentration in the NLE is impractical due to the reduction in cathode mass gain, iron enrichment of the coating matrix, and depletion of nickel and aluminum concentrations. The wear rate of plasma-clad $(NiAl)_{0.8}WC_{0.2}$–Fe(0–15 wt. %) coatings, as reported in [17], was significantly higher at $6.02 \cdot 10^{-5}$ mm^3/(N·m). This is likely due to their lower tungsten carbide concentration and lower hardness. Therefore, the proposed approach for producing Ni–Al–Fe coatings reinforced with tungsten carbide on steels appears to be more effective.

Electrochemical corrosion tests of WC/Ni–Al–Fe coatings were conducted in a 3.5 % NaCl solution using potentiodynamic polarization and impedance spectroscopy methods. Fig. 8, *a* presents Tafel polarization curves constructed from potentiodynamic experiments. The corrosion potential (E_{corr}) and corrosion current density (I_{corr}) were determined by extrapolating the cathodic and anodic slopes of the Tafel plots. As shown in Table 4, the corrosion potential of the coated samples ranged from –0.68 V to –0.57 V relative to the Ag/AgCl electrode. The highest E_{corr} value was observed in the ANW4 sample, indicating its greater resistance to spontaneous corrosion compared to the other coatings. The corrosion current density of the coated samples ranged from $3.9 \cdot 10^{-5}$ to $2.5 \cdot 10^{-4}$ A/cm^2, with the lowest value recorded for ANW4 and the highest for ANW2. For uncoated 35 steel, the corrosion current density was $5.5 \cdot 10^{-5}$ A/cm^2. Given that corrosion rate is directly proportional to I_{corr}, it can be concluded that only the ANW4 coating improves the corrosion resistance of 35 steel by 29 %.

Fig. 8, *b* presents Bode impedance diagrams, which describe the frequency-dependent electrochemical behavior at the material-electrolyte interface. It is known that an increase in the impedance modulus (lg|*Z*|) at low frequencies hinders charge transfer, thereby improving the corrosion resistance of the material [32]. The WC/Ni–Al–Fe coatings can be ranked in ascending order of lg|*Z*| values as follows: ANW4, ANW2, and ANW6. Thus, the sample with the highest tungsten carbide concentration exhibits the greatest charge transfer resistance. According to the Bode plots, the impedance maximum of the steel substrate was higher than that of the coatings, indicating their weaker corrosion resistance. Notably, Ni–Al–Fe coatings without WC demonstrated higher charge transfer resistance [33]. This is likely due to the fact that conductive tungsten carbide disrupts the continuity of the Al_2O_3 barrier layer, which forms on the surface of WC/Ni–Al–Fe coatings in the electrolyte solution.

Table 4. **Corrosion potential and current density of WC/Ni–Al–Fe coatings in a 3.5 % NaCl solution**

Таблица 4. **Потенциал и плотность тока коррозии WC/Ni–Al–Fe-покрытий в 3,5 %-ном растворе NaCl**

Parameter	35 steel	ANW2	ANW4	ANW6
E_{corr}, V	–0.72	–0.63	–0.57	–0.68
I_{corr}, µA	54.48	250.84	39.36	142.10

Overall, the corrosion resistance of WC/Ni–Al–Fe coatings can be considered weak, likely due to their relatively high iron concentration (35.5 to 57.6 at. %). Additionally, as a ceramic material with high electrical conductivity, tungsten carbide does not provide barrier protection against corrosion. Instead, it may form galvanic couples at the interface between the metallic matrix and WC particles.

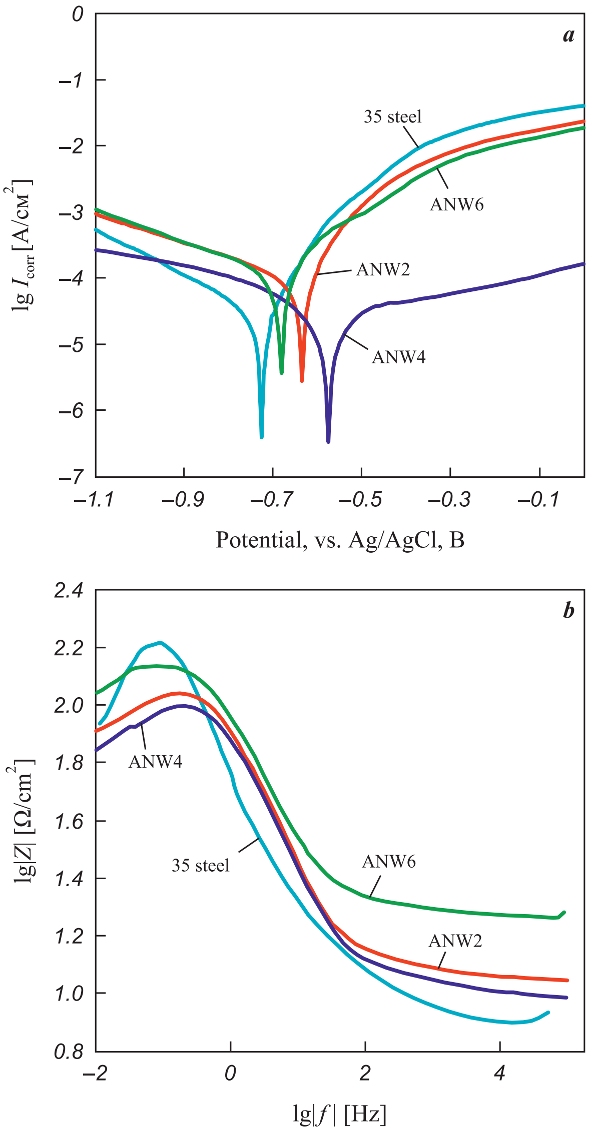

Fig. 8. Polarization curves (***a***) and Bode impedance plots (***b***) of WC/Ni–Al–Fe coatings and 35 steel

Рис. 8. Поляризационные кривые (***а***) и импедансные графики Боде (***b***) WC/Ni–Al–Fe-покрытий и стали 35

Fig. 9, *a* presents the results of cyclic oxidation resistance tests of 35 steel samples with WC/Ni–Al–Fe coatings at 700 °C. After 110 h of testing, the mass gain of the coated samples ranged from 8.3 to 39.8 g/m^2, while the steel substrate exhibited a significantly higher mass gain of 416.2 g/m^2. Thus, the application of WC/Ni–Al–Fe coatings enhances the oxidation resistance of 35 steel by a factor of 10.5 to 49.9. It should be noted that the mass gain of Ni–Al–Fe coatings produced without tungsten carbide under similar test conditions was comparable to the current results [33]. The oxidation resistance of the coated samples increased in the following order: ANW2, ANW6, and ANW4.

These findings indicate that incorporating up to 65 vol. % WC into the Ni–Al–Fe layer does not degrade its oxidation resistance. The ANW4 coating demonstrated the best performance, which aligns with the potentiodynamic polarization data (see Table 4). The mass gain during the oxidation resistance test resulted from the fixation of oxygen on the sample surfaces in the form of hematite (Fe_2O_3) and iron tungstate (Fe_2WO_6) (see Fig. 9, *b*), which forms through the simultaneous oxidation of iron and tungsten carbide:

$$WC + 2Fe + 4O_2 = Fe_2WO_6 + CO_2.$$

In addition to these compounds, Fe_3W_3C and AlNi phases were also detected, further confirming the high oxidation resistance of the coatings. The Fe_3W_3C phase forms due to the recrystallization of W_2C during prolonged high-temperature exposure. Overall, all WC/Ni–Al–Fe coatings exhibited high oxidation resistance at 700 °C, comparable to that of metallic glasses [34], while also demonstrating greater wear resistance during wear testing.

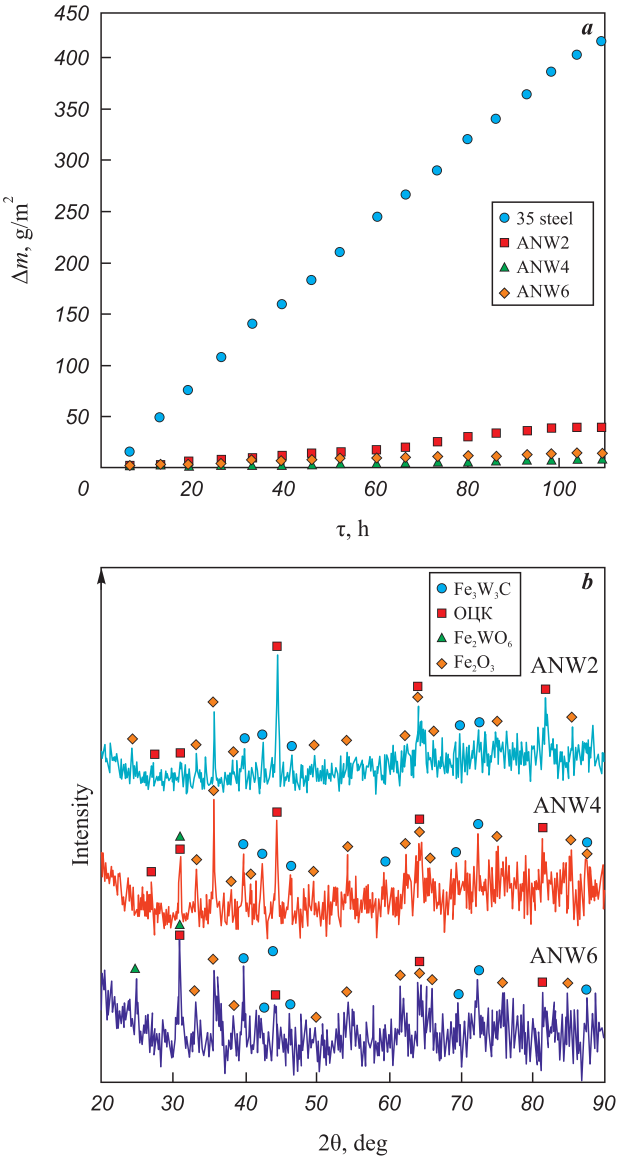

Fig. 9. Cyclic oxidation resistance of coated samples at 700 °C (***a***) and XRD patterns of coatings after oxidation resistance testing (***b***)

Рис. 9. Результаты циклических испытаний образцов на жаростойкость при температуре 700 °C (***a***) и рентгеновские дифрактограммы покрытий после этих испытаний (***b***)

Conclusion

For the first time, metalloceramic WC/Ni–Al–Fe coatings were successfully deposited on 35 steel using the ESD method with a nonlocalized electrode, composed of nickel and aluminum granules (15 at. % Al and 85 at. % Ni) with 2, 4, and 6 vol. % WC powder. The coating matrix consisted of nickel aluminide (NiAl) and ferro-nickel, while α-WC and W_2C inclusions acted as reinforcing phases. Increasing the WC powder content in the nonlocalized electrode led to a higher tungsten carbide concentration in the coatings.

Impedance and polarization experiments in a 3.5 % NaCl solution revealed that WC/Ni–Al–Fe coatings exhibit weak corrosion resistance, while their cyclic oxidation resistance at 700 °C was 10.5 to 49.9 times higher than that of 35 steel.

Microhardness testing showed a monotonic increase from 7.2 to 10.6 GPa as the WC powder concentration in the nonlocalized electrode increased from 2 to 6 vol. %. The application of WC/Ni–Al–Fe coatings reduced the friction coefficient of 35 steel components by 8–31 % and lowered the specific wear rate by a factor of 11 to 24.

References / Список литературы

1. Mari D., Bolognini S., Feusier G., Cutard T., Verdon C., Viatte T., Benoit W. TiMoCN based cermets: Part I. Morphology and phase composition. *International Journal of Refractory Metals and Hard Materials*. 2003;21(1–2):37–46. https://doi.org/10.1016/S0263-4368(03)00010-6

2. Wang L., Bai J., Wang Y., Men Z. A review of research progress on Ti (C, N)-based cermet binder by intermetallic compounds and high-entropy alloys. *Materials*. 2024;17(3):675. https://doi.org/10.3390/ma17030675

3. Erfanmanesh M., Abdollah-Pour H., Mohammadian-Semnani H., Shoja-Razavi R. Kinetics and oxidation behavior of laser clad WC–Co and Ni/WC–Co coatings. *Ceramics International*. 2018;44(11):12805–12814. https://doi.org/10.1016/j.ceramint.2018.04.087

4. Yang L.J., Wang S.P., Wang P., Li H., Yang H.Y., Ye Y.S., Li Z.X. Microstructural evolution and abrasive resistance of WC7Co ceramic particle-reinforced Ti6Al4V composite coating prepared by pulse laser cladding. *Journal of Iron and Steel Research International*. 2020;27(2):228–237. https://doi.org/10.1007/s42243-019-00359-y

5. Cheng J., Peng J., Wang M., Bo K., Li K., Zhang G., Yang Z. Effects of cyclic heating and water-cooling on the mechanical properties of WC–Co coatings. *Journal of Alloys and Compounds*. 2020;831:154769. https://doi.org/10.1016/j.jallcom.2020.154769

6. Dvornik M.I., Vlasova N.M. Comparative analysis of the tool life of submicron hard alloy WC-10Co sintered from powder obtained by electro discharge in oil. *Powder Metallurgy and Functional Coatings*. 2023;17(1):75–84. https://doi.org/10.17073/1997-308X-2023-1-75-84

Дворник М.И., Власова Н.М. Сравнительный анализ эксплуатационной стойкости субмикронного твердого сплава WC–10Co, спеченного из порошка, полученного электроэрозионным диспергированием в масле. *Известия вузов. Порошковая металлургия и функциональные покрытия*. 2023;17(1):75–84. https://doi.org/10.17073/1997-308X-2023-1-75-84

7. Ojo-Kupoluyi O., Tahir S., Baharudin B., Azmah Hanim M., Anuar M. Mechanical properties of WC-based hardmetals bonded with iron alloys – A review. *Materials Science and Technology*. 2017;33:507–517. https://doi.org/10.1080/02670836.2016.1186929

8. Sun J., Zhao J., Gong F., Ni X., Li Z. Development and application of WC-based alloys bonded with alternative binder phase. *Critical Reviews in Solid State and Materials Sciences*. 2019;44(3):211–238. https://doi.org/10.1080/10408436.2018.1483320

9. Piechowiak D., Kania A., Łukaszkiewicz N., Miklaszewski A. Properties and microstructure evaluation in NiAl-xWC (x = 0–90 wt. %) intermetallic-based composites prepared by mechanical alloying. *Materials*. 2023; 16(5):2048. https://doi.org/10.3390/ma16052048

10. Li X., Zhang M., Zheng D., Cao T., Chen J., Qu S. The oxidation behavior of the WC–10 wt.% Ni$_3$Al composite fabricated by spark plasma sintering. *Journal of Alloys and Compounds*. 2015;629:148–154. https://doi.org/10.1016/j.jallcom.2015.01.010

11. Yao H.R., Bao Z.B., Shen M.L., Zhu, S.L., Wang F.H. A magnetron sputtered microcrystalline β-NiAl coating for SC superalloys. Part II. Effects of a NiCrO diffusion barrier on oxidation behavior at 1100 °C. *Applied Surface Science*. 2017;407:485–494. https://doi.org/10.1016/j.apsusc.2017.02.245

12. Deevi S.C. Advanced intermetallic iron aluminide coatings for high temperature applications. *Progress in Materials Science*. 2021;118:100769. https://doi.org/10.1016/j.pmatsci.2020.100769

13. Jia Q., Li D., Li S., Zhang Z., Zhang N. High-temperature oxidation resistance of NiAl intermetallic formed in situ by thermal spraying. *Coatings*. 2018;8(8):292. https://doi.org/10.3390/coatings8080292

14. Zou Y., Kusabiraki K., Saji S. Effect of Ni addition on formation of amorphous and nanocrystalline phase during mechanical alloying of Al–25 at.%Fe–(5,10) at.%Ni powders. *Materials research bulletin*. 2002;37(7):1307–1313. https://doi.org/10.1016/S0025-5408(02)00762-6

15. Schneibel J.H., George E.P., Specht E.D., Horton J.A. Strength, ductility, and fracture mode of ternary FeAl alloys. *MRS Online Proceedings Library*. 1994;364:73–78. https://doi.org/10.1557/PROC-364-73

16. Celik E., Culha O., Uyulgan B., Ak Azem N.F., Ozdemir I., Turk A. Assessment of microstructural and mechanical properties of HVOF sprayed WC-based cermet coatings for a roller cylinder. *Surface and Coatings Technology*. 2006;200(14–15):4320–4328. https://doi.org/10.1016/j.surfcoat.2005.02.158

17. Yuan J., Wang Q., Liu X., Lou S., Li Q., Wang Z. Microstructures and high-temperature wear behavior of NiAl/WC-Fe$_x$ coatings on carbon steel by plasma cladding. *Journal of Alloys and Compounds*. 2020;842:155850. https://doi.org/10.1016/j.jallcom.2020.155850

18. Xu B., Zhu Z., Ma S., Zhang W., Liu W. Sliding wear behavior of Fe–Al and Fe–Al/WC coatings prepared by high velocity arc spraying. *Wear*. 2004;257(11):1089–1095. https://doi.org/10.1016/j.wear.2004.05.012

19. Mostajeran A., Shoja-Razavi R., Hadi M., Erfanmanesh M., Barekat M., Firouzabadi M.S. Evaluation of the mechanical properties of WC–FeAl composite coating fabricated by laser cladding method. *International Journal of Refractory Metals and Hard Materials*. 2020;88:105199. https://doi.org/10.1016/j.ijrmhm.2020.105199

20. Zhou J., Huang Y., Liang G., Zhao J., Hao X. Effect of copper on microstructure and performance of WC/NiAl/TiC composite coatings by laser cladding. *Advanced Engineering Materials*. 2024;26(10):2302059. https://doi.org/10.1002/adem.202302059

21. Jamnapara N.I., Frangini S., Alphonsa J., Chauhan N.L., Mukherjee S. Comparative analysis of insulating properties of plasma and thermally grown alumina films on electrospark aluminide coated 9Cr steels. *Surface and Coatings Technology*. 2015;266:146–150. https://doi.org/10.1016/j.surfcoat.2015.02.028

22. Burkov A.A., Kulik M.A. Electrospark deposition and structure of ceramic-metal WC/Fe–Al coatings. *Svarochnoye proizvodstvo*. 2023;2:26–32. (In Russ.). https://doi.org/10.34641/SP.2023.1059.2.013

Бурков А.А., Кулик М.А. Электроискровое осаждение и структура металлокерамических WC/Fe–Al покрытий. *Сварочное производство*. 2023;2:26–32. https://doi.org/10.34641/SP.2023.1059.2.013

23. Burkov A.A. Wear resistance of electrospark WC–Co coatings with different iron contents. *Journal of Friction and Wear*. 2016;37(4):385–388. https://doi.org/10.3103/s1068366616040048

24. Verkhoturov A.D. Formation of the surface layer of metals during electrospark deposition. Vladivostok: Dal'nauka, 1995. 323 p. (In Russ.).

Верхотуров А.Д. Формирование поверхностного слоя металлов при электроискровом легировании. Владивосток: Дальнаука, 1995. 323 с.

25. Kwok D.Y., Neumann A.W. Contact angle measurement and contact angle interpretation. *Advances in Colloid and Interface Science*. 1999;81(3):167–249. https://doi.org/10.1016/S0001-8686(98)00087-6

26. Burkov A.A., Krutikova V.O., Bytsura A.Yu., Khe V.K. Ti–Cr–Cu electrospark coatings on steel St3. *Problemy chernoi metallurgii i materialovedeniya*. 2023;(1):93–104. (In Russ.). https://doi.org/10.54826/19979258_2023_1_93

Бурков А.А., Крутикова В.О., Быцура А.Ю., Хе В.К. Ti–Cr–Cu электроискровые покрытия на стали Ст3. *Проблемы черной металлургии и материаловедения*. 2023;(1):93–104. https://doi.org/10.54826/19979258_2023_1_93

27. Burkov A.A., Chigrin P.G., Kulik M.A. The influence of the working conditions of the electrospark granules deposition on the formation of cracks in Ti–Al intermetallic coatings. *Solid State Phenomena*. 2021;316:814–820. https://doi.org/10.4028/www.scientific.net/SSP.316.814

28. Burkov A.A., Pyachin S.A. Investigation of WC–Co electrospark coatings with various carbon contents. *Journal of Materials Engineering and Performance*. 2014;23(6):2034–2042. https://doi.org/10.1007/s11665-014-0974-z

29. Nurminen J., Näkki J., Vuoristo P. Microstructure and properties of hard and wear resistant MMC coatings deposited by laser cladding. *International Journal of Refractory Metals and Hard Materials*. 2009;27(2):472–478. https://doi.org/10.1016/J.IJRMHM.2008.10.008

30. Jin H., Ji R., Dong T., Liu S., Zhang F., Zhao L., Liu Y. Efficient fabrication and characterization of Ni–Fe–WC composite coatings with high corrosion resistance. *Journal of Materials Research and Technology*. 2022;16:152–167. https://doi.org/10.1016/j.jmrt.2021.11.145

31. Kayali Y., Talaş Ş. Investigation of wear and corrosion behaviour of AISI 316 L stainless steel coated by ESD surface modification. *Protection of Metals and Physical Chemistry of Surfaces*. 2019;55(6):1148–1153. https://doi.org/10.1134/S2070205119060170

32. Rosalbino F., Scavino G. Corrosion behaviour assessment of cast and HIPed Stellite 6 alloy in a chloride-containing environment. *Electrochimica Acta*. 2013;111:656–662. https://doi.org/10.1016/j.electacta.2013.08.019

33. Burkov A.A., Kulik M.A., Bytsura A.Yu. Structure and properties of Al–Ni–Fe coatings on Steel 35 obtained by electrospark deposition. *Metal Science and Heat Treatment*. 2024;66(7):415–422. https://doi.org/10.1007/s11041-024-01065-7

Бурков А.А., Кулик М.А., Быцура А.Ю. Структура и свойства Al–Ni–Fe-покрытий на стали 35, полученных методом электроискрового легирования. *Металловедение и термическая обработка металлов*. 2024;7:22–30. https://doi.org/10.30906/mitom.2024.7.22-30

34. Lee C.Y., Sheu H.H., Tsay L.W., Hsiao P.S., Lin T.J., Lee H.B. The effect of heat treatment on the corrosion resistance of Fe-based amorphous alloy coating prepared by high velocity oxygen fuel method. *Materials*. 2021;14(24):7818. https://doi.org/10.3390/ma14247818

Information about the Author

Aleksandr A. Burkov – Cand. Sci. (Phys.-Math.), Senior Researcher, Head of the Laboratory of Physical and Chemical Fundamentals of Materials Technology, Institute of Materials Science of the Khabarovsk Federal Research Center of the Far Eastern Branch of the Russian Academy of Sciences
ORCID: 0000-0002-5636-4669
E-mail: burkovalex@mail.ru

Сведения об авторе

Александр Анатольевич Бурков – к.ф.-м.н., ст. науч. сотрудник, зав. лабораторией физико-химических основ технологии материалов, Институт материаловедения Хабаровского федерального исследовательского центра Дальневосточного отделения РАН
ORCID: 0000-0002-5636-4669
E-mail: burkovalex@mail.ru

Received 19.08.2024
Revised 21.01.2025
Accepted 24.01.2025

Статья поступила 19.08.2024 г.
Доработана 21.01.2025 г.
Принята к публикации 24.01.2025 г.

Зарегистрирован Федеральной службой по надзору
в сфере связи, информационных технологий
и массовых коммуникаций.
Свидетельство о регистрации ПИ № ФС77-79230

Журнал распространяется агентством «Урал-Пресс»
Подписной индекс: 80752 (печатная версия)
05108 (электронная версия)